Photon statistics of a single ion coupled to a high-finesse cavity

Dissertation

zur erlangung des Doktorgrades an der
Fakultät für Mathematik, Informatik und Physik
der Leopold-Franzens-Universität Innsbruck

vorgelegt von

Carlos Manuel da Silva Baptista Russo

durchgeführt am Institut für Experimentalphysik
unter der Leitung von
Univ. Prof. Dr. Rainer Blatt

Innsbruck
October 2, 2008

Abstract

The recent development of ideas and experiments in the field of quantum information have emphasised the importance of achieving coherent control over quantum systems. In particular, entanglement of a single atom with a single photon is believed to be a resource of key importance for establishing networks for the distribution of quantum information. Such goals can be achieved by controlling the emission of light by a single atom or ion.

This thesis reports on the design, construction and operation of a single-ion device: a novel versatile experimental setup that allows control of light emission by a single ion.

A single $^{40}Ca^{+}$ ion is stored in a linear Paul trap and coupled to a high-finesse resonator. The ion is externally excited by two laser fields at wavelengths of 397 nm and 866 nm. The laser at 397 nm and the optical cavity are detuned by the same amount from the $S_{1/2} \leftrightarrow P_{1/2}$ and $D_{3/2} \leftrightarrow P_{1/2}$ transitions respectively. Consequently, a vacuum-stimulated Raman transition is driven and the population in the state $S_{1/2}$ is transferred to the $D_{3/2}$ manifold, while a photon is emitted into the cavity. The atomic population in the metastable $D_{3/2}$ state is then optically pumped back to the ground state $S_{1/2}$ by using the second laser, at a wavelength of 866 nm, near-resonant to the $D_{3/2} \leftrightarrow P_{1/2}$ transition. The emitted photons are stored for about 1 μs before leaving the resonator.

The various building blocks of the single-ion device are first characterized and used to demonstrate that the spectral properties of the emitted light can be controlled by manipulating the laser detunings and the magnetic field.

This is followed by a discussion on the measurements of the statistical behaviour of the photon stream produced by the single-ion device when it is operated under pulsed and continuous external laser excitation. Under pulsed excitation, the single-ion device behaves as an efficient single-photon source. Under continuous operation, it is shown that the statistical properties of the photons can be controlled by the laser intensities. Depending on the laser parameters, it is experimentally demonstrated that the single-ion device can be tuned from a regime dominated by sub-Poissonian photon statistics and associated with single-photon emissions to a regime resembling a thermal source following super-Poissonian photon statistics. A careful analysis supported by numerical simulations shows that the device can even display a behaviour characteristic of a conventional laser operating at threshold.

Zusammenfassung

Die jüngste Entwicklung der Ideen und Experimente im Feld der Quanteninformation betonen die herausragende Bedeutung der kohärenten Kontrolle über Quantensysteme. Dabei bildet die Verschränkung eines einzelnen Atoms mit einem einzelnen Photon eine fundamentale Ressource zur Etablierung von Netzwerken für die Verteilung von Quanteninformation. Diese Ziele können durch Kontrolle der Lichtmission eines einzelnen Atomes oder Ions erreicht werden.

In dieser Dissertation wird das Design, die Konstruktion und den Betrieb eines Einzelionensystemes beschrieben: Ein neuartiger, vielseitiger experimenteller Aufbau, der die kontrollierte Emission von Licht durch ein einzelnes Atom erlaubt.

Ein einzelnes $^{40}Ca^{+}$ wird in einer linearen Paulfalle gefangen und an einen optischen Resonator hoher Finesse gekoppelt. Das Ion wird von zwei externen Laserfeldern der Wellenlängen 397 nm und 866 nm angeregt. Der Laser bei 397 nm und der optische Resonator sind um den gleichen Betrag vom $S_{1/2} \leftrightarrow P_{1/2}$ und $D_{3/2} \leftrightarrow P_{1/2}$ verstimmt. Dadurch wird ein vakuum-stimulierter Ramanübergang getrieben, bei dem die atomare Besetzung aus dem $S_{1/2}$ Zustand in den $D_{3/2}$ Zustand übertragen und ein Photon in den Resonator emittiert wird. Die atomare Besetzung des metastabilen $D_{3/2}$ Zustandes wird anschließend mit dem zweiten Laser bei 866 nm, der quasiresonant mit dem $D_{3/2} \leftrightarrow P_{1/2}$ Übergang ist, optisch zum Grundzustand $S_{1/2}$ zurückgepumpt. Die in den Resonator emittierten Photonen werden für ungefähr 1 μs gespeichert, bevor sie ihn verlassen.

Anfangs werden die verschiedenen Teile des Einzelionensystems charakterisiert. Es wird gezeigt, dass die spektralen Eigenschaften des emittierten Lichtes durch Manipulation der Laserverstimmungen und des magnetischen Feldes kontrolliert werden können.

Anschließend werden Messungen des statistischen Verhaltens des Photonenstromes diskutiert, der vom Einzelionensystem bei gepulster und kontinuierlicher Laseranregung produziert wird. Während sich das Einzelionensystem bei gepulster Anregung als eine effiziente Einzelphotonenquelle verhält, können die statistischen Eigenschaften der Photonen bei kontinuierlichem Betrieb durch die Laserintensitäten kontrolliert werden. Der Übergang von einem Regime sub-Poissonscher Photonenstatistik, welches mit Einzelphotonenemissionen assoziiert wird, zu einem Regime super-Poissonscher Photonenstatistik, welches einer thermischen Lichtquelle gleicht, wird im Experiment durch Einstellen der Laserparameter herbeigeführt. In einer von numerischen Simulationen unterstützten, detaillierten Analyse wird gezeigt, dass das System sogar das charakteristische Verhalten eines konventionellen Lasers an der Laserschwellwe aufweist.

Para ser grande, sê inteiro: nada
Teu exagera ou exclui.
Sê todo em cada coisa. Põe quanto és
No mínimo que fazes.
Assim em cada lago a lua toda
Brilha, porque alta vive.

To be great, be whole; exclude
Nothing, exaggerate nothing that is you.
Be whole in every thing. Put all you are
Into the smallest thing you do.
The whole moon gleams in every pool,
It rides so high.

Ricardo Reis, Odes de Ricardo Reis *(14-2-1933)*

Contents

Chapter 1

Introduction

The work described in this thesis explores the measurement of the statistical properties of light emitted by a single ion coupled to an optical resonator.

Historically, the measurement of photon statistics was motivated by the study of the *spatial coherence* properties of light. Using an intensity interferometer comprised of two photoelectric detectors, Hanbury Brown and Twiss measured the angular diameter of stars [1, 2]. Their experiments made use of the fact that light from a thermal source (a star) follows super-Poissonian statistics. In particular, they explored the fact that photoelectric detection at the two detectors show a positive correlation (i.e. $g^{(2)} > 1$), which is commonly known as *photon bunching*. This positive correlation only exists for photons in the same spatial mode. By varying the distance between the two detectors, the angular diameter of a given star could be determined from the decrease in the photon bunching.

The measurement of *time-resolved* photodetection correlations was used to demonstrate the quantum nature of light: in 1977, Kimble et al. [3] demonstrated *photon antibunching* in resonance fluorescence of atomic sodium. The fluctuations in the number of atoms in the beam hindered the immediate demonstration of sub-Poissonian statistics. Following a similar technique, Short et al.[4] finally observed in 1983 resonance fluorescence with sub-Poissonian statistics, by improving the detection efficiency and attenuating the atomic beam to the point that only one atom was observed at a time. Sub-Poissonian photon statistics has also been observed in various sources, including masers [5, 6] and solid-state systems [7].

The invention of the laser [8] by Maiman et al. in 1960 followed the development of the maser [9, 10] and marked the birth of a new field in physics: quantum optics. Over time, the low noise and spectral density of the lasers became an essential tool in precision spectroscopy, which naturally led to techniques such as laser cooling. In turn, the cooling and trapping of single neutral atoms and ions became possible.

In 1976, van Dyck et al. reported on frequency measurements on a single trapped electron using a Penning trap [11] that allowed the determination of the g-factor of the electron. This work motivated experiments in precision spectroscopy using single trapped ions. The trapping of a single ion was first demonstrated in 1979 by Neuhauser et al. [12]: a single Barium ion was stored in a quadrupole Paul trap [13] and laser-cooled to a spatial localisation of ~ 2 μm. The ability to trap single particles contributed to the evolution of high-resolution spectroscopy, to the point that nowadays single trapped ions allow the implementation of frequency standards with fractional uncertainties of the order of 10^{-17} [14].

In the last two decades, the attention shifted towards the possibility of exerting control over quantum systems, which opened new research fronts. A prominent example is the field of quantum information processing, where information is encoded in the state of a quantum system and logical operations (also called gates) consist of a sequence of controlled interactions. In a restricted set of problems, the complexity of some notable quantum algorithms (such as Shor's factorisation algorithm) has been shown to scale much better that any classical solution [15, 16]. It is widely believed that the reason for such computational gain is the use of entanglement as a resource. Experimentally, a rudimentary quantum computer has already been implemented: laser pulses and trapped ions have been used to demonstrate gates and simple algorithms [17–20].

The scalability of quantum computers depends on their ability to exchange information. While atomic systems are well-suited to store quantum information for long periods of time, today's best known way to transport quantum information over distances exceeding millimetres is via optical photons [21, 22]. Therefore, in order to establish quantum networks, it is desirable to have a deterministic interface between atomic qubits stored in trapped atoms and photons [23]. Such requirement stresses the necessity of having full control over the emission and absorption of photons, which can be obtained by making use of stimulated processes, typically requiring strong coupling between the emitter and communication channel [24].

An atom strongly coupled to a cavity allows a nearly one-dimensional description [25] in the sense that photons are emitted/absorbed into/from one mode of the radiation field and is consequently a natural model. Technically, low-loss resonators and small cavity mode volumes are required to achieve strong coupling, in which coherent processes dominate over incoherent processes. Although strong coupling of neutral atoms to cavities has already been achieved, it is currently not possible to trap an atom for very long periods of time, at least in comparison with ions. However, obtaining strong coupling with ions is challenging, as it is difficult to engineer a small trap inside a short cavity. Moreover, setting an ion trap around a cavity might not work, as charge patches on the cavity surface may lead to excessive ion heating rates. As challenging as such implementations may be, single trapped ions have been successfully coupled to cavities [26–28].

While these technical problems are not yet solved for good, we approached the problem by pursuing a cavity in concentric configuration and using a Raman scheme [29–31]. The concentric scheme allows the possibility to fit a trap safely between the cavity mirrors, while obtaining small mode volume and narrow cavity linewidth, at the cost of some potential manufacturing difficulties. The use of a Raman transition in a Λ-type three-level system allows suppression of spontaneous emission and the ability to control the degree of ion-cavity coupling: by working at a detuning Δ, the rate of spontaneous scattering (via off-resonant excitation of the upper state followed by spontaneous emission) scales with $(\Omega/\Delta)^2$ while the ion-field coupling scales with Ω/Δ, where Ω is the Rabi frequency of the driving laser. In other words, the parameters of the driving field act as a handle that controls the dynamics of the system, from a regime dominated by the coherent ion-cavity coupling, to a dissipative regime dominated by incoherent processes.

Such a single-ion device has tremendous flexibility and offers a rich variety of new physics. By switching the ion-cavity coupling on and off, the system can be used to efficiently produce a stream of single photons [31]. Depending on the strength of the ion-cavity coupling, the photons can be emitted via spontaneous or stimulated processes. Such photons are strongly correlated with its emitter: a fact that can be

explored for the generation of entangled states. By exciting the ion continuously, a laser-like system with a single ion as gain medium can be implemented [32, 33]. In fact, a single atom coupled to a resonator and under external excitation constitutes the most elementary model for a laser. Conventional lasers are made of a large collection of atoms and photons and operate in a regime where the interactions between each atom and the cavity mode are weaker than the dissipative processes (atomic spontaneous emission and photon loss from the cavity mode). They operate thus in a *weak atom-cavity coupling regime*. In opposition, one-atom lasers typically operate in the *strong coupling regime*, in which the atom-cavity interaction is stronger than the dissipative process. It is therefore not surprising that one-atom lasers have fundamentally different properties when compared to conventional lasers. By varying the ion-cavity coupling, the single-ion device can be used to probe the smooth transition from a laser system that is manifestly quantum-mechanical to a more conventional classical laser.

This thesis describes the design, construction and exploration of such a single-ion device: a system that can be used to produce light in a controlled fashion into a well-defined mode. The experiments discussed in this manuscript are centred on the analysis of the spectral and statistical properties of such light.

The dissertation is organised as follows.

In chapter 2, the theory for an ideal two-level system in a cavity mode is presented. This description is first extended to include dissipation, and further expanded to a three-level atom. The concept of a vacuum-stimulated Raman transition is first introduced and an approximation is made that allows the simplification of the theoretical picture in terms of an effective two-level system, which allows for a more straightforward grasp of the physical concepts behind the single-ion device. The basic concepts on the measurement of photon statistics are introduced, namely second-order correlations of the photoelectric detection events.

In chapter 3, the relevant properties of the calcium ion are presented and integrated in a theoretical framework that is later used to numerically simulate the properties of the single-ion device.

The experimental setup is presented in chapter 4. The main components of the experiment are introduced: linear Paul trap, high-finesse cavity, vacuum system, laser setup and photon detection setup at wavelengths of 397 nm and 866 nm. The basic methodology for daily operation of the experiment is described in chapter 5: trapping and cooling of ions, calibration of the laser parameters, normalisation of photon correlations. The spectral properties of the light at the cavity output are also discussed.

The main experimental results on the photon statistics of the single-ion device are presented in chapters 6 – 8. The single-ion device is first used to implement a deterministic single-photon source, as discussed in chapter 6. In chapter 7, by continuously exciting the system, it is demonstrated that the statistical properties of the light at the cavity output can be tuned by controlling the external excitation. In particular, a smooth transition from non-classical to classical photon statistics is shown. The various regimes of photon emission are presented and discussed in chapter 8. In particular, special care is taken with the transition between a regime characterised by spontaneous single-photon emissions to a region where the single-ion device behaves as a single-ion laser at threshold. The discussion is complemented with numerical simulations that allow the global interpretation of the results.

Finally, in chapter 9, the results are summarised and the perspectives of this work are discussed.

Chapter 2

Theory

This chapter introduces the basic theoretical concepts behind the interaction between an atom and a resonator.

Most of the physical concepts behind the experiments discussed in this dissertation can be grasped using the simplest possible model: a two-level atom interacting with a single mode of the radiation field. The atom-cavity interaction is modelled by the Jaynes-Cummings Hamiltonian. In the absence of dissipative processes, the dynamics of the system can be interpreted in terms of an infinite succession of two-level systems. The formal inclusion of mechanisms for the atomic spontaneous emission and the photon loss from the cavity mode leads naturally to the concepts of strong and weak coupling limits, which are characterised by completely different dynamics.

The experiments exploit a Raman transition and are more appropriately described using the concept of a three-level atom. Consequently, the model is extended to include a third level and the external coherent excitation. The discussion follows by adiabatically eliminating one of the levels, thus allowing the interpretation of the system as an effective two-level atom coupled to a thermal bath and exchanging photons with a cavity.

Finally, the basic concepts behind the measurement of the photon statistics are introduced.

2.1 Two-level atom in a cavity

2.1.1 Introduction

The canonical formalism of quantum theory applied to electromagnetic fields in free space in the absence of sources reveals that light is composed by bosonic quanta: *photons*. Photons in one mode of the electromagnetic field are then formally equivalent to excitations in a quantum harmonic oscillator [34].

Given the context of atomic physics, the natural model system for the interaction between one atom and one photon is a single hydrogen atom inside a resonator. However complete such a description may be, its dynamics is still rather complex, and current real world applications operate under very specific conditions that allow further simplifications.

In the simplest case, the system is modelled in the dipole approximation by a fictitious two-level atom interacting with a single mode of the electromagnetic field,

if the following conditions are satisfied:

1. the normal modes of the resonator are well separated in frequency;
2. only one such mode is populated, the others being devoid of photons;
3. this populated mode only interacts with a pair of atomic levels ($|\downarrow\rangle$ and $|\uparrow\rangle$) and leads to no modification on other levels.

Such situation can be found in the microwave and optical domains of the spectrum of light.

2.1.2 Jaynes-Cummings Hamiltonian

The Hamiltonian for a two-level atom interacting with a single mode of the radiation field was first given by Jaynes and Cummings[35]:

$$\hat{H} = \hbar\omega_0\sigma_z + \hbar\omega\hat{a}^\dagger\hat{a} + \hbar\left(g\hat{\sigma}^\dagger - g^*\hat{\sigma}\right)\left(\hat{a} - \hat{a}^\dagger\right) \tag{2.1}$$

Here, $\hat{\sigma}_z = (\widehat{\sigma}_{\uparrow\uparrow} - \widehat{\sigma}_{\downarrow\downarrow})/2$, where the operators $\widehat{\sigma}_{\uparrow\uparrow} = |\uparrow\rangle\langle\uparrow|$ and $\widehat{\sigma}_{\downarrow\downarrow} = |\downarrow\rangle\langle\downarrow|$ are projectors for the atomic excited and ground states, respectively. The levels have an energy difference of $\hbar\omega_0$. The operators $\hat{\sigma}^\dagger = |\uparrow\rangle\langle\downarrow|$ and $\hat{\sigma} = |\downarrow\rangle\langle\uparrow|$ are the atomic raising and lowering Pauli operators, respectively. Also, $\hat{a}$ and $\hat{a}^\dagger$ are the annihilation and creation operators for the electromagnetic field whose photons have an energy of $\hbar\omega$. The atom-cavity coupling constant is given by g. Please note that the motion of the atom is not considered.

In the limit of vanishing interaction ($g \to 0$), atom and cavity decouple and the Heisenberg equations of motion give $\hat{a}(t) = \hat{a}(0)e^{-i\omega t}$ and $\hat{\sigma}(t) = \hat{\sigma}(0)e^{-i\omega_0 t}$. Near resonance ($\omega \sim \omega_0$) and when the photon number is small, the terms in $\hat{\sigma}^\dagger\hat{a}^\dagger$ and $\hat{\sigma}\hat{a}$ change relatively fast ($\sim e^{\pm 2i\omega t}$). These terms describe processes that violate energy conservation and can only be allowed in time scales compatible with the uncertainty principle: $\hat{\sigma}^\dagger\hat{a}^\dagger$ is a process in which a photon is emitted and the atom is excited, and $\hat{\sigma}\hat{a}$ corresponds to the mechanism in which the atom absorbs one photon while returning to the ground state. Comparatively to the slow terms $\sigma a^\dagger$ and $\sigma^\dagger a$, the effect of the fast terms on the dynamics averages out; dropping the fast terms constitutes the Jaynes-Cummings Hamiltonian in the *rotating wave approximation*:

$$\hat{H} = \hbar\omega_0\hat{\sigma}_z + \hbar\omega\hat{a}^\dagger\hat{a} + \hbar g\hat{\sigma}^\dagger\hat{a} + \hbar g^*\hat{a}^\dagger\hat{\sigma} \tag{2.2}$$

Coupled states

The Hamiltonian (2.2) can be rewritten as a sum of two contributions: the Hamiltonian $\hat{H}_0$ for the non-interacting atom and cavity mode, and the Hamiltonian $\hat{H}_I$ for the interaction between them:

$$\hat{H} = \hat{H}_0 + \hat{H}_I$$

$$\hat{H}_0 = \hbar\omega_0\hat{\sigma}_z + \hbar\omega\hat{a}^\dagger\hat{a} \tag{2.3}$$

$$\hat{H}_I = \hbar g\hat{\sigma}^\dagger\hat{a} + \hbar g^*\hat{a}^\dagger\hat{\sigma} \tag{2.4}$$

The eigenstates of $\hat{H}_0$ constitute the *coupled states* (see Figures 2.1 and 2.2a)), denoted by $|\downarrow, n\rangle$ and $|\uparrow, n\rangle$. They are constructed by taking the tensor product of the

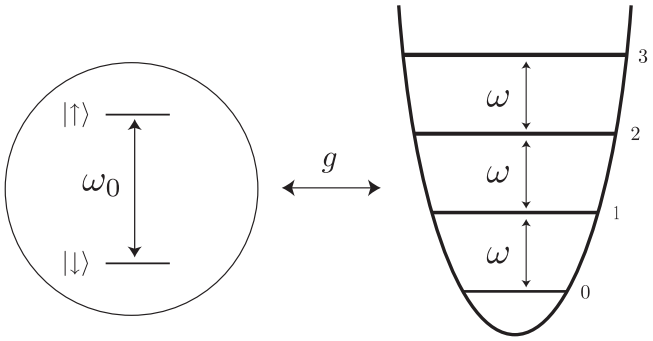

Figure 2.1: Composite atom-cavity system. The atom is a two-level system with energy difference $\hbar\omega_0$, whereas the cavity field is represented by an harmonic oscillator at a frequency ω. The Hilbert space of the composite system is the product of the atom and cavity spaces. The interaction of the two subspaces is ruled by the atom-cavity coupling g, at a detuning $\hbar\Delta = \hbar(\omega_0 - \omega)$.

atomic pseudospin states $|\downarrow\rangle$ and $|\uparrow\rangle$ with the cavity photon number states $|n\rangle$. The corresponding energies are simply given by the sum of the energies of two constituent systems, $E_{\downarrow,n} = \hbar(n\omega - \omega_0/2)$ and $E_{\uparrow,n} = \hbar(n\omega + \omega_0/2)$. On resonance $\omega = \omega_0$ and the states $|\uparrow, n-1\rangle$ and $|\downarrow, n\rangle$ are degenerate.

Dressed states

Introducing an interaction leads to a new set of eigenstates for the composite system, which could be colloquially seen as an *atom-photon molecule*. The *dressed states* are the eigenstates of the total Hamiltonian $\hat{H}$ in (2.2). The ground state of the system is $|\downarrow, 0\rangle$, with an associated energy $E_{\downarrow,0} = -\hbar\omega_0/2$. The remaining eigenstates $|\pm, n\rangle$ constitute an infinite series of independent multiplicities of two-level systems. Each pair of levels follows a dynamic evolution set by the (partial) Hamiltonians $H^{(n)}$.

In the basis $\{|\uparrow, n-1\rangle, |\downarrow, n\rangle\}$, the Hamiltonian for each multiplicity $n > 0$ reads

$$\hat{H}^{(n)} = \hbar \begin{pmatrix} (n-1)\omega + \omega_0/2 & g^* \sqrt{n} \\ g\sqrt{n} & n\omega - \omega_0/2 \end{pmatrix} \tag{2.5}$$

Obviously, for $n = 0$ we have $H^{(0)} = -\hbar\omega_0/2\,|\downarrow, 0\rangle\langle\downarrow, 0|$. Assuming g has a positive real value and that $g \ll \omega$, the eigenstates $|n, \pm\rangle$ and eigenvalues $\lambda_\pm^{(n)}$ of the partial Hamiltonians $H^{(n)}$ are:

$$|n, +\rangle = \cos\theta_n\,|n, \downarrow\rangle - \sin\theta_n\,|n-1, \uparrow\rangle \tag{2.6}$$

$$|n, -\rangle = \sin\theta_n\,|n, \downarrow\rangle + \cos\theta_n\,|n-1, \uparrow\rangle \tag{2.7}$$

$$\lambda_\pm^{(n)} = \hbar\omega\left(n - \frac{1}{2}\right) \pm \frac{\hbar}{2}\sqrt{\Delta^2 + 4g^2 n} \tag{2.8}$$

where we introduced the atom-cavity detuning $\Delta = \omega_0 - \omega$. The mixing angles θ_n

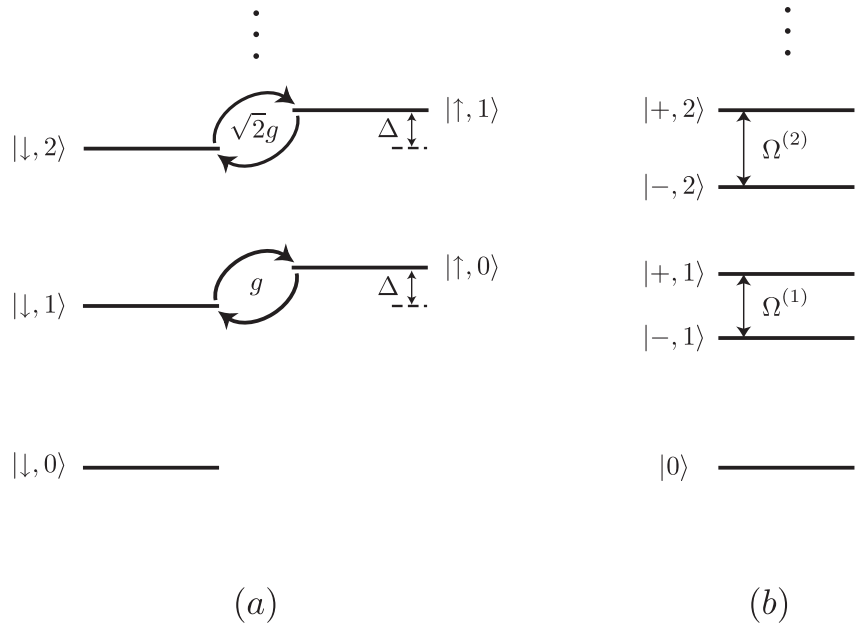

Figure 2.2: Ideal lossless two-level system in (a) the coupled-states picture and (b) the dressed-states picture. In the coupled-states picture (a), the energy level structure of the system can be regarded as two ladders of Fock states, each ladder being associated with one of the two atomic states. The cavity interaction connects one level of one ladder with one level of the other ladder. In the dressed-state picture (b), the energy level structure is a series of multiplicities composed of two levels $|\pm,n\rangle$ having an energy splitting of $\hbar\sqrt{\Delta^2+4g^2n}$. Excluding the ground state, the composite atom-cavity system can be seen as an infinite set of non-interacting two-level systems.

are defined such that

$$\sin\theta_n = +\frac{1}{\sqrt{2}}\left[1+\Delta/\sqrt{\Delta^2+4g^2n}\right]^{1/2} \tag{2.9}$$

$$\cos\theta_n = -\frac{1}{\sqrt{2}}\left[1-\Delta/\sqrt{\Delta^2+4g^2n}\right]^{1/2} \tag{2.10}$$

The multiplicity associated with a given n consists of the eigenstates $|n,\pm\rangle$ (see Figure 2.2b) which have an energy splitting of $2\hbar g\sqrt{n}$; in the absence of the atom-cavity interaction the states would be degenerate. The two levels within the n-th multiplicity are superpositions of the states $|\downarrow,n\rangle$ and $|\uparrow,n-1\rangle$. They interact coherently at an effective Rabi frequency $\Omega^{(n)} = \hbar\sqrt{\Delta^2+4g^2n}$. Each multiplicity is separated from the next by an energy of an intra-cavity photon, $\hbar\omega$. Obviously, the model holds only if the energy separation between successive multiplicities is much larger than the energy splitting of the states within each multiplicity, that is $\hbar\omega \gg 2\hbar g\sqrt{n}$.

2.1.3 Dissipation

The model developed up to now must include dissipative processes like spontaneous emission from the atom and photon loss from the cavity in order to approximate the

reality. In other words, it must be expressed as an open quantum system, which is usually done using a master equation formalism. The reader is directed to consult specialised literature [36, 37], here the procedure is only sketched.

The dissipative processes are represented in Figure 2.3. The system is assumed to be radiatively damped via its interaction with the many modes of the radiation field in thermal equilibrium at a temperature $T = 0$ K. The field is effectively a reservoir of empty modes.The interaction between the system and reservoir is assumed to be weak, in such a way that the state of the reservoir is virtually unaffected (Born approximation). Moreover, this interaction is taken to be memoryless (Markov approximation), which is equivalent to say that any correlations between the system and the reservoir disappear on a time scale much faster than the dynamics of the system, to the point at which they become irrelevant.

The system is now most conveniently described in terms of the reduced density operator $\hat{\rho}$. The master equation can be written as [37]:

$$\frac{d\hat{\rho}}{dt} = -\frac{i}{\hbar}\left(\hat{H}\hat{\rho} - \hat{\rho}\hat{H}^{\dagger}\right) + \mathscr{L}_{\text{diss}}(\hat{\rho}) = -\frac{i}{\hbar}\left[\hat{H}, \hat{\rho}\right] + \mathscr{L}_{\text{diss}}(\hat{\rho}) \tag{2.11}$$

where the relaxation superoperator $\mathscr{L}_{\text{diss}}(\hat{\rho})$ can be written in the Lindblad form in terms of collapse operators $\hat{C}_m$ containing the couplings between the system and the reservoir:

$$\mathscr{L}_{\text{diss}}(\hat{\rho}) = \frac{1}{2}\sum_m \left(2\hat{C}_m\hat{\rho}\hat{C}_m^{\dagger} - \hat{\rho}\hat{C}_m^{\dagger}\hat{C}_m - \hat{C}_m^{\dagger}\hat{C}_m\hat{\rho}\right) \tag{2.12}$$

Implementing dissipation in the model is thus reduced to expressing the relaxation mechanisms in terms of collapse operators.

Spontaneous emission is an irreversible process in which the atom emits one photon to the appropriate bath in the reservoir and is projected to the ground state. The corresponding collapse operator is $\hat{C}_{\text{spont}} = \sqrt{2\gamma}\sigma = \sqrt{2\gamma}\,|{\downarrow}\rangle\langle{\uparrow}|$, where 2γ is the spontaneous emission rate. Here it is implied that this operator acts only on the atom subspace. This procedure introduces a phenomenological linewidth to the upper level $|{\uparrow}\rangle$, which is equivalent to state that the upper level has a lifetime of $\tau = (2\gamma)^{-1}$. It also introduces a Lamb shift to the bare atom frequency ω_0, but this can and will be ignored in the following discussion.

The second relaxation mechanism to consider is the photon loss from the cavity, by coupling to the outside world. The corresponding collapse operator $\hat{C}_{cav} = \sqrt{2\varkappa}\hat{a}$ describes the dissipative process in which a photon is removed from the cavity mode at the rate $2\varkappa$. This implies that there is a finite photon storage time $\tau_c = (2\varkappa)^{-1}$.

The master equation (2.11) can be rewritten as

$$\frac{d\hat{\rho}}{dt} = -\frac{i}{\hbar}\left(\hat{H}_{\text{eff}}\hat{\rho} - \hat{\rho}\hat{H}_{\text{eff}}^{\dagger}\right) + \sum_m \hat{C}_m\hat{\rho}\hat{C}_m^{\dagger} \tag{2.13}$$

$$\hat{H}_{\text{eff}} = \hat{H} - \frac{i\hbar}{2}\left(\sum_m \hat{C}_m^{\dagger}\hat{C}_m\right) \tag{2.14}$$

Here we interpret $\hat{H}_{\text{eff}}$ as a non-hermitian operator that acts as an effective Hamiltonian. Even though $\hat{H}_{\text{eff}}$ does not preserve the norm of the state, the unitarity of the evolution is guaranteed by the *feeding* terms $\sum_m \hat{C}_m\rho\hat{C}_m^{\dagger}$.

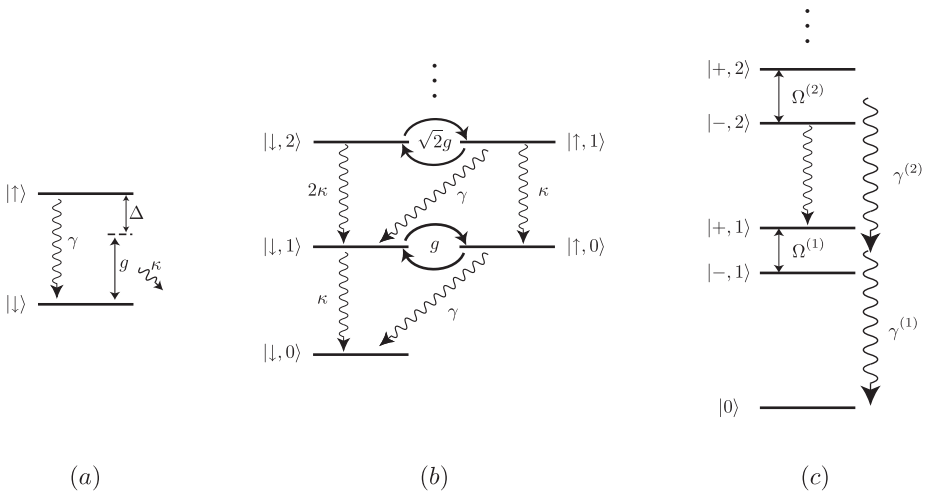

Figure 2.3: Level structure for the two-level atom in a cavity, with dissipation: (a) in the atomic bare-state picture, (b) in the coupled-states picture, and (c) in the dressed-states picture. In a): The atomic excited state can decay, with subsequent spontaneous emission of a photon, at a rate 2γ; the cavity can also leak one photon at a rate $2\varkappa$. In b): Compared to the lossless case of Fig. 2.2, the different multiplicities are now linked via dissipative processes. The population in higher-lying manifolds will eventually decay and populate lower-lying multiplicities until the ground state is reached. In c): Upon dissipation of one quanta, the population in higher-lying multiplicities is projected to one of the two eigenstates of the multiplicity immediately below. Eventually, the system will be projected in the ground state.

2.1.4 Coupling limits

Over time, the system interacts with the reservoir, until a stationary state is established. In general, this state can be determined from (2.11) by setting $d\hat{\rho}/dt = 0$ and solving for $\hat{\rho}$. However, because the reservoir is at $T = 0$ and the system is not being fed, the system can only lose energy to the reservoir. The stationary solution is trivially inferred: it must be the ground state. Nevertheless, this statement says nothing about the duration or evolution of any transient behaviour, which can be very short or infinitely long.

The effective Hamiltonian will now be used to determine the eigenvalues and the time evolution of the system. Similarly to (2.5), and also in the basis $\{|\uparrow, n-1\rangle, |\downarrow, n\rangle\}$, $\hat{H}_{\text{eff}}$ decomposes into a series of Hamiltonians for two-level systems ($n > 1$):

$$\begin{aligned}
\hat{H}^{(0)}_{\text{eff}} &= -\frac{\hbar\omega_0}{2}\,|\downarrow,0\rangle\langle\downarrow,0| \\
\hat{H}^{(n)}_{\text{eff}} &= \hbar\begin{pmatrix} (n-1)\omega + \frac{\omega_0}{2} - i\gamma - i\varkappa(n-1) & g^*\sqrt{n} \\ g\sqrt{n} & n\omega - \frac{\omega_0}{2} - i\varkappa n \end{pmatrix}
\end{aligned} \tag{2.15}$$

Solving the system (2.15) yields a new set of eigenvalues which are trivially found:

$$\lambda^{(n)}_{\pm} = \hbar\omega\left(n - \frac{1}{2}\right) \pm \frac{\hbar}{2}\sqrt{\left[\Delta - i(\gamma - \varkappa)\right]^2 + 4g^2 n} - i\hbar\varkappa\left(n - \frac{1}{2}\right) - \frac{i\hbar\gamma}{2} \tag{2.16}$$

Here we have used the *decay imbalance* $\delta = \gamma - \varkappa$, which expresses the imbalance between the two decay channels (leakage of a photon from the cavity or spontaneous emission into free space).

The eigenvalues $\lambda_{\pm}^{(n)}$ are potentially complex and can be cast into the more meaningful form $\lambda_{\pm}^{(n)} = E_{\pm}^{(n)} - i\hbar\gamma_{\pm}^{(n)}$, where $E_{\pm}^{(n)}$ and $\gamma_{\pm}^{(n)}$ are real valued and denote the energy and generalised linewidth of the associated eigenstate. Depending on the rates g, $\varkappa$ and γ, several limits can be found. Only the solutions $\lambda_{\pm}^{(n)}$ with a negative imaginary part have a physical meaning. To grasp the physics, it is sufficient to consider only the resonant cases, that is at $\Delta = 0$.

Strong coupling regime

In the limit $g \gg |\delta|, \gamma, \varkappa$, the solutions resemble the lossless oscillatory case described by equations (2.6)-(2.8). For $\Delta = 0$, each multiplicity is composed of two eigenstates $|\pm, n\rangle$, with energies $E_{\pm}^{(n)}$ differing by $\hbar\Omega^{(n)}$ and with linewidths given by $\gamma^{(n)}$:

$$E_{\pm}^{(n)} = \hbar\omega\left(n - \frac{1}{2}\right) \pm \frac{\hbar\Omega^{(n)}}{2} \tag{2.17}$$

$$\Omega^{(n)} = \sqrt{4g^2 n - \delta^2} \approx 2g\sqrt{n} - \frac{\delta^2}{4g\sqrt{n}} \tag{2.18}$$

$$\gamma^{(n)} = \varkappa\left(n - \frac{1}{2}\right) + \frac{\gamma}{2} \tag{2.19}$$

In the lossless case, each multiplicity was independent of the others, in the sense that it would follow its own dynamical evolution and would conserve population.

The dynamics of the system is still marked by the coherent exchange of quanta between the pairs of levels within each multiplicity at a rate $\Omega^{(n)}/2$. However, if one decay channel is faster than the other, the decay imbalance δ is non-zero and the coupling constant is effectively reduced from $2g\sqrt{n}$ to $\Omega^{(n)}$.

The population within each multiplicity is no longer conserved, as the dissipative processes link the successive multiplicities (see Figure 2.3c). Here, $\gamma^{(n)}$ characterises the rate at which population incoherently decays from the manifold n composed by the states $|\pm, n\rangle$, to the lower lying manifold $n-1$. Upon the loss of one quantum, the system is projected to one of the two (lower) $|\pm, n-1\rangle$ states. The quanta are continuously removed from the system until the ground state $|0, \downarrow\rangle$ is eventually reached.

Weak coupling regime

If $g \ll |\delta|, \gamma, \varkappa$, then the dynamics of the system is dominated by dissipation. The coherent coupling g can nearly be ignored, the levels within each multiplicity become degenerate, and consequently the two eigenstates per multiplicity differ only in their linewidths. The eigenvalues are given by:

$$\lambda_{\pm}^{(n)} = \hbar\omega\left(n - \frac{1}{2}\right) - i\hbar\left[\varkappa\left(n - \frac{1}{2}\right) + \frac{\gamma}{2} \mp \frac{|\delta|}{2} \pm \frac{g^2 n}{|\delta|}\right] \tag{2.20}$$

The two decay channels define the two possible limits.

1. The dynamics of the system may be *dominated by photon loss from the cavity* ($\varkappa \gg \gamma, g$). In such cases, the system can be described in terms of the so-called *bad-cavity limit*, with eigenvalues given by:

$$\lambda_+^{(n)} = \hbar\omega\left(n-\frac{1}{2}\right) - i\hbar\left[\varkappa\left(1+\frac{g^2}{\varkappa^2}\right)(n-1)+\gamma\left(1+\frac{g^2}{\varkappa\gamma}\right)\right] \tag{2.21}$$

$$\lambda_-^{(n)} = \hbar\omega\left(n-\frac{1}{2}\right) - i\hbar\varkappa\left(1-\frac{g^2}{\varkappa^2}\right)n \tag{2.22}$$

   If the multiplicities above the first excited state (i.e. $n > 1$) are never populated, the state of the system can be written as a product state. Atom and cavity subspaces are thus decoupled and evolve independently. The cavity decays at a very slightly inhibited rate $\varkappa' = \varkappa\left(1-g^2/\varkappa^2\right)$ while the atom decays at a higher spontaneous emission rate $\gamma' = \gamma(1+F)$. Here $F = g^2/(\varkappa\gamma)$ is the factor used by Purcell [38, 39] to quantify the enhancement of the spontaneous emission rate [40, 41] [1]. The fraction of photons spontaneously emitted into the cavity is given by

$$\beta = \frac{F}{F+1} \tag{2.23}$$

2. The dynamics of the system may alternatively be *dominated by the spontaneous emission from the atom*. The condition $\gamma \gg \varkappa, g$ is thus fulfilled, and the *bad-atom limit* is obtained. The eigenvalues for the system read

$$\lambda_+^{(n)} = \hbar\omega\left(n-\frac{1}{2}\right) - i\hbar\varkappa\left(1+\frac{g^2}{\varkappa\gamma}\right)n \tag{2.24}$$

$$\lambda_-^{(n)} = \hbar\omega\left(n-\frac{1}{2}\right) - i\hbar\left[\left(\varkappa-\frac{g^2}{\gamma}\right)(n-1)+\gamma\left(1-\frac{g^2}{\gamma^2}\right)\right] \tag{2.25}$$

   Following a similar line, if the multiplicities beyond the first are never populated, atom and cavity subspaces decouple. The cavity decays at an enhanced rate $\varkappa' = \varkappa(1+F)$ whereas the atom decays at a slightly decreased rate $\gamma' = \gamma\left(1-g^2/\gamma^2\right)$.

Intermediate coupling regime

In the region where $g \approx |\delta|/2$, the eigenvalues share characteristics from strong and weak coupling regimes. Namely, there will always be one critical manifold $n_{\text{crit}} = (\gamma-\varkappa)^2/(2g)^2$ that sets the boundary:

- the manifolds $n \leq n_{\text{crit}}$ have *degenerate eigenvalues but two different linewidths*, thus exhibiting characteristics of the weak coupling regime;
- the manifolds $n > n_{\text{crit}}$ have *non-degenerate eigenstates with the same linewidth*, the time evolution is similar to the strong coupling regime.

[1] The literature also employs the *cooperativity parameter*, C, which is a concept inherited from the language of optical bi-stability(see e.g. [25, 36]). It is the inverse of the critical number of atoms required to achieve appreciable quantum behaviour in a CQED system. For a single atom, it is related to the Purcell factor by $C = F/2$.

2.2 Three-level atom in a cavity

The model of a two-level atom in a cavity is not entirely sufficient to describe the experiments we performed, and at least a third atomic level must be considered. Nevertheless, there are special conditions that allow the reduction of the three-level system into an effective two-level atom coherently coupled to a cavity and under incoherent excitation.

The formalism for the two-level atom developed in the section 2.1 can be readily extended to a three-level atom in Λ-configuration, which brings the model closer to the experimental situation. It will be shown that under certain conditions the description of the system can be interpreted in terms of an effective two-level system, which can exhibit tunable coupling, from strong to weak coupling.

2.2.1 Extension of the model

The three-level atom that will be considered is composed of the two ground states $|S\rangle$ and $|D\rangle$, and of the excited state $|P\rangle$. As depicted in Figure 2.4a), the atom interacts with the resonator via the $D \leftrightarrow P$ transition. It also interacts with two lasers (*driving* and *recycling*) of angular frequencies ω_{driv} and ω_{recyc} via the $S \leftrightarrow P$ and $D \leftrightarrow P$ transitions, respectively. The cavity is assumed to be transparent at the wavelength of the $S \leftrightarrow P$ transition. Also, the recycling laser and the cavity can not directly interact (the respective axes are not co-linear).

Introducing the atomic lowering operators $\widehat{\sigma}_{sp} = |S\rangle\langle P|$ and $\widehat{\sigma}_{dp} = |D\rangle\langle P|$, the Hamiltonian for the system is given by:

$$\hat{H} = \hat{H}_0 + \hat{H}_c + \hat{H}_{\text{driv}} + \hat{H}_{\text{recyc}} \tag{2.26}$$

with

$$\hat{H}_0 = E_S\widehat{\sigma}_{ss} + E_P\widehat{\sigma}_{pp} + E_D\widehat{\sigma}_{dd} + \hbar\omega_c\hat{a}^\dagger\hat{a} \qquad \text{(bare Hamiltonian)} \tag{2.27}$$

$$\hat{H}_c = \hbar g\left(\hat{a}^\dagger\widehat{\sigma}_{dp} + \hat{a}\widehat{\sigma}_{pd}\right) \qquad \text{(ion - cavity interaction)} \tag{2.28}$$

$$\hat{H}_{\text{driv}} = \frac{\hbar\Omega_{\text{driv}}}{2}\left(\widehat{\sigma}_{sp}e^{i\omega_{\text{driv}}t} + \widehat{\sigma}_{ps}e^{-i\omega_{\text{driv}}t}\right) \qquad \text{(ion - driv. laser interaction)} \tag{2.29}$$

$$\hat{H}_{\text{recyc}} = \frac{\hbar\Omega_{\text{recyc}}}{2}\left(\widehat{\sigma}_{dp}e^{i\omega_{\text{recyc}}t} + \widehat{\sigma}_{pd}e^{-i\omega_{\text{recyc}}t}\right) \qquad \text{(ion - recyc. laser interaction)} \tag{2.30}$$

The first term $\hat{H}_0$ contains the energy terms for the bare atom and bare cavity. The cavity photons have an energy of $\hbar\omega_c$, while the energy of the bare atomic levels S, P and D are given by E_S, E_P and E_D, respectively.

In a similar fashion to the two-atom level, $\hat{H}_c$ is the Jaynes-Cummings for the atom-cavity interaction, relative to the $D \leftrightarrow P$ transition.

The atom-laser interaction Hamiltonians $\hat{H}_{\text{driv}}$ and $\hat{H}_{\text{recyc}}$ constitute the semi-classical approximation obtained from the Jaynes-Cummings Hamiltonian by assuming the laser light is described by coherent states with sufficiently high amplitudes such that they are not perturbed at all by any photon absorption or emission from the atom. The total energy of each laser field is thus constant and therefore irrelevant for the dynamics of the system. In addition, the creation and annihilation operators for the laser fields can be safely replaced by their expectation values.

The time dependence of the Hamiltonian $\hat{H}$ can be removed by performing a transformation to the *interaction picture*, by considering a general unitary transformation $\hat{U}$ that maps the state of system $|\psi\rangle$ into a new state $|\psi'\rangle = \hat{U}|\psi\rangle$. Then, $\hat{H}$ transforms into $\hat{H}'$ as $\hat{H}' = \hat{U}\hat{H}\hat{U}^\dagger - i\hbar\hat{U}d\hat{U}^\dagger/dt$.

In the particular case that $\hat{U} = \exp(i\hat{\mathcal{H}}_0 t/\hbar)$ and $\mathcal{H}_0$ is a time-independent operator, the transformation simplifies to $\hat{H}' = \hat{U}\hat{H}\hat{U}^\dagger - \mathcal{H}_0$.

For the case of the Hamiltonian (2.26), the appropriate unitary transformation is a product of three rotations:

$$\hat{U} = \exp\left(i\hat{a}^\dagger\hat{a}\omega_{\text{recyc}}t\right)\exp\left(i\widehat{\sigma}_{dd}\omega_{\text{recyc}}t\right)\exp\left(i\widehat{\sigma}_{ss}\omega_{\text{driv}}t\right) \tag{2.31}$$

The two rightmost rotations in the transformation can be interpreted as a switch to a frame that rotates synchronously with lasers in the $S \leftrightarrow P$ and $D \leftrightarrow P$ transitions. At this point, the operator $\hat{a}$ oscillates at a frequency ω_{recyc}. Therefore, the leftmost rotation in $\hat{U}$ is required to transform to a frame where the cavity interaction is also constant.

In the new basis and upon setting the energy reference at the state $|P\rangle$, the total Hamiltonian becomes

$$\begin{aligned}\hat{H}' = \hbar\left[\Delta_{\text{driv}}\widehat{\sigma}_{ss} + \Delta_{\text{recyc}}\widehat{\sigma}_{dd} + \left(\Delta_c - \Delta_{\text{recyc}}\right)\hat{a}^\dagger\hat{a}\right] \\ + \frac{\hbar\Omega_{\text{driv}}}{2}\left(\widehat{\sigma}_{sp} + \widehat{\sigma}_{ps}\right) + \hbar g\left(\hat{a}^\dagger\widehat{\sigma}_{dp} + \widehat{\sigma}_{pd}\hat{a}\right) + \frac{\hbar\Omega_{\text{recyc}}}{2}\left(\widehat{\sigma}_{dp} + \widehat{\sigma}_{pd}\right)\end{aligned} \tag{2.32}$$

where we have introduced the detunings :

$$\Delta_{\text{driv}} = (E_S - E_P)/\hbar - \omega_{\text{driv}} \tag{2.33}$$

$$\Delta_{\text{recyc}} = (E_D - E_P)/\hbar - \omega_{\text{recyc}} \tag{2.34}$$

$$\Delta_c = (E_D - E_P)/\hbar - \omega_c \tag{2.35}$$

2.2.2 Raman interaction picture

When both driving laser and cavity are detuned by the same amount $\Delta_c = \Delta_{\text{driv}} = \Delta$ from the upper level $|P\rangle$, a Raman resonance is expected to build up between the states $|S\rangle$ and $|D\rangle$.

The two-photon process can become the dominant coherent interaction if all one-photon processes such as off-resonant excitation of the $|P\rangle$ state or spontaneous decay of $|P\rangle$ to $|S\rangle$ and $|D\rangle$ (at rates γ_{SP} and γ_{DP}, respectively) are sufficiently suppressed, i.e. if $\Delta_{\text{driv}}, \Delta_c \gg \gamma_P, \Omega_{\text{driv}}, g$, with $\gamma_P = \gamma_{SP} + \gamma_{DP}$. In the following, we will see that under such conditions, the upper state can be eliminated and the system can be effectively reduced to a two-level system [42–45] [see Figure 2.4a)].

The reduction to a two-level system is obtained by performing yet another unitary transformation $\hat{U}$ that expresses the Hamiltonian in a frame where the Raman coupling is clearly stated. This corresponds to a frame that follows the dynamics of Raman process, which can be intuitively seen as two rotations on the two interactions (driving laser and atom-cavity). The required transformation [43, 44] is $\hat{U} = e^{\hat{S}}$, where

$$\hat{S} = \frac{\Omega_{\text{driv}}}{2\Delta_{\text{driv}}}\left(\widehat{\sigma}_{sp} - \widehat{\sigma}_{ps}\right) + \frac{g}{\Delta_c}\left(a^\dagger\widehat{\sigma}_{dp} - \widehat{\sigma}_{pd}a\right) \tag{2.36}$$

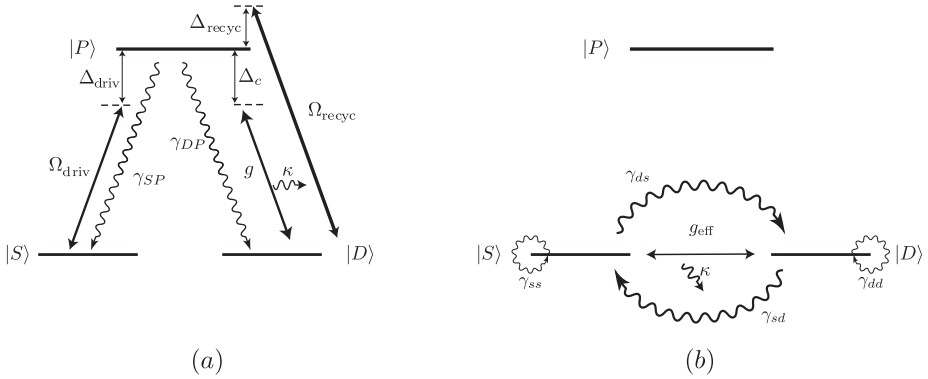

Figure 2.4: Energy level scheme for the three-level atom: in the canonical form (a); and effective two-level atom approximation (b). In a): The driving laser excites the $S \leftrightarrow P$ transition at a Rabi frequency Ω_{driv} and is detuned by Δ_{driv}. The cavity field interacts with the $D \leftrightarrow P$ transition at a Rabi frequency $2g$ and detuning of Δ_c. The recycling laser is detuned by Δ_{recyc} from the $D \leftrightarrow P$ transition and interacts with it at a Rabi frequency Ω_{recyc}. The P state decays via spontaneous emission to both S and D states at rates $2\gamma_{SP}$ and $2\gamma_{DP}$. The cavity field decays at a rate $\varkappa$. In b): When $\Delta_{\text{driv}} = \Delta_c = \Delta$, the states S and D are coupled at an effective Rabi frequency $g_{\text{eff}} = g\Omega_{\text{driv}}/(2\Delta)$. The driving laser can off-resonantly transfer population from S into P, which is followed by spontaneous emission into S or D. These incoherent processes can be replaced by direct decay rates γ_{ds} and γ_{ss}. Similarly, the recycling laser transfers population from D into P, which decays into either S or D. The equivalent direct processes are represented by the rates γ_{sd} and γ_{dd}.

The transformed Hamiltonian $\hat{H}'' = \hat{U}\hat{H}'\hat{U}^\dagger$ can be expanded in a power series in $\Delta_{\text{driv}}^{-1}$ and Δ_c^{-1} by using the well-known Baker-Campbell-Hausdorff formula

$$\hat{H}'' = e^{\hat{S}}\hat{H}'e^{-\hat{S}} = \hat{H}' + \left[\hat{S},\hat{H}'\right] + \frac{1}{2!}\left[\hat{S},\left[\hat{S},\hat{H}'\right]\right] + \ldots \tag{2.37}$$

Provided that $\Omega_{\text{driv}}, g \ll \Delta_c, \Delta_{\text{driv}}$, it is sufficient to keep only the first-order

terms:

$$\hat{H}'' = \hbar\Delta_{\text{driv}}\hat{\sigma}_{ss} + \hbar\Delta_{\text{recyc}}\hat{\sigma}_{dd} + \hbar\left(\Delta_c - \Delta_{\text{recyc}}\right)\hat{a}^\dagger\hat{a} + \underbrace{\frac{\hbar\Omega_{\text{recyc}}}{2}\left(\hat{\sigma}_{dp} + \hat{\sigma}_{pd}\right)}_{\text{recycling laser}} + \tag{2.38}$$

$$+ \underbrace{\frac{\hbar g\Omega_{\text{driv}}}{4}\left(\frac{1}{\Delta_{\text{driv}}} + \frac{1}{\Delta_c}\right)\left(\hat{a}^\dagger\hat{\sigma}_{sd} + \hat{\sigma}_{ds}\hat{a}\right)}_{\text{ion-cavity Raman coupling}} + \tag{2.39}$$

$$+ \underbrace{\frac{\hbar\Omega_{\text{driv}}^2}{4\Delta_{\text{driv}}}\left(\hat{\sigma}_{ss} - \hat{\sigma}_{pp}\right)}_{\text{dynamic Stark shift due to driving laser}} + \underbrace{\frac{\hbar g^2}{\Delta_c}\left[\hat{a}^\dagger\hat{a}\left(\hat{\sigma}_{dd} - \hat{\sigma}_{pp}\right) - \hat{\sigma}_{pp}\right]}_{\text{dynamic Stark shift due to cavity}} + \tag{2.40}$$

$$+ \underbrace{\frac{\hbar g\Omega_{\text{recyc}}}{2\Delta_c}\left(\hat{a}^\dagger + \hat{a}\right)\left(\hat{\sigma}_{dd} - \hat{\sigma}_{pp}\right)}_{\text{scattering of recycling laser into the cavity}} + \underbrace{\frac{\hbar\Omega_{\text{driv}}\Omega_{\text{recyc}}}{4\Delta_{\text{driv}}}\left(\hat{\sigma}_{sd} + \hat{\sigma}_{ds}\right)}_{\text{driving-recycling Raman coupling}} + \tag{2.41}$$

$$+ \hat{\mathcal{O}}(\Delta_c^{-2}, \Delta_{\text{driv}}^{-2})$$

The terms in (2.38) are not affected by the transformation.

The transformation reveals the effective Raman coupling, which is expressed by the term (2.39). In this process, one photon is absorbed from the driving laser, leading to a transition from $|S\rangle$ to $|D\rangle$ and to the creation of one photon in the cavity field; because the Raman coupling is a coherent process, the reverse also occurs. For $\Delta = \Delta_{\text{driv}} = \Delta_c$, the Raman-Rabi frequency [2] for the transition $|S, n-1\rangle \leftrightarrow |D, n\rangle$ is thus $\Omega_{\text{eff}}^{(n)} = \hbar g\Omega_{\text{driv}}\sqrt{n}/(2\Delta)$.

Provided the interaction of the laser and the cavity is sufficiently weak, the bare states are only slightly perturbed by an admixture due to the dressing, suffering an energy shift. The terms (2.40) show the light shifts for the atomic dressed states. The driving laser introduces a light shift of $\hbar\Omega_{\text{driv}}^2/(4\Delta_{\text{driv}})$ to both $|S\rangle$ and $|P\rangle$ states, while the cavity field contributes with a light shift of $\hbar g^2/\Delta_c$ to both $|P\rangle$ and $|D\rangle$ states.

Finally, (2.41) reveals two other possible interactions. The first term corresponds to a Raman scattering process that is characterised by the exchange of one photon between the cavity field and the recycling laser, which only occurs if the cavity detuning matches the detuning of the recycling laser ($\Delta_c = \Delta_{\text{recyc}}$). The second term of (2.41) reveals an additional Raman interaction between the S and D states, established by the driving and recycling lasers if the resonance condition $\Delta_{\text{recyc}} = \Delta_{\text{driv}}$ is fulfilled, which allows the population of the S and D states to be exchanged independently of the atom-cavity interaction.

[2] The transformation to the Raman interaction picture can be performed exactly [44]. The exact Raman-Rabi frequency is given by:

$$\Omega_{\text{eff}}^{(n)} = \frac{1}{2}\cdot\frac{g\sqrt{n}\cdot\Omega_{\text{driv}}}{4g^2n + \Omega_{\text{driv}}^2}\cdot\left(\sqrt{\Delta^2 + \Omega_{\text{driv}}^2 + 4g^2n} - \Delta\right) \tag{2.42}$$

2.2.3 Effective two-level system

The complete elimination of the $|P\rangle$ state from the description will now lead to an effective two-level system.

The analysis of Figure 2.4 already allows the intuitive understanding on how this elimination is to be performed, by comparing the processes using the bare three-level atom picture [Figure 2.4a)] and the effective two-level atom picture [Figure 2.4b)].

In the absence of the recycling laser, $\Omega_{\text{recyc}} = 0$, the state $|P\rangle$ becomes irrelevant for the dynamics. An effective Hamiltonian can be built using only the dressed $|S\rangle$ and $|D\rangle$ states, the cavity field and the Raman interaction. Such a system can be mapped to a two-level atom in a quantised cavity field :

$$\hat{H}_{\text{eff}} = \hbar\left[\Delta - \frac{g^2}{\Delta}\right]\hat{a}^\dagger\hat{a} + \hbar\left[\Delta + \left(\frac{\Omega_{\text{driv}}}{2\Delta}\right)^2 - \frac{g^2}{\Delta}\hat{a}^\dagger\hat{a}\right]\widehat{\sigma}_{ss} + \\ + g_{\text{eff}}\left(\hat{a}^\dagger\widehat{\sigma}_{sd} + \widehat{\sigma}_{ds}\hat{a}\right) \quad (2.43)$$

As we will explore later, the recycling laser is fundamental and cannot be removed from the system. However, its existence formally adds the off-diagonal terms $\widehat{\sigma}_{dp} + \widehat{\sigma}_{pd}$ in (2.38), which prevent the immediate identification of an effective two-level system, because the $|P\rangle$ state cannot be factored out.

An approximation is now necessary to replace the action of the coherent recycling laser with a series of incoherent process, effectively removing the $|P\rangle$ state from the theoretical treatment. Such procedure allows for a simplified understanding of the dynamics of the system.

Inclusion of dissipative processes

The recycling laser transfers population from $|D\rangle$ to $|P\rangle$, which is followed by spontaneous emission to either $|S\rangle$ or $|D\rangle$ states. The spontaneous decay mechanisms happen at rates much faster than the Raman interaction. Provided the recycling laser is not at the same detuning as either the driving laser or the cavity, its action can be coarsely approximated by two incoherent processes, namely:

1. A process for direct spontaneous emission from D to S, at a rate $2\gamma_{sd}$, with

$$\gamma_{sd} \approx \frac{\Omega^2_{\text{recyc}}/4}{\Delta^2_{\text{recyc}} + \gamma_p^2 + \Omega^2_{\text{recyc}}/2} \cdot \gamma_{SP} \quad (2.44)$$

   which approximates an excitation of the P state that is followed by spontaneous emission into S [3].

2. A phase noise mechanism in the D state, at a rate $2\gamma_{dd}$, with

$$\gamma_{dd} \approx \frac{\Omega^2_{\text{recyc}}/4}{\Delta^2_{\text{recyc}} + \gamma_p^2 + \Omega^2_{\text{recyc}}/2} \cdot \gamma_{DP} \quad (2.45)$$

   which approximates an excitation of the P state that is followed by spontaneous emission back into D.

[3] Please note our convention for the notation of the decay rates: γ_{ab} should be read as *the decay rate from b to a*.

The approximate expressions are obtained from the theory of a two-level atom (see e.g. [46]).

This formalism outlines the introduction of the dissipative processes of the effective two-level system and can be completed by including the spontaneous emission from the P state due to off-resonant excitation of the driving laser, by adding the following processes (see Figure 2.4):

1. Direct spontaneous emission from S to D, at a rate $2\gamma_{ds}$, with

$$\gamma_{ds} \approx \frac{\Omega_{\text{driv}}^2/4}{\Delta_{\text{driv}}^2 + \gamma_p^2 + \Omega_{\text{driv}}^2/2} \cdot \gamma_{DP} \approx \left(\frac{\Omega_{\text{driv}}}{2\Delta_{\text{driv}}}\right)^2 \cdot \gamma_{DP} \tag{2.46}$$

   corresponding to a process in which the driving laser off-resonantly excites the P state and which is followed by spontaneous emission into D.

2. Phase noise in the S state, at a rate $2\gamma_{ss}$, with

$$\gamma_{ss} \approx \frac{\Omega_{\text{driv}}^2/4}{\Delta_{\text{driv}}^2 + \gamma_p^2 + \Omega_{\text{driv}}^2/2} \cdot \gamma_{SP} \approx \left(\frac{\Omega_{\text{driv}}}{2\Delta_{\text{driv}}}\right)^2 \cdot \gamma_{SP} \tag{2.47}$$

   corresponding to a process in which the driving laser off-resonantly excites the P state and which is followed by spontaneous emission back into S.

Figure 2.5 illustrates the final effective two-level system. If the system is not externally driven by the recycling laser, $\gamma_{sd} = 0$, the system is analogous to the one discussed in section 2.1.3 and the dissipative processes will eventually leave the system in the state $|D,0\rangle$, which is the ground state of the system. The emission of a photon into the cavity mode is regarded as the result of the coherent interaction of the atom with the vacuum-stimulated Raman interaction, at a rate g_{eff}, while the phase noise processes (at rates γ_{ss} and γ_{dd}) dampen the coherence in the system. In the presence of the recycling laser, the system behaves as if it was interacting with an external hot reservoir.

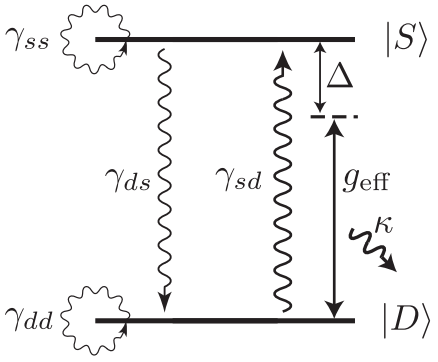

Figure 2.5: Effective two-level system with dissipation in the bare-atom representation. The upper level S is incoherently pumped at a rate $2\gamma_{sd}$ and decays spontaneously at a rate $2\gamma_{ds}$. The cavity couples coherently with the $S \leftrightarrow D$ transition at the Rabi frequency $2g_{\text{eff}}$. The photons stored in the cavity decay at a rate $2\varkappa$. The processes acting on the states D and S at rates $2\gamma_{dd}$ and $2\gamma_{ss}$ introduce phase noise.

If the formalism developed in section 2.1 is now applied to the effective two-level system, the reduced linewidth associated with the vacuum-stimulated Raman transition is given by γ_{eff}:

$$\gamma_{\text{eff}} \approx \gamma_{ss} + \gamma_{sd} + \gamma_{ds} + \gamma_{dd} \tag{2.48}$$

while the Rabi frequency is given by

$$\Omega_{\text{eff}} \approx \frac{g\Omega_{\text{driv}}}{2\Delta_{\text{driv}}} \tag{2.49}$$

The Rabi frequency normalised to the linewidth ($\Omega_{\text{eff}}/\gamma_{\text{eff}}$) indicates the dominant type of photon emission: spontaneous or stimulated emission.

When the dissipative processes dominate over the atom-cavity coherent interaction, then $\Omega_{\text{eff}}/\gamma_{\text{eff}} < 1$ and the atom emits photons into the cavity mode mostly via spontaneous decay. Such situations can be easily obtained with high intensities of the driving and recycling lasers: the excessive excitation leads to a higher occupation of the P state which in turn leads to higher γ_{eff}.

In contrast, at low intensities of the driving and recycling lasers, the effective atom-cavity coupling Ω_{eff} competes with the dissipative processes: we have $\Omega_{\text{eff}}/\gamma_{\text{eff}} > 1$ and the photons are emitted into the cavity mode mostly via stimulated emission.

Single-atom laser

In the absence of the recycling laser, the system behaves as the two-level atom coupled to a cavity described in the previous sections, the ground state being $|D, 0\rangle$. Since the effective Rabi frequency of the coherent coupling depends on the parameters of the driving laser, the dynamics of the system can be tuned by playing with the parameters of the driving laser: the same device can be operated in both strong and weak coupling regimes.

As the recycling laser is turned on, an incoherent pumping mechanism is introduced, which can be used to excite the S manifold. In other words, population inversion becomes possible. As the cavity becomes populated, a photon stream leaves the resonator through the mirrors.

The atom-cavity system can be thus formally understood in terms of an effective two-level atom in a cavity coupled to an external reservoir. Nevertheless, this approximation is valid only as long as the recycling mechanism is slow and the $D \leftrightarrow P$ transition is not broadened: the level structure is modified for a strong interaction with the recycling laser.

The immediate question is: can such a system act as a laser? The literature has considered this topic extensively.

In 1990, Agarwal and Dutta Gupta [47] solved the quantum model above, but neglected the phase noise mechanisms. They were able to show that such a system could output non-classical light. In particular, depending on the ratio between the atom-cavity coupling strength and the cavity decay rate, they showed that the photon statistics could change from sub- to super-Poissonian nature. Moreover, they demonstrated that atom and cavity field are strongly correlated.

In 1992, Mu and Savage [32] provided the theoretical proof that a single atom coupled to a cavity and subject to external excitation can produce laser light. They considered two-, three- and four-level atoms, and compared semiclassical and quantum models. Unlike macroscopic lasers, they found no clear evidence of a threshold,

which is typically expected to be a sharp phase transition from weakly excited thermal light to coherent light at a particular pump power.

In 1997, Meyer, Briegel and Walther [33] considered the specific case of a $^{40}Ca^{+}$ and found several features: the development of two thresholds, sub-Poissonian statistics, lasing without inversion and self-quenching.

In 2004, McKeever et al. [48, 49] demonstrated experimentally a single-atom laser operating in the strong coupling regime.

We conclude this introductory section on the single ion laser by hinting that the measurements discussed in chapter 8 show that a single ion coupled to a cavity displays a behaviour that resembles a semiclassical laser on threshold. Our numerical simulations show that there is a smooth transition from a quantum laser with sub-Poissonian statistics to a semiclassical laser on threshold. If some technical limitations are removed, both situations can be implemented.

2.3 Photon statistics

The quantum nature of light enforces a statistical description of its properties. The radiation field must therefore be described in terms of electric field operators $\hat{E}^{\pm}(t)$. The observation of the photon stream of a given light source with single-photon detectors allows the determination of the moments of the photon counting distribution, as well as the time-resolved photon correlation functions, which may be used to obtain some information about the internal state of the source.

Moments

The first moment of the photon counting distribution $\overline{n}$ is the average count rate. The theory of the photoelectric detection of light [50, 51] states that it is proportional to the average of the normally-ordered intensity of the light field:

$$\overline{n} = \sum_n n \cdot p_n \equiv \frac{\eta}{\hbar\omega} \langle : I(t) : \rangle = \frac{\eta \epsilon_0}{2\hbar\omega} \langle \hat{E}^-(t) \hat{E}^+(t) \rangle \tag{2.50}$$

where p_n is the probability of detecting n photons, $\hbar\omega$ is the energy of one photon, η is the detection efficiency and the brackets $\langle \cdot \rangle$ indicate an average over the total measurement time T. The normal ordering (denoted by the colons inside the brackets) reflects the fact that the detector works by absorbing photons.

The second moment of the photon counting distribution $\overline{n^2}$ is similarly given by

$$\overline{n^2} = \sum_n n^2 \cdot p_n \equiv \left(\frac{\eta}{\hbar\omega}\right)^2 \langle : I^2(t) : \rangle = \left(\frac{\eta \epsilon_0}{2\hbar\omega}\right)^2 \langle \hat{E}^-(t) \hat{E}^-(t) \hat{E}^+(t) \hat{E}^+(t) \rangle \tag{2.51}$$

and is related to the variance of the photon counting distribution by $\overline{(\Delta n)^2} = \overline{(n - \overline{n})^2} = \overline{n^2} - \overline{n}^2$. The variance is usually normalised to the variance of a Poisson distribution with the same average count rate, for which $\overline{\Delta n^2} = \overline{n}$. The resulting value is known as the Fano factor F:

$$F := \frac{\overline{\Delta n^2}}{\overline{n}} = \frac{\overline{n^2} - \overline{n}^2}{\overline{n}} \tag{2.52}$$

The Mandel Q parameter is also commonly used in the literature in the same context. The relationship between the two quantities is given by $Q = F - 1$. Positive values of the Mandel Q parameter indicate a super-Poissonian distribution, while negative values indicate a sub-Poissonian photon counting distribution.

Time-resolved correlations

If the photon detection times are well resolved, it is possible to obtain correlations from coincidence measurements.

The first-order correlation function is a correlation of the amplitude of the electric field and is classically defined as

$$g^{(1)}(t, t+\tau) = \frac{\langle E(t+\tau) E(t) \rangle}{\langle I(t) \rangle^{1/2}} \tag{2.53}$$

where $E(t)$ and $I(t)$ are the amplitude and intensity of the electric field at time t, respectively. However, a single-photon detector is sensitive to the intensity of the

radiation field and cannot be directly used to determine the electric field. These detectors usually require the use of techniques based on the interference of two electric fields, such as homodyne and heterodyne configurations.

In the experiments discussed in this thesis, the second-order correlation function (also called intensity correlation function) was measured instead. In a classical framework it assumes the simple form:

$$g^{(2)}(t,t+\tau)=\frac{\langle I(t+\tau)I(t)\rangle}{\langle I(t)\rangle^2} \tag{2.54}$$

Given that the intensity is proportional to the probability of a photoelectric detection, the classical second-order correlation function can be rewritten as

$$g^{(2)}(t,t+\tau)=\frac{p(t+\tau,t)}{p^2(t)}=\frac{p(t+\tau|t)}{p(t)} \tag{2.55}$$

where

$p(t)$ is the probability of detecting a photon at time t,

$p(t+\tau,t)$ is the *joint probability* of detecting photons at times t and $t+\tau$,

$p(t+\tau|t)$ is the conditional probability of detecting a photon at time $t+\tau$ *provided* one photon was detected at time t.

In other words, the second-order correlation function can be classically understood as a normalised conditioned probability. The measurement of the joint probability for two photoelectric detections can be performed in a setup similar to the experiments by Hanbury-Brown and Twiss, where the light is decomposed by a beam splitter in two parts and the photoelectric events of the two detectors are recorded in time.

The experiments discussed in this thesis, however, require the use of the quantum framework. Recalling that $\hat{E}^{\pm}(t)$ are the electric field operators in the Schrödinger picture for the radiation field under consideration, the second-order correlation function is given by:

$$g^{(2)}(t,t+\tau)=\frac{\langle\hat{E}^-(t)\hat{E}^-(t+\tau)\hat{E}^+(t+\tau)\hat{E}^+(t)\rangle}{\langle\hat{E}^-(t)\hat{E}^+(t)\rangle\,\langle\hat{E}^-(t+\tau)\hat{E}^+(t+\tau)\rangle} \tag{2.56}$$

Here, the normal and time-ordering play a significant role [52, 53].

If the light source is (statistically) stationary, its second-order correlation function depends only on the time difference τ. This is formally obtained by letting $t\to\infty$:

$$g^{(2)}(\tau)=\lim_{t\to\infty}g^{(2)}(t,t+\tau)=\lim_{t\to\infty}\frac{\langle\hat{E}^-(t)\hat{E}^-(t+\tau)\hat{E}^+(t+\tau)\hat{E}^+(t)\rangle}{\langle\hat{E}^-(t)\hat{E}^+(t)\rangle^2} \tag{2.57}$$

It is simple to verify that the correlation function $g^{(2)}(\tau)$ obeys the properties of time symmetry ($g^{(2)}(-\tau)=g^{(2)}(\tau)$) and non-negativity ($g^{(2)}(\tau)\geq 0$). It can also be easily shown that the Mandel Q parameter is intimately linked with the correlation at zero delay time:

$$Q=\overline{n}\left[g^{(2)}(0)-1\right] \tag{2.58}$$

Examples

Figure 2.6 shows typical single-mode second-order correlation functions for three types of light sources [36]:

Thermal light The discovery of the Hanbury-Brown-Twiss effect [1, 2] led to the clarification that thermal sources (such as stars) display *photon bunching*: positive correlation at short delay times τ, i.e. $g^{(2)}(0) \geq g^{(2)}(\tau)$ for any τ. These correlations disappear at long delay times τ, i.e, $g^{(2)}(\tau \to \infty) = 1$. Consequently, $g^{(2)}(0) \geq 1$ and $Q > 0$ which implies that thermal photons follow *super-Poissonian statistics*.

The dashed line in Figure 2.6 shows a thermal chaotic source, for which $g^{(2)}(\tau) = 1 + e^{-\gamma|\tau|}$.

Non-classical light The quantum mechanical treatment is required for *non-classical* photon sources like the resonance fluorescence of a single atom in free space [3] (see dash-dotted line in Figure 2.6). These sources may display *photon anti-bunching* ($g^{(2)}(0) \leq g^{(2)}(\tau)$) and can even follow sub-Poissonian statistics ($g^{(2)}(0) \leq 1$).

Another quite simple example of non-classical light would be the case of a stationary Fock state with N photons, which is characterised by a second-order correlation function $g^{(2)}(\tau) = 1 - 1/N$: the photon counting distribution follows sub-Poissonian statistics.

Laser light The classical concept of a laser consists of a perfectly harmonic stationary electric field $E(t) = E_0 e^{i\omega t}$, for which $g^{(2)}(\tau) = 1$. In quantum theory, laser light is a coherent state of amplitude α: $|\alpha\rangle$. The coherent states are characterised by the relations $\hat{a}|\alpha\rangle = \alpha|\alpha\rangle$ and $\hat{a}^\dagger|\alpha\rangle = \alpha^*|\alpha\rangle$. These relations suffice to establish that $g^{(2)}(\tau) = 1$.

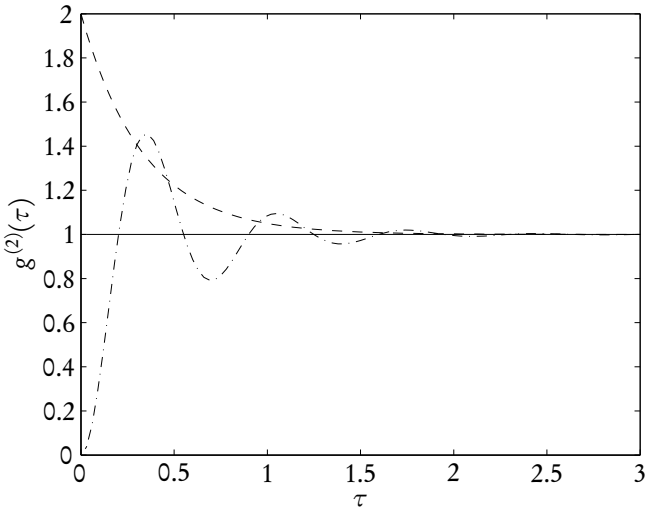

Figure 2.6: Calculated second-order correlation function $g^{(2)}(\tau)$ for a single mode and three light sources: chaotic thermal source (dashed line), single atom resonance fluorescence (dash-dotted line), and laser light or light in a coherent source (solid line).

Chapter 3

Model

While in the previous chapter we explored the general physical picture using fictitious two-level and three-level atoms, the goal of this chapter is to bridge the gap between the conceptual and the real world. This chapter therefore presents the realistic theoretical model used to describe the experimental results obtained with single $^{40}Ca^{+}$ ions. The relevant level structure of $^{40}Ca^{+}$ is first presented and a model based on a density matrix formalism using eight Zeeman states is constructed. We emphasise the derivation of the Hamiltonian operator.

3.1 The calcium ion

Calcium is an earth-alkaline element with two valence electrons. It is the fifth most abundant element in the Earth's crust. Upon the removal of one electron, the dynamics of the calcium ion is determined in terms of the possible transitions of the valence electron. The experiments use $^{40}Ca^{+}$, which is the most abundant calcium isotope, making up 97% of the natural occurrence. As most other stable calcium isotopes, $^{40}Ca^{+}$ has zero nuclear spin ($I = 0$), the sole exception being $^{43}Ca^{+}$, for which $I = 7/2$.

The relevant lowest lying levels of $^{40}Ca^{+}$ are presented in Figure 3.1, while the parameters are presented in Table 3.1.

Transition	λ_{air} (nm)	τ	$\gamma/(2\pi)$
$S_{1/2} \leftrightarrow P_{1/2}$	397.847	7.7(2) ns	10.3(3) MHz
$S_{1/2} \leftrightarrow D_{3/2}$	732.389	1.176(11) s [54]	67.6(6) mHz
$S_{1/2} \leftrightarrow D_{5/2}$	729.147	1.168(7) s [55]	68.1(4) mHz
$P_{1/2} \leftrightarrow D_{3/2}$	866.214	94.3 ns	0.844 MHz
$P_{3/2} \leftrightarrow D_{3/2}$	849.802	901 ns	88.3 kHz
$P_{3/2} \leftrightarrow D_{5/2}$	854.209	101 ns	0.789 MHz

Table 3.1: Wavelength in air (λ_{air}), lifetime (τ) and coherence decay rate (γ) for the relevant transitions of $^{40}Ca^{+}$.

As outlined in Chapter 2, a lambda level scheme is used to implement the effective coupling between the ion and the cavity mode. By noting that the lifetime of the metastable D levels is far higher than those of the P levels, three lambda

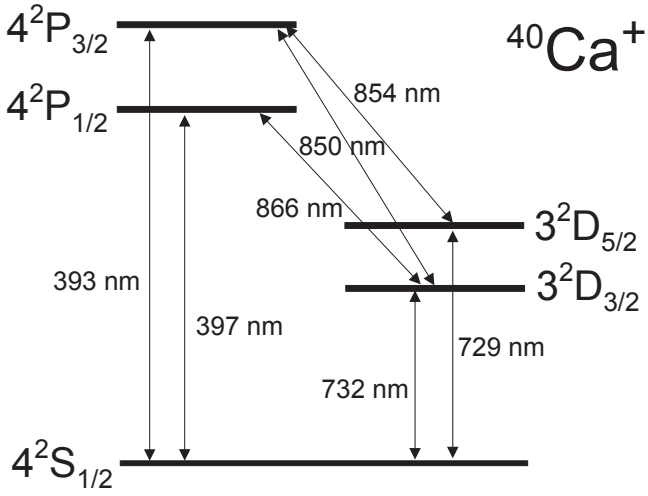

Figure 3.1: Lowest lying energy levels of $^{40}Ca^+$, along with the wavelengths of the dipole- and quadrupole-allowed transitions

schemes can be considered. The first is composed by the levels $S_{1/2} \leftrightarrow P_{1/2} \leftrightarrow D_{3/2}$, while the second and the third are composed by the states $S_{1/2} \leftrightarrow P_{3/2} \leftrightarrow D_{3/2}$ and $S_{1/2} \leftrightarrow P_{3/2} \leftrightarrow D_{5/2}$, respectively. The latter two cases are plagued by an additional transition: in order to avoid population trapping in the wrong D state, additional lasers sources are required.

Due its simplicity, the experiments on photon statistics discussed in this thesis made use of the $S_{1/2} \leftrightarrow P_{1/2} \leftrightarrow D_{3/2}$ lambda system. The discussion on the energy level structure of $^{40}Ca^+$ will therefore be restricted to these three manifolds, comprising a total of eight levels.

3.2 Eight-level atom in a cavity

3.2.1 Zeeman structure

In a weak magnetic field of magnitude B, the Zeeman effect lifts the degeneracy of the energy levels. As depicted in Figure 3.2, the manifolds $S_{1/2}$, $P_{1/2}$ and $D_{3/2}$ are split into two, two and four levels respectively. We must therefore consider a total of eight levels.

The energy splitting within the various manifolds is given by:

$$\Delta E_{j,m_j} = m_j g_j \mu_B B \tag{3.1}$$

where $\mu_B = 9.3 \times 10^{-24} \mathrm{J} \cdot \mathrm{T}^{-1} = 1.4\ \mathrm{MHz} \cdot \mathrm{G}^{-1}$ is the Bohr magneton and g_j is the Landé g-factor. The latter can be calculated from the quantum numbers using the expression $g_j = 1 + [j(j+1) - l(l+1) + s(s+1)] / [2j(j+1)]$, and reads $g(S_{1/2}) = 2$, $g(P_{1/2}) = 2/3$ and $g(D_{3/2}) = 4/5$.

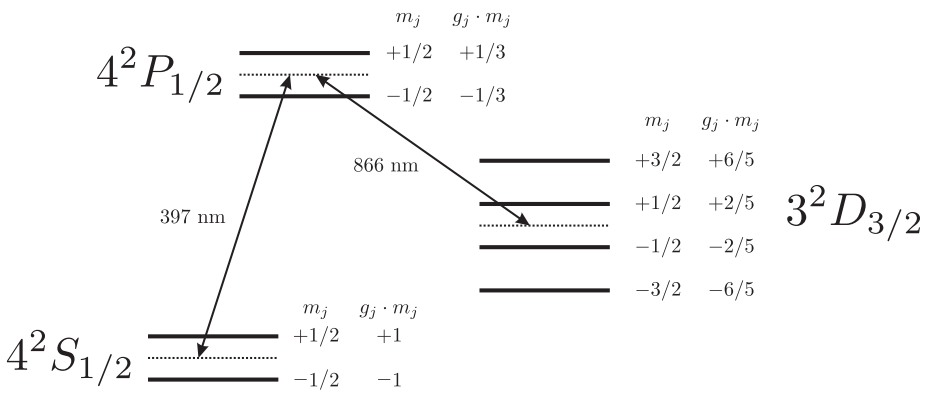

Figure 3.2: $^{40}Ca^{+}$ Zeeman structure for the three lowest-lying states, revealing a total of eight levels

3.2.2 Electric dipole interaction

The Hamiltonian for the atom-light interaction in the dipole approximation is written as the scalar product of the vectorial dipole moment operator $\widehat{\mathbf{d}}$ with the electric field operator $\widehat{\mathbf{E}}$:

$$\hat{H}_I = -\widehat{\mathbf{d}} \cdot \widehat{\mathbf{E}} \tag{3.2}$$

Dipole moment

The vectorial dipole operator $\widehat{\mathbf{d}} = e\widehat{\mathbf{r}}$ can be expanded in terms of projectors acting on the atomic subspace:

$$\hat{\mathbf{d}} = \sum_{U,V} \sum_{m_u,m_v} \left\langle U, m_u \left| e\widehat{\mathbf{r}} \right| V, m_v \right\rangle \cdot |V, m_v\rangle \langle U, m_u| \tag{3.3}$$

$$= \frac{1}{2} \sum_{U,V} \sum_{m_u,m_v} \mu_{U,V} \left(\widehat{\sigma}_{U,m_u;V,m_v} + \widehat{\sigma}_{V,m_v;U,m_u} \right) \mathbf{d}_{U,m_u}^{V,m_v} \tag{3.4}$$

Here, $\widehat{\sigma}_{U,m_u;V,m_v}$ is the projector associated to a transition from the state $|V, m_v\rangle$ to the state $|U, m_u\rangle$ and $\mu_{U,V}$ is the reduced dipole moment for the transition between the manifolds U and V, with $U, V = S_{1/2}, P_{1/2}, D_{3/2}$. It is related to the natural lifetime $\tau_{U,V} = (2\gamma_{U,V})^{-1}$ of the $U \leftrightarrow V$ transition by

$$\gamma_{U,V} = \frac{1}{2} \frac{1}{4\pi\varepsilon_0} \frac{4\omega^3 |\mu_{U,V}|^2}{3\hbar c^3} = \frac{4\pi^2 c^3}{3\hbar\varepsilon_0 \lambda^3} |\mu_{U,V}|^2 \tag{3.5}$$

where ω and λ are the angular frequency and wavelength associated with the transition $U \leftrightarrow V$.

The geometric component of $\hat{\mathbf{d}}$ is contained in the various vectors $\mathbf{d}_{U,m_u}^{V,m_v}$:

$$\mathbf{d}_{U,m_u}^{V,m_v} = \langle j_U, m_u; 1, m_v - m_u | j_V, m_v \rangle \cdot \begin{cases} \vec{\epsilon}_+ & \text{if } m_v = m_u + 1 \\ \vec{\epsilon}_0 & \text{if } m_v = m_u \\ \vec{\epsilon}_- & \text{if } m_v = m_u - 1 \\ 0 & \text{otherwise} \end{cases} \tag{3.6}$$

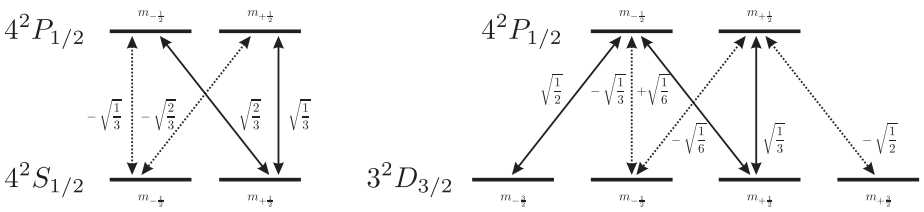

Figure 3.3: Clebsch-Gordan coefficients for the $S \leftrightarrow P$ and $D \leftrightarrow P$ transitions. The solid (dotted) lines correspond to coefficients with positive (negative) sign.

Here, $\langle j_U, m_u; 1, m_v - m_u | j_V, m_v \rangle$ is the Clebsch-Gordan coefficient associated with the dipole-allowed transition $|U, m_u\rangle \leftrightarrow |V, m_v\rangle$ which is given by

$$\langle j_U, m_u; 1, m_v - m_u | j_V, m_v \rangle = (-1)^{2(j_U + m_v)} \times \times \sqrt{\frac{2\,(2j_U)!\,(j_V - m_v)!\,(j_V + m_v)!}{(2j_V)!\,(j_U - m_u)!\,(j_U + m_u)!\,(m_u - m_v + 1)!\,(m_v - m_u + 1)!}} \tag{3.7}$$

The Clebsch-Gordan coefficients for the $S_{1/2} \leftrightarrow P_{1/2}$ and $D_{3/2} \leftrightarrow P_{1/2}$ transitions are represented in Figure 3.3. In these processes, a photon is emitted or absorbed, with its polarisation being represented by the vectors $\vec{\epsilon}_\pm = \left(\mathbf{u}_x \pm i\mathbf{u}_y\right)/\sqrt{2}$ and $\vec{\epsilon}_0 = \mathbf{u}_z$. These vectors are orthonormal and therefore obey the relations $\vec{\epsilon}_0 \cdot \vec{\epsilon}_0 = \vec{\epsilon}_\pm \cdot \vec{\epsilon}_\pm = 1$ and $\vec{\epsilon}_0 \cdot \vec{\epsilon}_\pm = \vec{\epsilon}_\pm \cdot \vec{\epsilon}_\mp = 0$. It is implied that the magnetic field is aligned with the z axis ($\mathbf{B} = B\mathbf{u}_z$).

Quantised electric field

At a given position $\mathbf{r}$ and at a time t, the electric field operator $\hat{\mathbf{E}}$ for a plane-wave at an angular frequency ω propagating in the direction $\mathbf{k}$ can be expressed in its second-quantisation form as:

$$\hat{\mathbf{E}}(\mathbf{k}, \mathbf{r}, t) = \sqrt{\frac{\hbar\omega}{2\varepsilon_0 V}} \left(\hat{a} e^{-i\omega t + i\mathbf{k}\cdot\mathbf{r}} + \hat{a}^\dagger e^{i\omega t - i\mathbf{k}\cdot\mathbf{r}}\right) \vec{\epsilon} \tag{3.8}$$

where V is the quantisation volume, $\hat{a}$ and $\hat{a}^\dagger$ are the photon creation and annihilation operators, $\mathbf{k}$ is the propagation direction, and $\vec{\epsilon}$ is the polarisation of the electric field. Note that the electric field operator acts on the photon subspace.

Atom-cavity electric dipole interaction

The electric field inside a linear resonator can be seen as the superposition of two counterpropagating plane waves with equal amplitude and polarisation. Therefore, the operator for the electric field inside a cavity is given by:

$$\hat{\mathbf{E}}_{\text{cavity}}(\mathbf{r}, t) = \hat{\mathbf{E}}(\mathbf{k}, \mathbf{r}, t) + \hat{\mathbf{E}}(-\mathbf{k}, \mathbf{r}, t) \tag{3.9}$$

$$= \sqrt{\frac{\hbar\omega}{2\varepsilon_0 V}} \cos(\mathbf{k}\cdot\mathbf{r}) \left(\hat{a} e^{-i\omega t} + \hat{a}^\dagger e^{i\omega t}\right) \vec{\epsilon} \tag{3.10}$$

Also, if the cavity has length L and holds a Gaussian mode of waist w_0, then the mode volume is given by $V = L\pi w_0^2/4$ and the electric field at the position of the waist $\mathbf{r}_0$ is:

$$\hat{\mathbf{E}}_{\text{cavity}}(\mathbf{r},t) = \sqrt{\frac{2\hbar\omega}{\varepsilon_0 L\pi w_0^2}}\cos(\mathbf{k}\cdot\mathbf{r}_0)\left(\hat{a}e^{-i\omega t} + \hat{a}^\dagger e^{i\omega t}\right)\vec{\epsilon} \tag{3.11}$$

By using the dipole moment operator, it is now possible to determine the interaction Hamiltonian in the electric dipole approximation for the $U \longleftrightarrow V$ transition:

$$\hat{H}_{U,V} = -\hat{\mathbf{d}}\cdot\hat{\mathbf{E}} = \sum_{m_u=-j_U}^{j_U}\sum_{m_v=m_u-1}^{m_u+1}\hat{H}_{U,m_u;V,m_v} \tag{3.12}$$

$$\hat{H}_{U,m_u;V,m_v} = \hbar g_{U,V}\left(\vec{\epsilon}\cdot\mathbf{d}_{U,m_u}^{V,m_v}\right)\left(\widehat{\sigma}_{U,m_u;V,m_v} + \widehat{\sigma}_{V,m_v;U,m_u}\right)\left(\hat{a}e^{-i\omega t} + \hat{a}^\dagger e^{i\omega t}\right)$$

where the atom-field coupling constant $\hbar g_{U,V} = \mu_{U,V}\sqrt{\frac{2\hbar\omega}{\varepsilon_0 L\pi w_0^2}}\cos(\mathbf{k}\cdot\mathbf{r}_0)$ is the Rabi frequency for the generic $U \longleftrightarrow V$ transition. The latter can be more conveniently written in terms of the spontaneous emission rate $\Gamma_{U,V} = 2\gamma_{U,V}$ and the wavelength λ of the $U \longleftrightarrow V$ transition:

$$g_{U,V} = \sqrt{\frac{3c\gamma_{U,V}\lambda^2}{\pi^2 L w_0^2}}\cos(\mathbf{k}\cdot\mathbf{r}_0) \tag{3.13}$$

The dependence on the polarisation and direction of the electric field with respect to the magnetic field is contained in the terms $\left(\vec{\epsilon}\cdot\mathbf{d}_{U,m_u}^{V,m_v}\right)$.

Please note that Eq. (3.12) is a generalisation of the Jaynes-Cummings Hamiltonian. Assuming now that the manifold V has a higher energy than U, and by performing the rotating-wave approximation, we obtain

$$\hat{H}_{U,m_u;V,m_v} = \hbar g_{U,V}\left(\vec{\epsilon}\cdot\mathbf{d}_{U,m_u}^{V,m_v}\right)\left(\hat{a}^\dagger\widehat{\sigma}_{U,m_u;V,m_v}e^{i\omega t} + \widehat{\sigma}_{V,m_v;U,m_u}\hat{a}e^{-i\omega t}\right) \tag{3.14}$$

Atom-laser electric dipole interaction

If $\hat{\mathbf{E}}$ represents a laser field, then the semi-classical approximation can be made, where the electric field is demoted from the operator status and becomes a (vectorial) complex-valued variable. It consists of replacing the electric field operator with its expectation value. Such an approximation is accurate because the photon number in the laser field is usually high enough that the absorption/emission of photons by/from the atom has virtually no effect on the laser field. Therefore, because an ideal laser outputs light in a coherent state with some amplitude α, the task is reduced to the calculation of $\langle\alpha|\hat{\mathbf{E}}|\alpha\rangle$:

$$\hat{\mathbf{E}}_{\text{laser}}(\mathbf{k},\mathbf{r},t) \rightarrow \mathbf{E}_{\text{laser}}(\mathbf{k},\mathbf{r},t) = \langle\alpha|\hat{\mathbf{E}}|\alpha\rangle = E_0\cos(\omega t - \mathbf{k}\cdot\mathbf{r})\vec{\epsilon} \tag{3.15}$$

with $E_0 = 2|\alpha|\sqrt{\frac{\hbar\omega}{2\varepsilon_0 V}}$.

The Hamiltonian for the electric dipole interaction for the $U \leftrightarrow V$ transition is therefore:

$$\hat{H}_{U,V} = -\hat{\mathbf{d}} \cdot \mathbf{E} = \sum_{m_u=-j_U}^{j_U} \sum_{m_v=m_u-1}^{m_u+1} \hat{H}_{U,m_u;V,m_v} \tag{3.16}$$

$$\hat{H}_{U,m_u;V,m_v} = \hbar\Omega_{U,V} \cos(\omega t - \mathbf{k}\cdot\mathbf{r}) \left(\vec{\epsilon}\cdot\mathbf{d}_{U,m_u}^{V,m_v}\right) \left(\widehat{\sigma}_{U,m_u;V,m_v} + \widehat{\sigma}_{V,m_v;U,m_u}\right)$$

where $\Omega_{U,V} = \mu_{U,V} E_0/\hbar$ is the Rabi frequency for the atom-laser coherent interaction for the transition $U \leftrightarrow V$. If the atomic motion can be neglected, i.e. $\delta r \ll \lambda$, we can set $\mathbf{r} = 0$. The counter-rotating terms can thus be eliminated by performing the rotating-wave approximation, and we finally obtain

$$\hat{H}_{U,m_u;V,m_v} = \frac{\hbar\Omega_{U,V}}{2} \left(\vec{\epsilon}\cdot\mathbf{d}_{U,m_u}^{V,m_v}\right) \left(\widehat{\sigma}_{U,m_u;V,m_v} e^{i\omega t} + \widehat{\sigma}_{V,m_v;U,m_u} e^{-i\omega t}\right)$$

3.2.3 Hamiltonian

The complete Hamiltonian for the eight-level atomic system coupled to two orthogonal cavity modes in the interaction picture is rather complex as it contains many terms. For the sake of simplicity, the total Hamiltonian $\hat{H}$ can be conveniently broken in three parts, pertaining the bare-ion Hamiltonian $\hat{H}_0$, the ion-laser interaction $\hat{H}_1$ and the ion-cavity interaction $\hat{H}_2$:

$$\hat{H} = \hat{H}_0 + \hat{H}_1 + \hat{H}_2 \tag{3.17}$$

Hamiltonian for the bare ion

The bare-ion Hamiltonian in the interaction picture can be readily decomposed in four operators:

$$\hat{H}_0 = \hat{H}_{0,S} + \hat{H}_{0,P} + \hat{H}_{0,D} + \hat{H}_{0,c} \tag{3.18a}$$

The first three operators on the right-hand side are the Hamiltonians for the S, P and D manifolds that implement the Zeeman shift of the respective sub-levels in a magnetic field of magnitude B:

$$\hat{H}_{0,S} = \sum_{m_s=-1/2}^{1/2} \hbar(\Delta_{\text{driv}} + m_s g_s \mu_B B)\widehat{\sigma}_{S,m_s;S,m_s} \tag{3.18b}$$

$$\hat{H}_{0,P} = \sum_{m_p=-1/2}^{1/2} \hbar(m_p g_p \mu_B B)\widehat{\sigma}_{P,m_p;P,m_p} \tag{3.18c}$$

$$\hat{H}_{0,D} = \sum_{m_d=-3/2}^{3/2} \hbar(\Delta_{\text{recyc}} + m_d g_d \mu_B B)\widehat{\sigma}_{D,m_d;D,m_d} \tag{3.18d}$$

The rightmost term of (3.18a) is the Hamilton operator for the uncoupled cavity field with two quantised modes, a and b:

$$\hat{H}_{0,c} = \hbar\left(\Delta_c - \Delta_{\text{recyc}}\right)\left(\hat{a}^\dagger\hat{a} + \hat{b}^\dagger\hat{b}\right) \tag{3.18e}$$

Here, as in chapter 2, Δ_{driv} and Δ_{recyc} are the detunings of the driving and recycling laser to the $S \leftrightarrow P$ and $D \leftrightarrow P$ transitions in the absence of a magnetic field. Similarly, the cavity is detuned by Δ_c from the $D \leftrightarrow P$ transition at $B = 0$.

Hamiltonian for the ion-laser interaction

The driving and recycling lasers act on the $S \leftrightarrow P$ and $D \leftrightarrow P$ transitions, respectively. The Hamiltonian for the ion-laser interaction is therefore decomposed into two parts:

$$\hat{H}_1 = \hat{H}_{1,SP} + \hat{H}_{1,DP} \tag{3.19a}$$

where the two operators expand fully to

$$\hat{H}_{1,SP} = \frac{\hbar\Omega_p}{2} \sum_{m_s=-\frac{1}{2}}^{\frac{1}{2}} \sum_{m_p=-\frac{1}{2}}^{\frac{1}{2}} \left[\left(\vec{\epsilon}_{\text{driv}} \cdot \mathbf{d}_{S,m_s}^{P,m_p} \right) \widehat{\sigma}_{P,m_p;S,m_s} + \text{h.c.} \right] \tag{3.19b}$$

$$\hat{H}_{1,DP} = \frac{\hbar\Omega_r}{2} \sum_{m_d=-\frac{3}{2}}^{\frac{3}{2}} \sum_{m_p=-\frac{1}{2}}^{\frac{1}{2}} \left[\left(\vec{\epsilon}_{\text{recyc}} \cdot \mathbf{d}_{D,m_d}^{P,m_p} \right) \widehat{\sigma}_{P,m_p;D,m_d} + \text{h.c.} \right] \tag{3.19c}$$

Hamiltonian for the ion-cavity interaction

For the ion-cavity interaction, two degenerate modes must be considered. They correspond to the two orthogonal photon polarisations supported by the cavity. Their respective annihilation operators are labelled $\hat{a}$ and $\hat{b}$.

$$\hat{H}_2 = \hat{H}_{2,a} + \hat{H}_{2,b} \tag{3.20a}$$

with

$$\hat{H}_{2,a} = \hbar g \sum_{m_d=-\frac{3}{2}}^{\frac{3}{2}} \sum_{m_p=-\frac{1}{2}}^{\frac{1}{2}} \left[\left(\vec{\epsilon}_a \cdot \mathbf{d}_{D,m_d}^{P,m_p} \right) \widehat{\sigma}_{P,m_p;D,m_d} \hat{a} + \text{h.c.} \right] \tag{3.20b}$$

$$\hat{H}_{2,b} = \hbar g \sum_{m_d=-\frac{3}{2}}^{\frac{3}{2}} \sum_{m_p=-\frac{1}{2}}^{\frac{1}{2}} \left[\left(\vec{\epsilon}_a \cdot \mathbf{d}_{D,m_d}^{P,m_p} \right) \widehat{\sigma}_{P,m_p;D,m_d} \hat{b} + \text{h.c.} \right] \tag{3.20c}$$

Here, the ion-cavity coupling strength g was assumed to be the same for both modes.

3.2.4 Dissipation

The full set of collapse operators corresponding to the different dissipative processes is obtained by performing the same extension of the formalism presented in chapter 2.

Atomic spontaneous emission

There are three possible decay channels for the photons that are spontaneously emitted from level P to S, as they can be σ^+, σ^- or π polarised. The corresponding collapse operators are given by

$$\hat{C}_{\gamma^{\pm},SP} = \sqrt{2\gamma_{SP} \left(\vec{\epsilon}_{\pm} \cdot \mathbf{d}_{S,\mp 1/2}^{P,\pm 1/2} \right)} \widehat{\sigma}_{S,\mp\frac{1}{2};P,\pm\frac{1}{2}} \tag{3.21}$$

$$\hat{C}_{\gamma^{0},SP} = \sum_{m=-1/2}^{1/2} \sqrt{2\gamma_{SP} \left(\vec{\epsilon}_{0} \cdot \mathbf{d}_{S,m}^{P,m} \right)} \widehat{\sigma}_{S,m;P,m} \tag{3.22}$$

Similarly to the previous case, the collapse operators for the spontaneous emission from P to D are given by:

$$\hat{C}_{\gamma^{\pm},DP} = \sum_{m=-1/2}^{1/2} \sqrt{2\gamma_{DP}\left(\vec{\epsilon}_{\pm}\cdot\mathbf{d}_{D,m\mp1}^{P,m}\right)}\,\hat{\sigma}_{D,m\mp1;P,m} \tag{3.23}$$

$$\hat{C}_{\gamma^{0},DP} = \sum_{m=-1/2}^{1/2} \sqrt{2\gamma_{DP}\left(\vec{\epsilon}_{0}\cdot\mathbf{d}_{D,m}^{P,m}\right)}\,\hat{\sigma}_{D,m;P,m} \tag{3.24}$$

Laser phase noise

In the experiment, both driving and recycling lasers have a non-zero linewidth (δ_{driv} and δ_{recyc} at half width at half maximum), which effectively introduces phase noise. This dephasing can be described by taking into account the following collapse operators:

$$\hat{C}_{\delta,\text{driv}} = \sum_{m_s=-1/2}^{1/2} \sqrt{2\delta_{\text{driv}}}\,\hat{\sigma}_{S,m_s;S,m_s} \tag{3.25}$$

$$\hat{C}_{\delta,\text{recyc}} = \sum_{m_d=-3/2}^{3/2} \sqrt{2\delta_{\text{recyc}}}\,\hat{\sigma}_{D,m_d;D,m_d} \tag{3.26}$$

Cavity decay

For the sake of completeness we list the collapse operators describing photon loss from either of the two cavity modes. Because they act only on the photon subspace, they retain their form from Chapter 2:

$$\hat{C}_a = \sqrt{2\varkappa}\,\hat{a} \tag{3.27}$$

$$\hat{C}_b = \sqrt{2\varkappa}\,\hat{b} \tag{3.28}$$

3.2.5 Observables

One-time expectation values

In the Schrödinger picture, the expectation value at time t for a certain observable represented by the operator $\hat{\mathcal{O}}$ is obtained by

$$\bar{\mathcal{O}}(t) = \langle\hat{\mathcal{O}}(t)\rangle = \text{Tr}[\hat{\mathcal{O}}\hat{\rho}(t)] \tag{3.29}$$

where $\hat{\rho}$ is the density operator, which is a solution of the master equation

$$\frac{d\hat{\rho}}{dt} = -\frac{i}{\hbar}\left[\hat{H},\hat{\rho}\right] + \mathscr{L}_{\text{diss}}(\hat{\rho}) = \mathscr{L}(\hat{\rho}) \tag{3.30}$$

The steady-state solution $\hat{\rho}_{ss}$ is a particular case that corresponds to the limit $t\to\infty$, being the solution of $d\hat{\rho}/dt = 0$.

$$\bar{\mathcal{O}}_{ss} = \lim_{t\to\infty}\text{Tr}[\hat{\mathcal{O}}\hat{\rho}(t)] = \text{Tr}[\hat{\mathcal{O}}\hat{\rho}_{ss}] \tag{3.31}$$

If the Hamiltonian is time independent, the evaluation of a certain observable at steady-state is reduced to an algebraic problem.

Correlation functions

The first and second order correlation functions of the field, $g^{(1)}(\tau)$ and $g^{(2)}(\tau)$, are given respectively by (see e.g. [46]):

$$g^{(1)}(t,t+\tau)=\frac{\langle\hat{E}^{+}(t)\hat{E}^{-}(t+\tau)\rangle}{\langle\hat{E}^{+}(t)\hat{E}^{-}(t)\rangle} \tag{3.32}$$

$$g^{(2)}(t,t+\tau)=\frac{\langle\hat{E}^{+}(t)\hat{E}^{+}(t+\tau)\hat{E}^{-}(t+\tau)\hat{E}^{-}(t)\rangle}{\langle\hat{E}^{+}(t+\tau)\hat{E}^{-}(t+\tau)\rangle\cdot\langle\hat{E}^{+}(t)\hat{E}^{-}(t)\rangle} \tag{3.33}$$

The first reveals information about the coherence properties of the field, while the second gives information about the photon stream statistics, like photon (anti-) bunching. From an abstract point of view, these correlation functions are the expectation values of products of operators evaluated at two different times.

By making use of the quantum regression theorem and taking the stationary limit, the intensity correlation function can be written as

$$\lim_{t\to\infty} g^{(2)}(t,t+\tau)=\frac{\mathrm{Tr}[\hat{a}^{\dagger}\hat{a}e^{\mathscr{L}\tau}(\hat{a}\hat{\rho}_{ss}\hat{a}^{\dagger})]}{n_{ss}^{2}}=:g^{(2)}(\tau) \tag{3.34}$$

where $n_{ss}=\mathrm{Tr}[\hat{a}^{\dagger}\hat{a}\hat{\rho}_{ss}]$ is the expectation value of the photon number at steady state. We can readily identify $\hat{a}\hat{\rho}_{ss}\hat{a}^{\dagger}/n_{ss}=:\hat{\rho}(0|\infty)$ as the density matrix describing the system at the instant a photon detection projected the system. By noting that $e^{\mathscr{L}\tau}\hat{\rho}(0|\infty)=\hat{\rho}(\tau|\infty)$, the expectation value can be written as

$$g^{(2)}(\tau)=\frac{\mathrm{Tr}[\hat{n}\hat{\rho}(\tau|\infty)]}{n_{ss}}=\frac{n(\tau|\infty)}{n_{ss}}=\frac{p(\tau|\infty)}{p(\infty)} \tag{3.35}$$

which is nothing more that the probability of detecting a photon a time τ after the first detection, normalised to the probability of detection one photon. In other words, the $g^{(2)}(\tau)$ can be understood as a conditional probability.

Regarding the first-order correlation function, a similar argumentation follows, it is sufficient to state that

$$\lim_{t\to\infty} g^{(1)}(t,t+\tau)=\frac{\mathrm{Tr}[\hat{a}e^{\mathscr{L}\tau}(\hat{\rho}_{ss}\hat{a}^{\dagger})]}{n_{ss}}=:g^{(1)}(\tau) \tag{3.36}$$

The emission spectrum $S(\omega)$ of the light source can be obtained applying the Fourier transformation to the field correlation function (see e.g. [36]):

$$S(\omega)=\frac{1}{2\pi}\int_{-\infty}^{+\infty} g^{(1)}(\tau)e^{i\omega\tau}d\tau \tag{3.37}$$

which can then be used to calculate the linewidth.

3.2.6 Numerical simulation

For small intracavity photon numbers, the photon space can be represented by a truncated Fock state basis. As the number of atomic levels is discrete, the state of the system can be represented by a density matrix of finite dimensions, which can be simulated on an ordinary computer with appropriate computational space.

The system was simulated by making heavy usage of the numerical routines by Sze Tan, packaged as the *Quantum Optics Toolbox* [56], for use with the Matlab numerical programming environment. The package introduces abstractions that simplify the implementation and the algebraic manipulation of operators and superoperators.

Chapter 4

Experimental tools

The experiments described in this thesis used single calcium ions stored in a linear Paul trap and coupled to an optical resonator, in a ultra-high vacuum environment. The state of the ion was manipulated by using lasers at various wavelengths and the emitted photon streams were observed. This chapter describes the various parts of the experimental apparatus.

First, the linear Paul trap is conceptually introduced as an evolution from the quadrupole mass filter. The dependence of the trapping potential on the electrode voltages is presented. Moreover, its implementation in the experiment is discussed. The optical cavity is then generically introduced and the special case of spherical resonators is considered. The components and assembly procedure of the realised optical cavity are described, together with the characterisation of the final system. The remaining components, namely the vacuum system, the calcium oven and the various laser systems are described. Finally, the photon detection systems are described.

4.1 Linear Paul trap

In order to confine a single calcium ion to a small region in space, a linear Paul trap is used. From the combination of static and oscillating electric fields on the various electrodes of the Paul trap, a tri-dimensional trapping potential is created.

4.1.1 Concepts: trapping potential

A linear Paul trap [13] consists mainly of a quadrupole mass filter with added electrodes at a dc voltage in order to introduce confinement along the symmetry axis of the trap. The idealised quadrupole mass filter is composed of four parallel electrodes with a hyperbolic profile which are at distance r_0 from the symmetry centre (see Figure 4.1).

Experimentally, two diagonally opposing rods are held at ground potential while the other pair is at a potential $2U(t)$. The theoretical analysis is usually simpler if we consider the more symmetric (equivalent) situation where the electric potentials $U(t)$ and $-U(t)$ are applied to the two pairs of diagonally opposite rods, respectively. The potential at the centre of the mass filter is therefore:

$$\Phi(\mathbf{r},t) = \frac{x^2 - y^2}{2r_0^2} U(t) \tag{4.1}$$

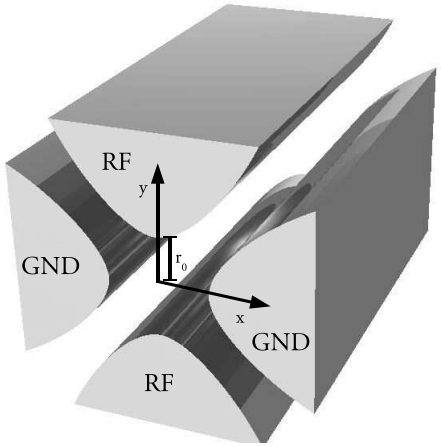

Figure 4.1: Quadrupole mass filter. Two of the four electrodes are connected to a radiofrequency field (RF), while the other two are grounded (GND).

If a static potential $U(t) = U_0$ is applied to the electrodes, the potential in Eq. (4.1) is saddle-shaped around the origin and does not confine charged particles. However, if the potential has a harmonic modulation at some frequency Ω (i.e. $U(t) = U_1 \cos \Omega t$), a radial confinement of charged particles becomes possible. The classical equations of motion for a particle of electric charge q and of mass m are given by the Lorentz force, $m\ddot{\mathbf{r}} = -q\vec{\nabla}\Phi$, which leads to a set of *Mathieu* equations [13, 57]

$$\frac{d^2x}{d\tau^2} - 2q_x \cos(2\tau)x = 0 \tag{4.2}$$

$$\frac{d^2y}{d\tau^2} + 2q_y \cos(2\tau)y = 0 \tag{4.3}$$

$$\frac{d^2z}{d\tau^2} = 0 \tag{4.4}$$

where the substitutions $\tau = \Omega t/2$ and $q_{x,y} = 2qU_1/(m r_0^2 \Omega^2)$ were performed.

The particle moves freely along the filter's axis (z axis). The motion within the xy plane can be determined exactly by solving the equations using the method by Floquet. Depending on the parameters $q_{x,y}$, the solutions can be either stable, with motion bounded by some radial confinement, or unstable (motion is unbounded). For $q_{x,y} \ll 1$, a simple solution for the x and y coordinates can be found:

$$x(t) \approx x_0 \left[1 + \frac{q_x}{2}\cos(\Omega t)\right] \cos(\omega_x t + \varphi_x) \tag{4.5}$$

$$y(t) \approx y_0 \left[1 - \frac{q_y}{2}\cos(\Omega t)\right] \cos(\omega_y t + \varphi_y) \tag{4.6}$$

where x_0 and y_0 are the amplitudes of the motion along the x and y axis, respectively. This solution allows the separation of the motion in two timescales, set by the *secular motion* and the *micromotion*. The secular motion is the usual oscillation around the

trap centre at the (trap) frequencies $\omega_{x,y} = \sqrt{\frac{2qU_1}{m^2\Omega^2 r_0^2}}$. The micromotion is a faster oscillation at the frequency Ω at which the mass filter is driven, atop of the secular motion.

The harmonicity of the secular motion in the xy plane can be understood as the result of the action of a *ponderomotive force*, which effectively creates a radial trapping potential. Recall that the electric field created by the trap oscillates at a high frequency Ω. If the inertia of the charged particle is sufficiently high, the particle hardly moves during one such oscillation. Over the course of time, in an hypothetical situation where the electric field is spatially homogeneous, the particle would simply remain around its initial position. However, if the electric field is spatially inhomogeneous (i.e. $\Phi(\mathbf{r}, t)$ has a spatial dependence), as in the case of the mass filter and the linear Paul trap, the particle drifts to the point where it experiences the minimum force. This drift results from a restoring ponderomotive force. Such force is proportional to the gradient of the intensity of the electric field and is independent of the sign of the charge:

$$\mathbf{F}_{\text{pond}} = -\frac{q^2}{m\Omega^2}\vec{\nabla}|\mathbf{E}(\mathbf{r})|^2 \tag{4.7}$$

where $\mathbf{E}(\mathbf{r})$ is the spatial component of the electric field, assumed to be in the form $\mathbf{E}(\mathbf{r}, t) = \mathbf{E}(\mathbf{r})\cos(\Omega t)$. The ponderomotive force can be cast into the form $\mathbf{F}_{\text{pond}}(\mathbf{r}) = -q\vec{\nabla}\Phi_{\text{pond}}$, where the *ponderomotive potential* Φ_{pond} for radial confinement can be recognised. Considering the case of the axially symmetric quadrupole mass filter, such potential is given by:

$$\Phi_{\text{pond}}(\mathbf{r}) = \frac{qU_1}{m\Omega^2 r_0^2}(x^2 + y^2) \equiv \frac{1}{2}m\omega_r^2 r^2 \tag{4.8}$$

which is a degenerate radial harmonic potential with the same oscillation frequency ω_r as the secular motion:

$$\omega_r = \omega_{x,y} = \sqrt{\frac{2qU_1}{m^2\Omega^2 r_0^2}} \tag{4.9}$$

The linear Paul trap differs from the quadrupole mass filter only by the addition of two end-cap electrodes along the z axis. If a static potential V is applied to both the end-caps, the motion along the z axis becomes bounded. By imposing Laplace's equation $\nabla^2\Phi = 0$ at the centre of the trap, and by observing that the total potential must depend on V, it has been shown (see e.g. [58]) that a new set of Mathieu equations can be obtained, which ultimately leads to the conclusion that the frequencies for the secular motion of the charged particle are modified to

$$\omega_r' = \omega_{x,y}' = \sqrt{\omega_r^2 - \frac{(\omega_z')^2}{2}} \tag{4.10}$$

$$\omega_z' = \sqrt{\frac{\alpha_{\text{geom}} qV}{2mL^2}} \tag{4.11}$$

where L is the distance between the two endcaps and α_{geom} is a numeric factor that depends on the particular geometry of the trap [59].

The reader is referred to previous work (e.g. [58, 60–62]) for further details.

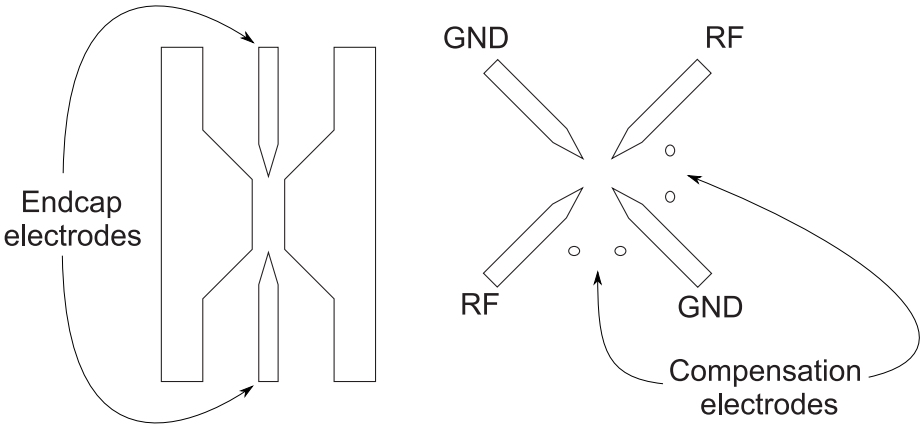

Figure 4.2: Trap electrodes: a) as seen from the side; b) as seen from top.

4.1.2 Implementation

The experiments described in this thesis used an engineered version of the linear Paul trap developed previously in Innsbruck and described in [62, 63].

The electrodes responsible for the radial potential are composed of four blades. Two tips were used as endcaps (see Figures 4.2, 4.3, 4.4). The gap between the tips was set to 4 mm. Two pairs of rigid wires were used as compensation electrodes. The trap electrodes were fabricated using an electro-erosion process on stainless steel which allowed a machining precision of 5 μm. The electrodes were mounted on two ceramic spacers (Macor®).

Additional holes were drilled on the larger ceramic spacer (Figure 4.3A) to allow the fixation of the whole mount to one flange of the vacuum chamber. The flange also accommodates six standard MHV (Miniature High Voltage) feedthroughs for the electrical connections of the various trap electrodes.

The air-side dc signals are connected to the respective feedthroughs in series with a resisto-capacitive low-pass filter at a cutoff frequency of 33 Hz. Under normal operation with a single ion, the trap tips are at a potential of 950 V, which is associated with an axial trap frequency of $\approx$ 1 MHz on calcium ions. The blade electrodes for the radial confinement are connected to a helical resonator, which is driven resonantly at 23.4 MHz. A quality factor $Q \approx 200$ was measured from the absorption spectrum of the loaded helical resonator. The radiofrequency source is a signal generator (Marconi Instruments 2023), which is typically amplified to about 5 W on a 50 Ω load. Under these conditions, the radial trap frequencies are non-degenerate, centred around $\approx$ 3 MHz, with a splitting of $\approx$ 61 kHz.

The compensation electrodes are used to reduce micromotion by introducing an extra static electric field. These were implemented by spot-welding stainless steel wires and inserting them into 1 mm drillings on the ceramic spacers. The electrodes are parallel to the trap axis. The plane defined by the first set of compensation electrodes (at a potential V_1) is perpendicular to the cavity axis (see following section). The second set (at a potential V_2) defines a plane parallel to the cavity axis and to the two large viewports.

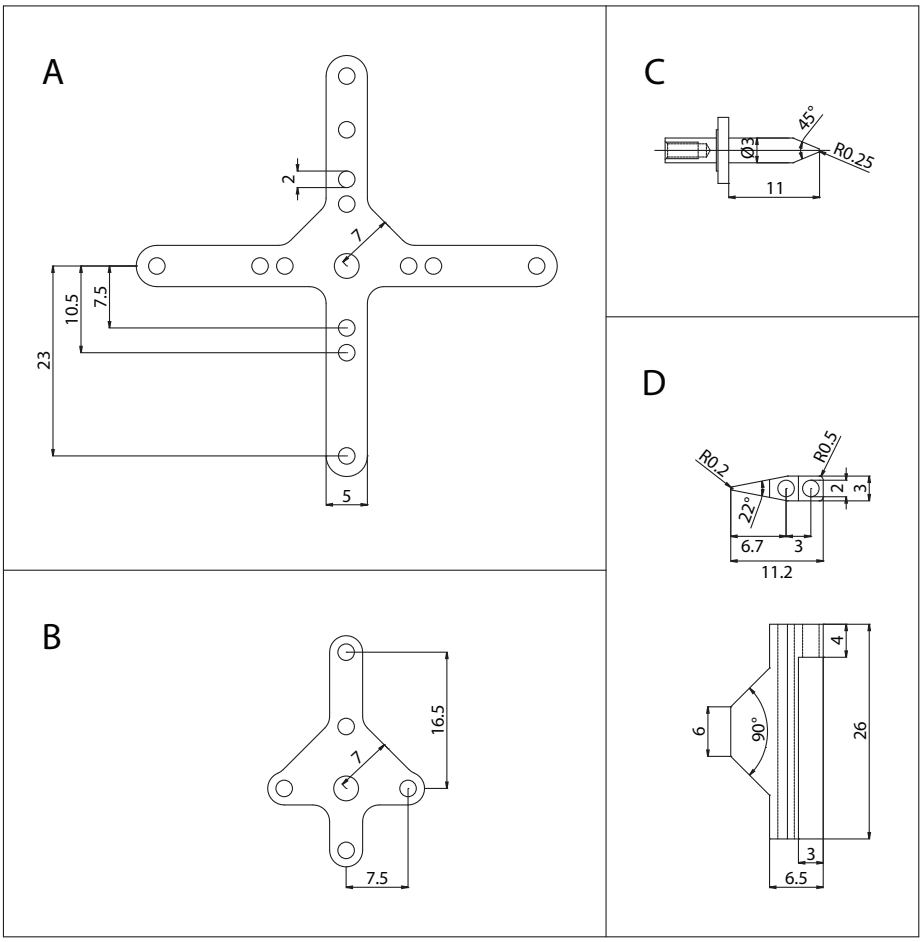

Figure 4.3: Relevant dimensions of the trap components, in millimetres: top ceramic holder (A), bottom ceramic holder (B), tip electrode (C), blade (D).

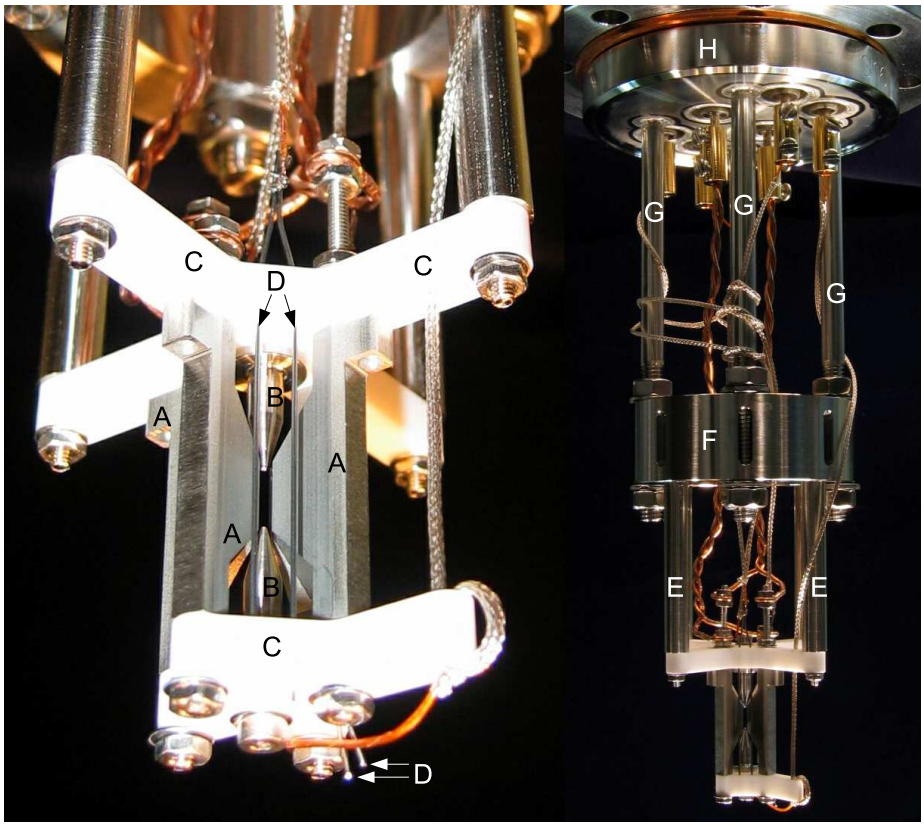

Figure 4.4: Photograph of the ion trap, taken before it was assembled in the vacuum chamber. The four blades (A) and tip electrodes (B) of the linear Paul trap are mounted on the two white Macor ceramic holders (C), together with the two sets of compensation electrodes (D). The trap is assembled to an intermediate holder (F) via four stainless steel rods (E). The intermediate holder (F) fits on four threaded rods (G) welded to the flange (H), which allowed for corrections on the tilt and total length of the structure during the assembly stage. The radiofrequency and ground electrodes are connected to the top flange feedthroughs by bare OFHC copper wire. Kapton-coated copper wire covered by a stainless steel braid is used for connecting the tips (B) and compensation electrodes (D) to the respective feedthroughs.

4.2 Optical cavity

4.2.1 Concepts

Photon storage in a resonator with flat mirrors

Two parallel flat mirrors facing each other can enforce the boundary conditions necessary to build an optical cavity. The mirrors are characterised by their field transmission, reflection and loss coefficients : t, r and l, respectively. It is also common to use the intensity transmission, reflection and loss coefficients : $\mathscr{T} = |t|^2$, $\mathscr{R} = |r|^2$ and $\mathscr{L} = |l|^2$, respectively. The loss mechanisms include photon absorption by the mirrors and light scattering to the outside world. Energy conservation ensures $\mathscr{T} + \mathscr{R} + \mathscr{L} = 1$ for each mirror.

If a plane wave of wavelength λ and intensity I_0 is perfectly coupled to the input of an optical resonator made of two identical flat mirrors placed at positions $x = \pm L/2$ parallel to each other, then the intensity of the field inside the resonator is given by (see e.g. [64, 65]):

$$I_{\text{cav}}(x) = I_0 \cdot \frac{\mathscr{T}}{(1-\mathscr{R})^2} \cdot \frac{1}{1+(\mathscr{F}/\pi)^2 \sin^2(kL)} \cdot \cos^2(kx) \tag{4.12}$$

where $k = 2\pi/\lambda$ is the wavenumber. The cavity field is characterised by a standing wave: intensity minima/maxima (*nodes/anti-nodes*) are spatially separated by $\lambda/2$. Also, $\mathscr{F}$ is the *finesse* of the resonator, which is a concept inherited from the theory of the Fabry-Perot interferometer. It is defined as the free spectral range of the optical resonator (ν_{FSR}) divided by the (full width at half maximum) bandwidth of its resonances ($\delta\omega$):

$$\mathscr{F} = \frac{\nu_{\text{FSR}}}{\delta\omega} \tag{4.13}$$

The *free spectral range* is defined as the frequency spacing between two successive longitudinal modes of the cavity. From (4.12), the resonance condition for the flat-mirror cavity is given by $kL = n\pi \Leftrightarrow L = n\lambda/2$, where n is an integer. The free spectral range is thus given by $\nu_{\text{FSR}} = c/(2L)$. In other words, $\mathscr{F}$ different lines can be resolved within one free spectral range.

The finesse is actually a measure of the quality of the mirrors, as it can be written in terms of the mirror reflectivity $\mathscr{R}$ (see e.g. [64, 66]):

$$\mathscr{F} \approx \frac{\pi\sqrt{\mathscr{R}}}{1-\mathscr{R}} \tag{4.14}$$

For very high reflectivities ($\mathscr{R} \to 1$), the finesse is proportional to the inverse of all photon losses:

$$\mathscr{F} \approx \frac{\pi}{\mathscr{T}+\mathscr{L}} \tag{4.15}$$

The cavity stores photons for a characteristic time $\tau_c = (\mathscr{F}/\pi)\cdot(L/c)$. The decay rate of the cavity electric field is therefore $\varkappa = (2\tau_c)^{-1}$.

In the limit of very small losses $\mathscr{L} \ll \mathscr{T} \ll \mathscr{R}$, on resonance and in an anti-node, $I_{\text{cav}} \approx I_0(\mathscr{F}/\pi)$. The enhancement factor $\mathscr{F}/\pi$ is the average number of reflections a photon undergoes before it is lost from the resonator. However, in the limit of high finesses $\mathscr{L}$ may be similar to $\mathscr{T}$ and even small losses must be taken into account. As an example, a cavity with a finesse of 70×10^3 with $\mathscr{L} = 0$ will have $I_{\text{cav}} \approx 22 \times 10^3 I_0$, whereas if $\mathscr{L} = 30$ ppm, then $I_{\text{cav}} \approx 7.4 \times 10^3 I_0$.

Spectrum of a spherical resonator

An optical cavity composed by two spherical concave mirrors with equal radii of curvature R and separated by a distance L exhibits a series of discrete resonances or *modes*, depending on the frequency of the light. The exact form of the mode structure depends on the symmetry present in the cavity (or its lack), though all modes must be solutions of the Helmholtz equation, typically taken in the paraxial approximation.

The results presented in this thesis were obtained using cavities whose beams exhibited rectangular symmetry. For this geometry, the solution for the Helmholtz equation is more easily obtained using Hermite-Gauss polynomials, for which the frequency spacing between the TEM_{kmn} modes [1] is given by [64]:

$$\omega_{k,m,n} = 2\pi \cdot \nu_{\mathrm{FSR}} \left[(k+1) + \frac{m+n+1}{\pi} \arccos(g_{\mathrm{st}}) \right] \tag{4.16}$$

Here k labels the *longitudinal modes* and m, n label the *transverse modes*, and *resonator stability parameter*

$$g_{\mathrm{st}} = 1 - L/R \tag{4.17}$$

Cavity parameters

The mode volume for a given mode TEM_{mn} is given in terms of the mode volume for the fundamental mode $V_0 = L\pi w_0^2/4$:

$$V_{mn} = V_0(m!n!2^{m+n}) \tag{4.18}$$

where w_0 is the waist of the fundamental mode:

$$w_0^2 = \frac{\lambda L}{2\pi} \sqrt{\frac{1+g_{\mathrm{st}}}{1-g_{\mathrm{st}}}} = \frac{\lambda}{2\pi} \sqrt{L(2R-L)} \tag{4.19}$$

For a fixed geometry, the mode volume of the longitudinal (TEM_{00}) mode is smaller than those of the higher-order transverse modes. It approaches zero as the beam waist w_0 decreases, which occurs if the cavity is in a near-planar ($L \to 0$) or in a near-concentric ($L \to 2R$) configuration (see Figure 4.6). Those two configurations are appealing for the CQED experiments, as the atom-cavity coupling g for a dipole transition increases with decreasing mode volume (see section 3.2.2):

$$g = \sqrt{\frac{\mu^2 \omega}{2\hbar\varepsilon_0 V}} = \sqrt{\frac{3c\gamma\lambda^2}{\pi^2 L w_0^2}} \tag{4.20}$$

where μ is the reduced dipole moment for the transition and 2γ is its spontaneous emission rate.

In the weak coupling regime (see section 2.1.4), the *cooperativity parameter* $C = g^2/(2\varkappa\gamma)$ is a relevant quantity, as it is related to the fraction $\beta = 2C/(2C+1)$ of spontaneous emission that occurs into the cavity mode. For the particular case of a two-level system, we have

$$C = \frac{3\lambda^2}{\pi^2} \cdot \frac{\mathscr{F}}{\pi w_0^2} = \frac{6\lambda}{\pi^2} \cdot \frac{\mathscr{F}}{\sqrt{L(2R-L)}} \qquad \text{(two-level system)} \tag{4.21}$$

[1] For further reference, TEM_{kmn} is often abbreviated as TEM_{mn}.

In this case and apart from the linear dependence on the wavelength of the transition, the cooperativity is basically determined by the properties of the resonator, namely the finesse $\mathscr{F}$ and the beam waist w_0.

Please note that for the case of a multi-level atom such as Ca^+, the excited state can decay to other states. The additional atomic spontaneous emission effectively reduces the cooperativity parameter

$$C_k = \frac{3\lambda^2}{\pi^2} \cdot \frac{\mathscr{F}}{\pi w_0^2} \cdot \frac{\gamma_k}{\sum_n \gamma_n} \qquad \text{(multi-level system)} \tag{4.22}$$

where k labels the transition under study, n labels the various decay channels and $2\gamma_n$ is the respective free-space spontaneous emission rate.

Resonator configuration and stability

The two mirrors act as a stable optical resonator only in the region $-1 < g_{st} < 1$, that is, $0 < L < 2R$. However, other than defining a limit, it is unclear from this condition on how stable the resonator is, in the sense that a small perturbation in the cavity configuration will still support a standing wave.

The cavity modes exist along the optical axis, which is determined by the line passing through the centres of curvature of both mirrors. These have a finite size, which effectively defines an aperture. Therefore, the relative position of centres of curvature is critical to allow the existence of an optical axis within both mirrors (see Figure 4.5).

The confocal configuration is the most stable case, where $g_{st} = 0$, that is $L = R$. Because the centre of curvature of one mirror lies in the surface of the other mirror, a small misalignment on the position or orientation of one mirror will often lead to a stable resonator. For a fixed set of mirrors with radius of curvature R, a cavity in confocal configuration displays maximum waist w_0. This is a particularly disadvantageous configuration for the experiments where the cooperativity constitutes the important quantity.

In contrast, the two extreme cases where $g_{st} \approx \pm 1$ are characterised by a sensitivity to misalignment, as depicted in Figure 4.5a,d.

- In the region close to the upper extreme, $g_{st} \lesssim 1$, the cavity length is much smaller than the radius of curvature of the mirrors: the resonator is in a *near-planar* configuration. Here, if the optical axis is tilted from the line defined by the centres of the surfaces of the two mirrors, the beam walks off to the rim of the mirrors after a sufficient number of reflections. Mirrors with a minimal curvature are usually employed to implement such a resonator [67, 68]

- In the region closer to the lower limit, $g_{st} \gtrsim -1$, the cavity length is slightly smaller than twice the radius of curvature of the mirrors: the mirrors of the cavity are therefore in a *near-concentric* configuration. Here, the distance between the two centres of curvature is small and a minor change in the position of one mirror can easily tilt the optical axis in such a way that the mode no longer fits entirely on the mirrors, possibly leading to dramatic diffraction losses.

In either of the cases $g_{st} \approx \pm 1$, the mode waist w_0 approaches the diffraction limit.

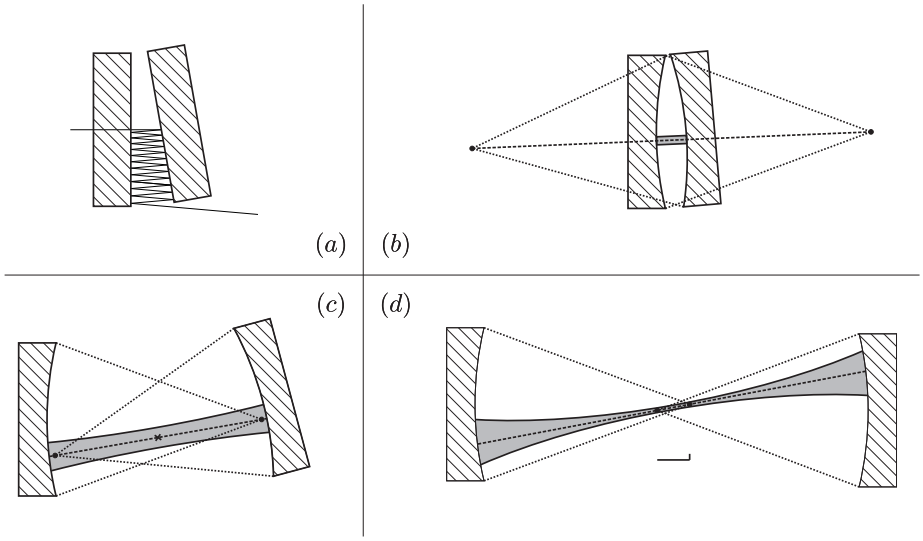

Figure 4.5: Sensitivity to misalignment of the various types of resonators. On a), a small tilt of one of the flat mirrors of Fabry-Perot interferometer is sufficient to misalign the resonator. This problem can be avoided by using curved mirrors in a near-planar configuration (b). A confocal cavity (c) is resilient even to an exaggerated perturbation of the tilt of one mirror. The optical axis of a near-concentric resonator (d) is very sensitive to small changes on the position of one of the two mirrors: the inset shows the displacement of the two mirror centres in the horizontal and vertical directions.

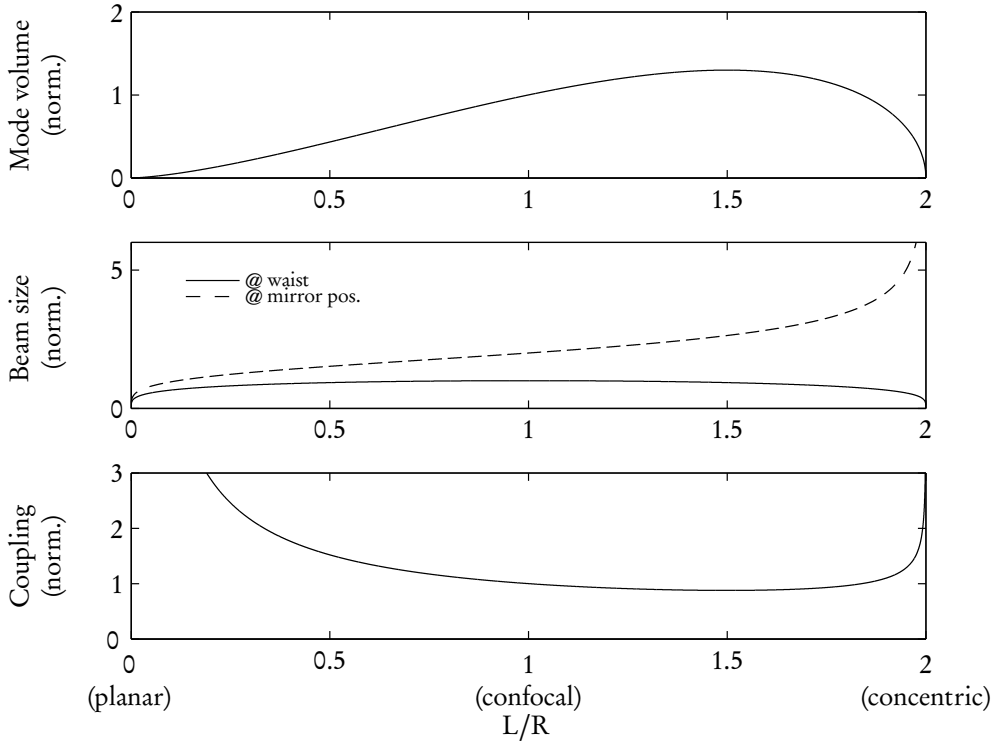

Figure 4.6: Comparison of several properties of a TEM_{00} mode in the whole stability region of a symmetric optical resonator. Top: Mode volume as a function of L/R normalised to the confocal case ($L = R$). The mode volume is maximum for $L/R = 3/2$, and approaches zero in the near-planar ($L \to 0$) and near-concentric ($L \to 2R$) configurations. Middle: beam radius at the waist (solid line) and mirror position (dashed line), normalised to the waist on the confocal case. The waist is minimum in both near-planar and near-concentric configurations, but the spot on the mirror increases as the near-concentric case is approached. Bottom: Atom-cavity coupling, normalised to the to coupling in the confocal case. The least favourable configuration corresponds to $L/R = 3/2$. From this point, the coupling increases smoothly towards the near-planar configuration and increases rapidly as the near-concentric case is approached.

4.2.2 Implementation

A near-concentric configuration for the cavity was sought, mainly due to the difficulty of fitting a macroscopic trap in the space inside a near-planar resonator.

Given the current state of technology and the equivalence between near-planar and near-concentric cavity configurations, it became clear that it would be simpler to build a near-concentric resonator with mirrors far away from the trap centre than it would be to build a microscopic trap resilient to the potential perturbations due to the mirror surfaces of a near-planar cavity. Additionally, the decision for a near-concentric configuration had the added bonus of a smaller cavity decay rate, which was of particular importance for the experiments discussed in this thesis.

There are two other important properties to consider.

The first is the spot size of the fundamental mode at the mirror surface, w_1, with:

$$w_1^2 = \frac{\lambda L}{\pi} \frac{1}{\sqrt{1 - g_{\mathrm{st}}^2}} = \frac{\lambda}{\pi} \frac{LR}{\sqrt{L(2R - L)}} \tag{4.23}$$

As can be observed in Figure 4.6, the spot size at the mirror surface increases dramatically as the near-concentric configuration is approached. Such systems are therefore prone to scattering losses: if the spot on the mirror surface exceeds the effective aperture defined by the mirrors, a portion of the light isn't reflected and the cavity presents excessive loss. This complication is potentially absent in near-planar cavities, as the mirror surface area largely exceeds the extension of the mode on the mirror surfaces.

The second parameter to consider is the Rayleigh length z_R, which sets the longitudinal length scale of the focal plane:

$$z_R = \frac{\pi w_0^2}{\lambda} = \frac{1}{2}\sqrt{L(2R - L)} \tag{4.24}$$

In the near-planar case, the Rayleigh length can be significantly larger than the cavity length ($z_R > L$), which implies that the beam radius of the cavity field is basically constant. The coupling of the ion to any particular anti-node is mainly irrelevant as the coupling strength does not significantly change. In contrast, the near-concentric case is characterised by $z_R < L$, which means that the strength of the ion-cavity coupling changes with the longitudinal position of the anti-node. Special care must be taken to allow the selection of the anti-node closest to the focal plane of the resonator by accurately positioning the ion in the cavity centre.

Assembly of the cavity mount

The cavity is composed of two mirrors with very high reflectivity, fabricated by REO[2]. Each mirror was specified to a different intensity transmission coefficient, in order to define a preferred output channel, resulting in an asymmetric cavity.

The two mirrors were first mounted on top of PZT stacks capable of a shear movement. Due to their minute dimensions, the mirrors could not be safely glued directly to the corresponding PZT stacks, which would allow to reduce the payload to an absolute minimum. Instead, each mirror had to be glued to a small and thin stainless steel frame, which was in turn glued to the top of the corresponding stack of piezoelectric actuators (see Figures 4.7 and 4.8).

[2]Research Electro Optics, Boulder, Colorado, USA

Figure 4.7: Components of the cavity mount: mirror frames (A), slow PZT stack (B), fast PZT stack (C), pillar for the slow PZT stack (D), pillar for the fast PZT stack (E) and frame (F).

The adhesive used to glue the different was dual-cure: a first exposure to UV light provided a superficial polymerisation of the adhesive, while a subsequent heat treatment completed the cure. The adhesive OP-66-LS by Dymax was chosen due to its suitability for ultra-high vacuum operation, high glass-transition temperature, ultra-low shrinkage ($< 0.1\%$) upon cure and low movement during temperature excursions. Such properties would minimise the misalignment upon the necessary bakeout procedure.

The *fast* and *slow* PZT stacks are composed of a different number of piezoelectric ceramic layers, two and six respectively, which can be driven by a maximum of ± 250 V. From our measurements in the final setup, we estimate that a variation of 400 V in the potential for the fast piezo moves the mirror by about 0.5 μm, while the same voltage variation at the slow piezo changes the cavity length by roughly 1.6 μm.

The bottom of each PZT stack was glued to auxiliary stainless steel pillars. The pillars could be mounted on a temporary translation stage and be individually manoeuvred in free space before being successively glued to a common frame.

The last step of the procedure revealed to be the most critical: as the second pillar was epoxied to the frame, the residual shrinkage of the adhesive would often randomly displace the position and tilt of the last mirror, leading to an unstable resonator. The cured adhesive could fortunately be easily scraped off and it was eventually possible to build a stable resonator with the desired length.

As depicted on the right hand side of Figure 4.8, and marked by the letters H and I, the cavity mount was installed on top of two crossed translation tables driven by PZT elements (Omicron MS5). When driven, the two translation tables allow fine tuning of the cavity position along the cavity axis and on the horizontally transverse direction with a specified precision of 20 nm. The vertical transverse direction can also be adjusted: the bottom translation table lies on top of a tripod table that can be tilted or moved along the trap axis direction by adjusting three differential micrometer screws (Elliot Scientific), in a similar fashion to [69]. This system allows the adjustment of the relative vertical position between the trap and cavity centres with a precision on the order of 1 μm.

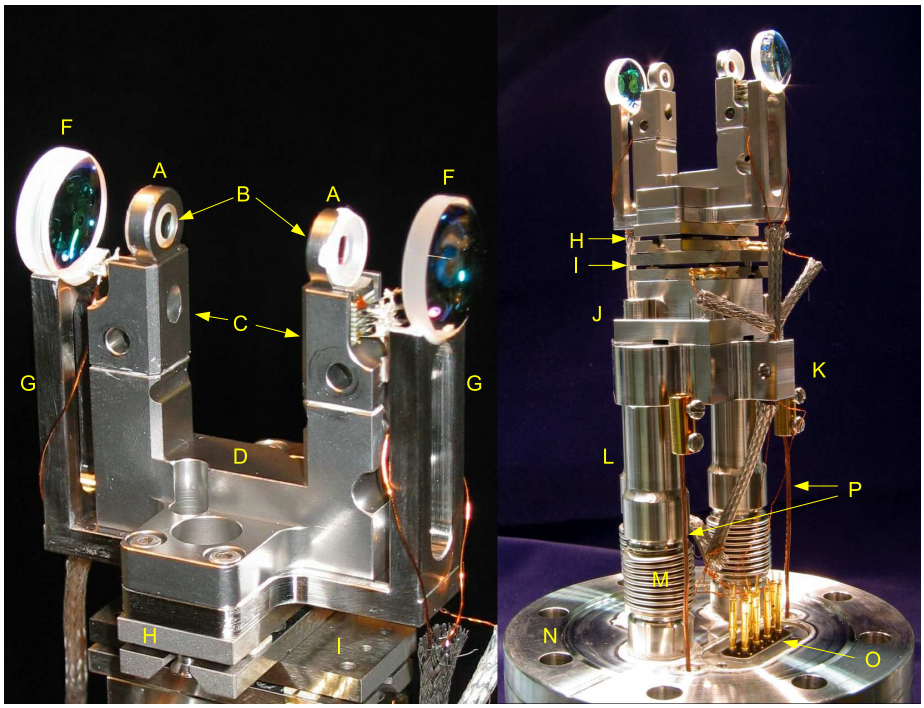

Figure 4.8: Photograph of the cavity mount (left) and of the cavity assembly (right). The connections between mirrors (B), their holders (A), the PZT stacks, the respective pillars (C) and the cavity mount (D) are glued using a dual-cure epoxy adhesive. The cavity mount (D) rests on top of a *U*-shaped structure (G) holding the two collimation lenses (F). The cavity mount is bolted to a series of two orthogonal piezo-driven translation stages (H and I). The bottom translation stage is secured to an intermediate fitting piece (J) which is then bolted to a tiltable table (K). The table is supported by three legs (L) welded to bellows (M) that are in turn welded to the CF63 flange (N). The sub-D feedthrough (P) and oven electrodes (P) are visible (the oven itself is not mounted).

reference mode				TEM_{00}	TEM_{00}
measured mode				TEM_{01}	TEM_{10}
mode spacing [70]		$\Delta\omega/(2\pi)$	(MHz)	311.0(1)	304.1(1)
cavity length		L	(mm)	19.9159(5)	19.9195(5)
beam waist	(866 nm)	w_0	(μm)	13.4(2)	13.2(2)
spot at mirror	(866 nm)	w_1	(μm)	291(4)	295(5)
atom-cavity coupling	(866 nm)	$g/(2\pi)$	(MHz)	1.61(2)	1.63(2)
beam waist	(854 nm)	w_0	(μm)	13.3(2)	13.1(2)
spot at mirror	(854 nm)	w_1	(μm)	289(4)	292(5)
atom-cavity coupling	(854 nm)	$g/(2\pi)$	(MHz)	1.54(2)	1.56(2)

Table 4.1: Cavity parameters at 854.209 nm and 866.210 nm, calculated from the measurements reported in [70]. The TEM_{01} and TEM_{10} modes are not degenerate, which is a situation not accounted for in Eq. 4.16, obtained for a cavity with perfect axial symmetry. The non-degeneracy is present in all transverse modes and is potentially attributed to an astigmatic deformation of the cavity.

4.2.3 Characterisation

Measurement of the frequency spacing of the cavity modes

By measuring the frequency spacing of two successive resonator modes and using Eq. 4.16, together with a rough estimate of the cavity length, it is possible to determine accurately the stability parameter g_{st}. Important cavity parameters can therefore be derived, such as the exact cavity length L, mode waist w_0 and atom-cavity coupling constant g. Two methods were used at different stages.

The first method was used throughout the assembly stage of the cavity mount, before the bake-out procedure. It consisted on coupling light at 785 nm to the resonator and scanning the cavity length in order to determine the frequency difference between the TEM_{00} and TEM_{01} modes. The sidebands created by frequency modulation at 16 MHz of the laser light were effectively used to calibrate the frequency scale. The cavity length could be measured with a precision of about 10 μm.

The second method was used after the bake-out procedure and is thoroughly described in Thomas Monz's diploma thesis [70]. The cavity length was first stabilised to a reference laser at 785 nm (see section 4.6). A laser at a wavelength of 854 nm was overlapped with the beam at 785 nm and its frequency was swept across a wide range. The transmitted light at 854 nm was separated and measured with a photodiode. The frequency spacing between the TEM_{00} and the TEM_{01}/TEM_{10} modes could therefore be directly retrieved, and the results are displayed on Table 4.1.

Measurement of the cavity decay rate

The cavity decay rate can be measured by a ring-down measurement. The light of a laser is coupled into the cavity and its frequency is slowly swept across the resonance of a certain TEM_{00} mode. Triggered upon a pre-determined cavity output level, I_0, the laser is rapidly switched off (on a timescale of a few ns). The light stored in the cavity decays exponentially in time. The associated time constant $\tau_c = (\mathcal{F}/\pi)\cdot(L/c)$ is the cavity storage time, which can be retrieved by fitting the experimental data to the model $I(t) = I_0 \exp(-t/\tau_c)$. Upon determination of the cavity length L, it is

then possible to determine the finesse of the resonator.

In the early stages of the experiment, the feasibility of near-concentric resonators was tested by measuring the finesse for different cavity lengths. Using this method, the finesse of a pair of mirrors was determined for different cavity lengths at a wavelength of 840 nm. The results are presented in Figure 4.9. Each point corresponds to a single attempt at a certain cavity length. Therefore, the results have no statistical meaning, but are useful nonetheless as they confirm the difficulty of obtaining stable near-concentric resonators. The mirrors were cleaned before the first data point was taken and were not cleaned in between. These particular experimental results show that in a near-confocal configuration ($L = 10$ mm) the cavity finesse was highest. For larger cavity lengths, the spot size at the mirrors increases, which increases the likelihood that the cavity beam hits a defect in the mirror surface, which will potentially scatter light. The loss is perceived as a decrease of the finesse. Therefore, the slow decrease of finesse for cavity lengths between 15 mm and 19 mm could be explained by the cavity beam hitting one such surface defect systematically. The irregular variation of the finesse for configurations closer to concentric ($L \gtrapprox 19$ mm) is unclear, but is partially attributed to the increased difficulty to align the optical axis to the line connecting the centre of the two mirror surfaces. Any small misalignments redefine the optical axis. Most likely, this will lead to increased diffraction losses, which effectively lowers the finesse. However, a different optical axis may also avoid a hitting a previous surface defect. It must be noted that each point represents only one attempt in a given configuration: the fact that the finesse variation is irregular only illustrates the practical difficulty of building a near-concentric resonator.

After installing the cavity in the vacuum chamber, the cavity finesse of the TEM_{00} modes was measured for three different wavelengths: 785, 854 and 866 nm, yielding $\mathscr{F}_{785} = 9.9(1) \times 10^3$, $\mathscr{F}_{854} = 7.7(1) \times 10^4$ and $\mathscr{F}_{866} = 7.0(1) \times 10^4$, respectively.

Measurement of absorption and scattering losses

In order to define an output channel, each mirror was specified to a different intensity transmission coefficient $\mathscr{T}_{1,2}$: the *input coupler* mirror was specified to $\mathscr{T}_1 = 4$ ppm, whereas the *output coupler* (the preferred output channel) was specified to $\mathscr{T}_2 = 40$ ppm. Under the ideal situation where the mirror losses would be negligible, the probability of a photon to escape to the output channel, provided one photon was put inside the resonator, would be $p_{\mathrm{out}} = \mathscr{T}_1/(\mathscr{T}_1 + \mathscr{T}_2) \approx 91\%$.

To determine the mirror properties, an approach similar to [71] was followed. The measurement of the finesse of the resonator, together with a careful measurement of the incident, transmitted and reflected intensities, when coupling light from either side of the cavity allows for the determination of the total internal losses $\mathscr{L} = \mathscr{L}_1 + \mathscr{L}_2$ and of the intensity transmission coefficients $\mathscr{T}_{1,2}$.

It is first convenient to note that the finesse of an asymmetric cavity can be rewritten as (see Eq. 4.15):

$$\mathscr{F} \approx \frac{2\pi}{\mathscr{T}_1 + \mathscr{T}_2 + \mathscr{L}} \tag{4.25}$$

Second, consider the realistic situation where only a portion ϵ of the incoming light spatially overlaps with the cavity mode and is actually coupled into the resonator. The fractions of the intensity that are reflected and transmitted when cou-

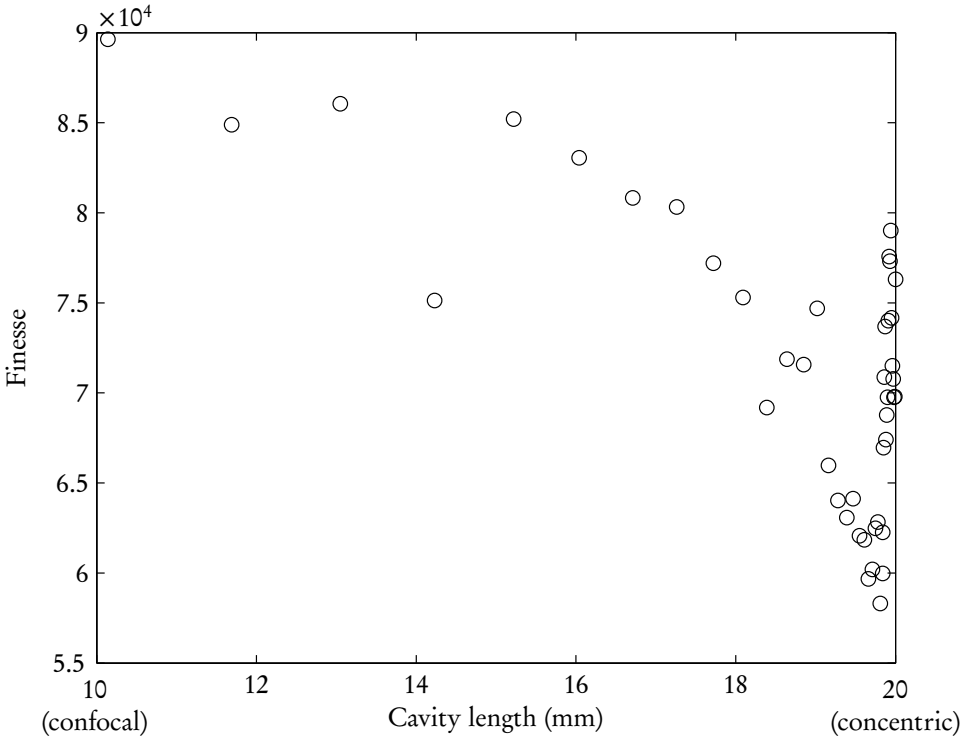

Figure 4.9: Finesse measurement for different cavity lengths at 840 nm. Each data point corresponds to a single trial. The finesse is maximum in near-confocal configurations and decreases slightly as the cavity configuration approaches the concentric case, due to the increase of the spot size at the mirror surface and corresponding higher probability of overlapping a surface defect. The irregular variation of the finesse is partially attributed to the increased difficulty on obtaining a stable resonator: the optical axis becomes tilted with respect to the line connecting the centre of the two mirror surfaces, leading to increasing diffraction losses.

pling resonant light to the input mirror are given by:

$$\left(\frac{I_t}{\epsilon I_0}\right)_{1\to 2} \approx \frac{4\mathscr{T}_1\mathscr{T}_2}{(\mathscr{T}_1+\mathscr{T}_2+\mathscr{L})^2} \tag{4.26}$$

$$\left(\frac{I_r-(1-\epsilon)I_0}{\epsilon I_0}\right)_{1\to 2} \approx \frac{(\mathscr{L}-\mathscr{T}_1+\mathscr{T}_2)^2}{(\mathscr{T}_1+\mathscr{T}_2+\mathscr{L})^2} \tag{4.27}$$

where I_r and I_t are respectively the reflected and transmitted intensities.

A series of careful measurements using each side of the cavity alternatively as input port was performed. A simple algebraic manipulation using Eqs. 4.25, 4.26 and 4.27 allows the independent determination of $\mathscr{T}_1$, $\mathscr{T}_2$ and $\mathscr{L}$. The results, which are summarised in Table 4.2.3, revealed to be quite different from the values specified by the manufacturer. As a consequence, we obtain $p_{\text{out}} = 19(2)\%$.

λ (nm)	Finesse $\mathscr{F}$	$\mathscr{T}_1$ (ppm)	$\mathscr{T}_2$ (ppm)	$\mathscr{L}$ (ppm)
854.210 (specified)	–	4	40	–
854.210 (measured)	$77(1)\times 10^3$	1.3(3)	13(1)	68(2)
866.215 (measured)	$70(1)\times 10^3$	1.9(4)	17(3)	71(3)

Table 4.2: Measurement of the properties of the trap cavity mirrors, for the two relevant wavelengths. Here, $\mathscr{L} = \mathscr{L}_1 + \mathscr{L}_2$ is the total loss in the cavity.

4.3 Vacuum apparatus

The setup composed by the trap and cavity assemblies was installed in a tight vessel which was then evacuated.

4.3.1 Components

The shape of the vacuum chamber can be loosely described as an octagonal prism with a horizontal axis (see Figure 4.10). Three of the facets house CF63 flanges, which were used to mount the trap, cavity and vacuum-pump assemblies. The remaining five facets display CF35 viewports. The two large CF200 flanges were used to attach recessed viewports with a diameter of 200 mm. The vacuum pump assembly is composed of a titanium sublimation pump, a 20 l/s ion getter pump (Varian VacIon Plus 20), a UHV gauge (Varian UHV-24) and a full-metal valve (VAT series 284), all of which were mounted on the different CF63 flanges of a six-way cross. The remaining flange was fitted with a viewport.

4.3.2 Bake-out

Using the metal valve, a turbomolecular pump was attached to the chamber. Under constant pumping, the vessel was first baked out at 280°C for a period of about one week, with all viewports replaced by blanks. Afterwards, in a second bake-out at 130°C that lasted two weeks, the blanks were quickly replaced by the respective viewports and both trap and cavity assemblies were installed. Special care was taken to prevent heating/cooling rates larger than 5°C/hour. Once the setup was removed from the oven, the trap cavity was measured to have a cavity length of 19.92 nm.

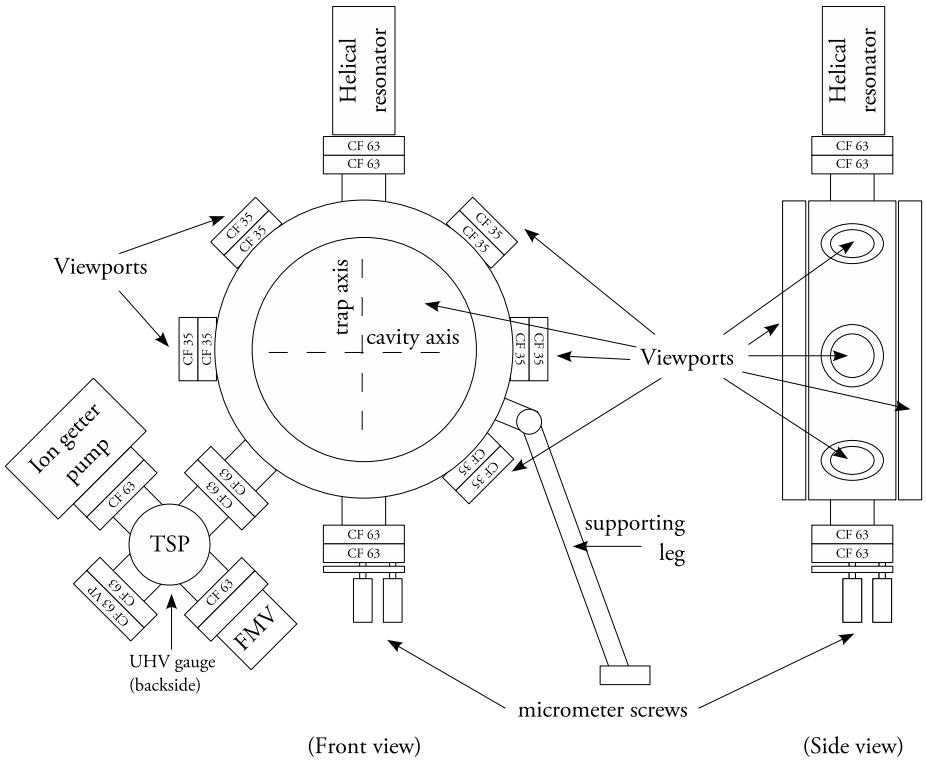

Figure 4.10: Schematic representation of the assembled vacuum vessel used to enclose the experimental apparatus.

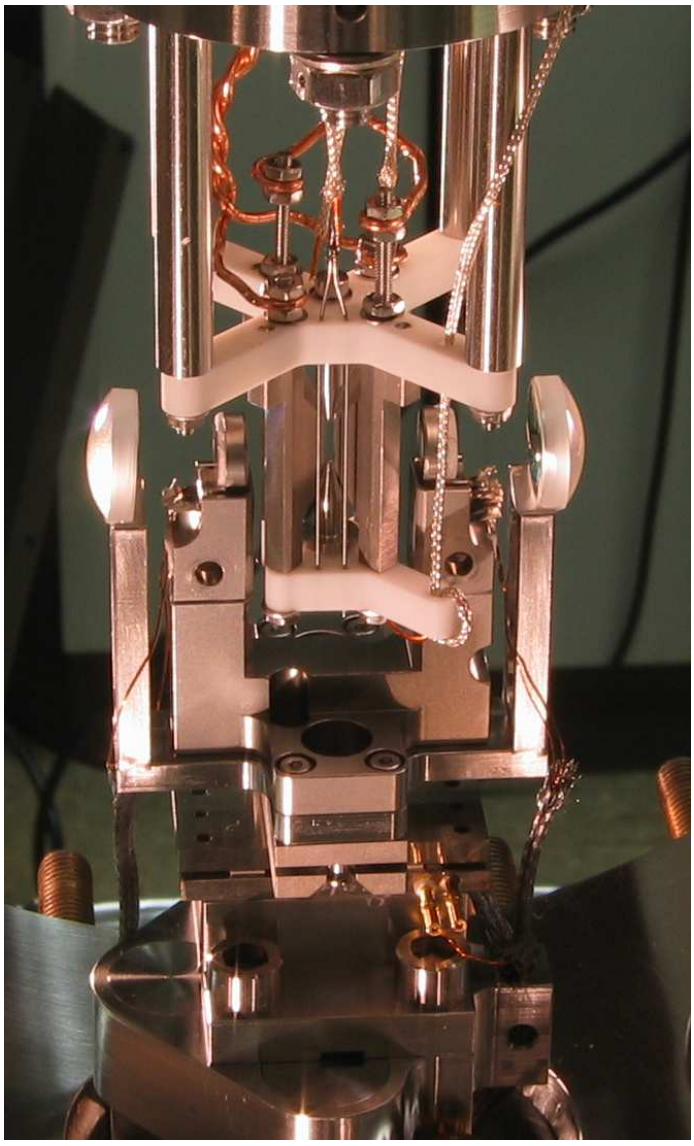

Figure 4.11: Photograph of the assembled trap-cavity system before bakeout.

Achieving a stable resonator with a sufficiently high finesse required several attempts: during bake-out, the cavity may suffer from contamination and/or misalignment.

The atmosphere in the vessel is typically kept at a pressure of 3×10^{-11} mbar, being maintained only by the ion getter pump and an occasional firing of the titanium sublimation pump.

4.4 Calcium oven

Calcium is delivered to the trap in the form of an atomic vapour. Combined with the trap potential, a two-step photo-ionisation process removes one electron from the outer shell (see section 4.5).

At pressures on the order of 10^{-11} mbar and at temperatures exceeding 500 K, atomic calcium sublimates at a sufficiently high rate to ensure rapid loading rates. The necessary heat is provided by the dissipation of a continuous current of ≈ 4.5 A flowing through an oven containing atomic calcium in the form of fine grains.

The oven is sketched in Figure 4.12. The oven consists of a ≈ 5 cm long stainless steel tube, whose ends are flattened and spot-welded to two stainless steel electrodes, that was later fitted in the cavity assembly, between the holders for the collimation lenses and the cavity mount (see Figure 4.8). The only opening in the oven is a 1 mm diameter hole drilled in middle aimed at the cavity mount. The atomic

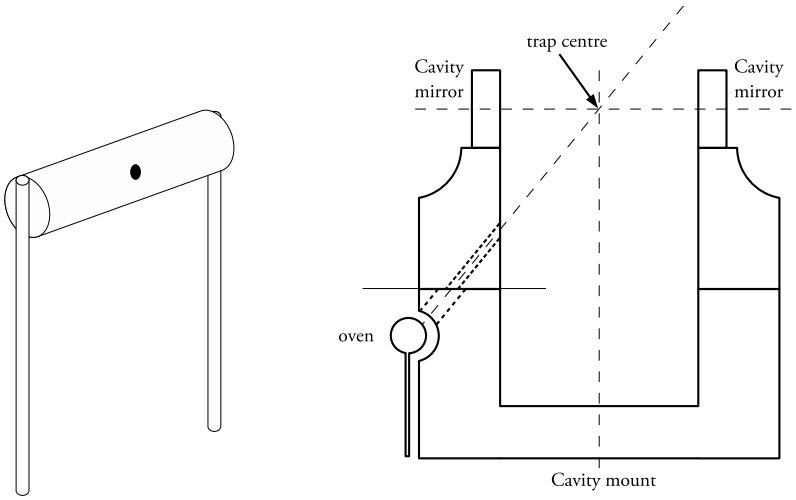

(a) Calcium oven (b) Mounting scheme for the oven

Figure 4.12: Sketch of the calcium oven and its mount. The oven is composed of a stainless steel tube with 1 mm diameter hole drilled in middle. The tube is filled with granulated calcium and two thin stainless steel rods are spot-welded to both ends. The oven is heated up by connecting the two rods to a power supply and the vaporised calcium escapes through the hole in the oven. The oven in mounted such that the atomic beam traverses an aperture made in the cavity mount (composed of two drillings), which spatially filters the atomic beam and prevents excessive contamination of the cavity mirrors.

calcium vapour beam traverses an aperture made in the cavity mount, which acts effectively as a spatial filter/collimator. The resulting atomic beam moves ballistically through the trapping region, where it can be ionised. Upon trapping of one ion, the power supply providing the current to the oven is switched off.

However, it turned out that the mount of the oven is not sufficiently stable. This is a design flaw that was only detected while experimenting. Depending on the exact position of the cavity mount, a thermal contact between the oven and the cavity mount may exist or not. Unfortunately, it is not possible to load ions when the cavity is in its optimal position, i.e. when the cavity waist matches the ion position. In this configuration, the added dissipation from the thermal contact prevents the oven from heating to sufficiently high temperatures. Nevertheless, the problem is easily circumvented by moving the cavity mount prior to loading, by driving one of the PZT-driven translation stages, and moving back to the original position afterwards.

4.5 Laser systems

In this section, we describe the various lasers sources required for the operation of the experiments described in this thesis. The current laser system is a result of the permanently on-going collective work of the research group and can be understood as an evolution of the historical systems previously described in [39, 61–63, 69, 70, 72–77]

Laser at 397 nm

The light at 397 nm acts on $S_{1/2} \leftrightarrow P_{1/2}$ dipole transition and is used for Doppler-cooling, state preparation, state detection and pumping of the vacuum-stimulated Raman transition on the $S_{1/2} \leftrightarrow D_{3/2}$ transition. A schematic representation of the setup for the laser at 397 nm is given in Figure 4.13.

The light at 397 nm is obtained by frequency doubling a 794 nm Ti:Sapphire (Ti:Sa) laser (Coherent, CR–899-21), which is in turn pumped by a solid-state laser (Coherent, Verdi V10). The frequency of the laser at 794 nm is locked using the Pound–Drever–Hall method (PDH) [78]. A temperature stabilised cavity serves as a passive frequency reference, which is effectively used to derive an error signal. The frequency is corrected by feeding back to a PZT element that acts on the length of the lasing cavity. The linewidth of this laser has been estimated from excitation spectra to be around 200 kHz. The frequency-doubling stage is based on a commercial LBO doubler crystal (Spectra Physics LAS, 'Wavetrain').

In typical operation conditions, the Ti:Sa laser is pumped with ≈ 7 W of light at 532 nm, yielding 500 mW at 794 nm. After the frequency doubling stage, ≈ 50 mW of ultra-violet light at 397 nm is available. This light is then split between the different experiments running in the laboratory. For the particular case of the CQED experiment, two acousto-optical modulators (AOM) running at a central frequency of 80 MHz are set up in double-pass configuration and coupled to two different polarisation-maintaining single-mode fibres, which guide the light to the experimental table.

The first AOM shifts the frequency of the laser light by $\approx +160$ MHz. Once on the experiment table, this light can be switched by using another AOM operating at 80 MHz in single-pass configuration. This light is then sent to the ion and constitutes the "397" beam, as it is near-resonant to the ion.

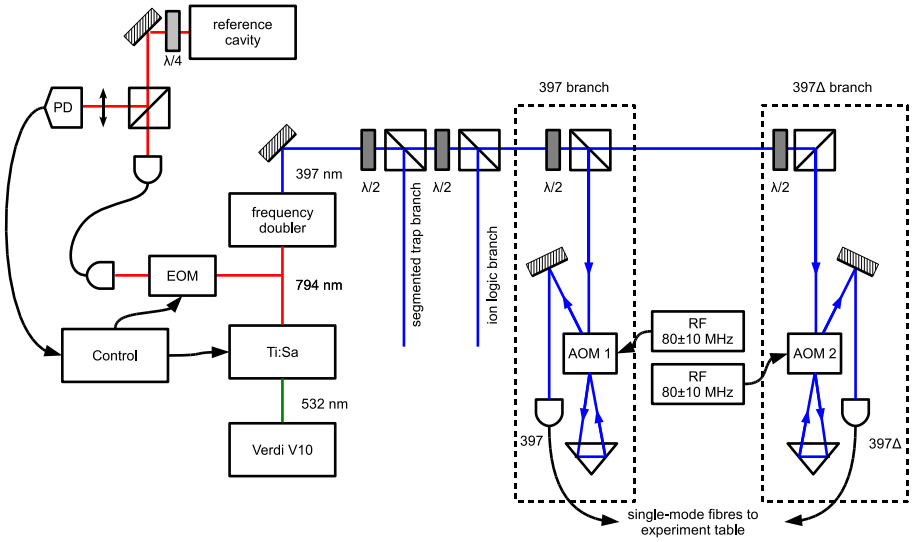

Figure 4.13: Schematic setup for the 397 nm laser. The laser light at 532 nm from a diode-pumped solid state laser (Verdi V10) is used to pump a Ti:Sa ring laser(Coherent 899). The light at 794 nm in then frequency doubled and divided into several branches. On one of the branches, the frequency of the light is up-shifted by 160 MHz, whereas in another branch the frequency of the light is down-shifted by 320 MHz. The light of these beams is coupled to separate single-mode fibres going to the experimental table.

The second AOM on the laser table shifts the frequency of the laser light by ≈ -160 MHz. The resulting beam ("397Δ") is used to drive the vacuum-stimulated Raman transition together with the trap cavity. The detuning of this beam relative to the $S_{1/2} \leftrightarrow P_{1/2}$ transition is therefore $\Delta \approx -400$ MHz.

In earlier stages of the experiments, both AOMs were mounted in single pass, but were also operating at 80 MHz. The two beams differed in frequency by ≈ 160 MHz, had orthogonal polarisations and were coupled to the same single-mode fibre. The detuning used for the initial measurements exploiting the vacuum-stimulated Raman transitions was therefore $\Delta = -160$ MHz.

Ultrastable laser at 729 nm

The narrow quadrupole transition at $S_{1/2} \leftrightarrow D_{5/2}$ at 729 nm is driven by the light produced by a very narrow band Ti:Sapphire laser (Coherent CR–899-21), which is also pumped by a solid-state laser (Coherent, Verdi V10). Akin to the 794 nm laser, the frequency of the Ti:Sa laser at 729 nm is stabilised using a PDH–locking scheme. Its short-term (≈ 1 s) linewidth, however, is of only about 1 Hz. The cutting-edge stability [77] is achieved by locking to an evacuated and temperature stabilised (sub-μK) high-finesse cavity ($\mathscr{F} \approx 4 \times 10^5$) and by feeding back to not only the laser cavity PZT element, but also to an intra-cavity electro-optical modulator (EOM).

With a pump of ≈ 7 W at 532 nm, the typical light power at the Ti:Sa output is of 700 mW. The light is transported to the experiment table via a single-mode fibre, and its frequency is up-shifted by an acousto-optical modulator running at a

central frequency of 250 MHz and mounted in a double-pass configuration. The ion is typically illuminated with a power of ≈ 25 mW.

Diode lasers at 866 nm and 854 nm

Two commercial diode lasers at 866 nm and 854 nm (Toptica, DL-100) are used to repump the population of the $D_{3/2}$ and the $D_{5/2}$ states. Figure 4.14 shows a schematic representation of the laser system at 866 nm; the laser system at 854 nm follows a similar design.

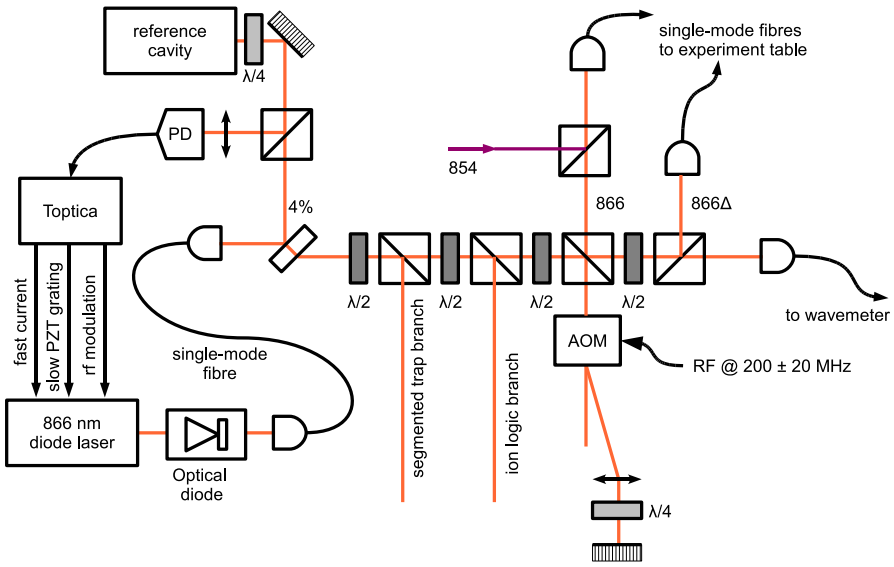

Figure 4.14: Schematic setup for the 866 nm laser. The setup for the 854 nm laser follows a similar scheme. The laser light from a Toptica DL100 diode laser running at 866 nm passes by an optical diode and is coupled to a single-mode fibre. The output of the fibre is divided amongst six branches. One branch is used for frequency stabilisation of the laser using the PDH scheme, while another is used for absolute frequency measurement in a wavemeter. The remaining four branches are allocated to the various experiments running in the laboratory. The experiments described in this thesis made use of two such branches: a resonant beam (866) and a beam detuned by −400 MHz from the resonance (866Δ). The light of these beams is coupled to separate single-mode fibres going to the experimental table.

The diode laser is grating stabilised using the Littrow configuration. The light at its output is collimated, sent through an optical diode and coupled to a single-mode fibre.

The light at the output of the fibre is then divided in six branches. The first branch comprises a small portion of the light and is used for frequency stabilisation. The Pound–Drever–Hall method was use to lock the frequency to temperature-stabilised cavities having a finesse of around $\mathcal{F} \approx 10^3$. The resulting laser linewidth

is ≈ 100 kHz.

The light in another branch is sent to a wavemeter, which monitors the absolute frequency of the laser. The four remaining branches are taken by the different experiments: the setups focused on segmented trap technology and ion logic use one branch each, while CQED uses two branches.

One of CQED's branches (marked 866Δ in Figure 4.14) is approximately detuned by -400 MHz from the $P_{1/2} \leftrightarrow D_{3/2}$ transition and is used as a frequency marker to help with the transfer lock (see section 4.6). The light in the second CQED branch (marked 866 in Figure 4.14) is near-resonant with the $P_{1/2} \leftrightarrow D_{3/2}$ transition and can be frequency shifted using an acousto-optical modulator running at a central frequency of 200 MHz, set in double-pass configuration, which allows both frequency and amplitude tunability, as well as adequate switching (attenuation of ≈ 40 dB). In both branches, the light is coupled into single-mode fibres and sent to the experimental table. About 1 mW of light power is sufficient at the trap apparatus.

Photo-ionisation lasers at 423 nm and 375 nm

The photo-ionisation of atomic calcium is a two-step process [79]. First, a laser at 423 nm excites atomic calcium to the $4p^1P_1$ state. From this level a second laser at 375 nm ionises the atom.

Both light sources are commercial diode laser systems (Toptica DL-100) that are grating stabilised by the Littrow technique. The fine tuning of the more critical 423 nm laser frequency is achieved by driving a PZT element which mechanically acts on the position of the grating. The wavelength of this laser can be coarsely checked using a hollow cathode calcium discharge lamp. The transition is collision-broadened to about 1 GHz. More accurate results have been obtained using Doppler-free saturation spectroscopy on a calcium vapour cell [75].

Frequency calibration

All wavelengths were initially measured with custom-built wavemeters with a relative precision of $\approx 10^{-7}$ [80]. The wavemeters worked by comparing the unknown wavelength with a reference wavelength of a He-Ne laser. This wavemeter was later replaced by a commercial unit (HighFinesse WS7) with a relative accuracy of $\approx 10^{-7}$ (i.e. 60 MHz absolute accuracy). The wavemeter precision is sufficient to determine the correct TEM_{00} mode of the reference cavities. The ultimate frequency reference is obviously the ion, which is spectroscopically probed for all relevant wavelengths.

Intensity stabilisation

The stability of the intensity of the laser beams labelled 397Δ and 866 (see Figures 4.13 and 4.14) is of critical importance for most of the experiments. For this purpose, the intensity of these beams is constantly measured with a fast low-noise photodiode. For each beam, a proportional-integral filter loop is then used to act on the radiofrequency power feeding the corresponding AOM on the respective laser tables. For further details, the reader is referred to [81].

4.6 Transfer lock

4.6.1 Motivation

If the driving laser at 397 nm and the trap cavity are detuned by the same amount from the $P_{1/2}$ state, it is possible to excite a Raman transition between the states $S_{1/2}$ and $D_{3/2}$. For vanishing Rabi frequencies of the driving laser, the linewidth of the Raman transition reaches a minimum linewidth equal to the cavity decay rate ($2\varkappa$ at FWHM).

In other words, the cavity detuning Δ_c is defined to an uncertainty set by the cavity linewidth. The cavity length uncertainty δL must therefore be defined to within $\delta L = \lambda/(2\mathscr{F})$, otherwise the uncertainty on the detuning is broadened. For a cavity length of $L = 19.92$ mm and a finesse of $\mathscr{F} = 7 \times 10^4$ at $\lambda = 866$ nm, this amounts to $\delta L \approx 6$ pm, which is merely six times the radius of the hydrogen atom. With such small numbers, keeping the trap cavity detuning stable becomes a serious technical difficulty. The approach we follow makes use of a transfer lock technique, where a stable laser is used as a length reference for a servo loop acting on the fast PZT stack, thus controlling the cavity length.

The current setup follows closely the setup presented in [69]. A diode laser operating at 785 nm is locked to an ultra-stable reference cavity. In turn, the trap cavity is locked to the 785 nm laser light. This wavelength is far-detuned from any relevant optical transition in $^{40}Ca^{+}$ and therefore does not interfere with the dynamics of the system (apart from a minimal light shift [39]). By tuning the frequency of the laser at 785 nm, the detuning of the cavity around the ion trap can be swept.

4.6.2 Laser system at 785 nm

Diode laser

A commercial grating-stabilised diode laser (Toptica DL-100) operating at 785 nm is frequency locked to an ultrastable reference cavity using the method by Pound, Drever and Hall [78]. A schematic representation of the setup for the 785 nm laser is given in Figure 4.15. The output of the laser is distributed between the locking and experimental branches.

In the locking branch, an error signal is derived. An electro-optical modulator is used to modulate the frequency of the light coupled to the ultra-stable reference cavity. The reflected light is measured by a photodiode with 100 MHz bandwidth. The error signal is derived by mixing the signal from the photodiode with the radiofrequency used for frequency modulation. The error signal is then actively filtered by two stages of Proportional-Integrator controllers (PI) attached in series. The first stage is used to modulate the injection current of the diode laser while the second stage acts on the PZT controlling the position of the grating.

In the experimental branch, the light is frequency shifted by an acousto-optical modulator (Brimrose TEF-270-100) running at a central frequency of 270 MHz set up in double-pass configuration, which allows fine tuning of the laser frequency within a range of ≈ 200 MHz. The resulting light is sent through an electro-optical modulator driven at a frequency of ≈ 16 MHz. The frequency-modulated light is then coupled to a single-mode fibre and is sent to the experiment table, where it is effectively used as a frequency reference for locking the detuning of the trap cavity.

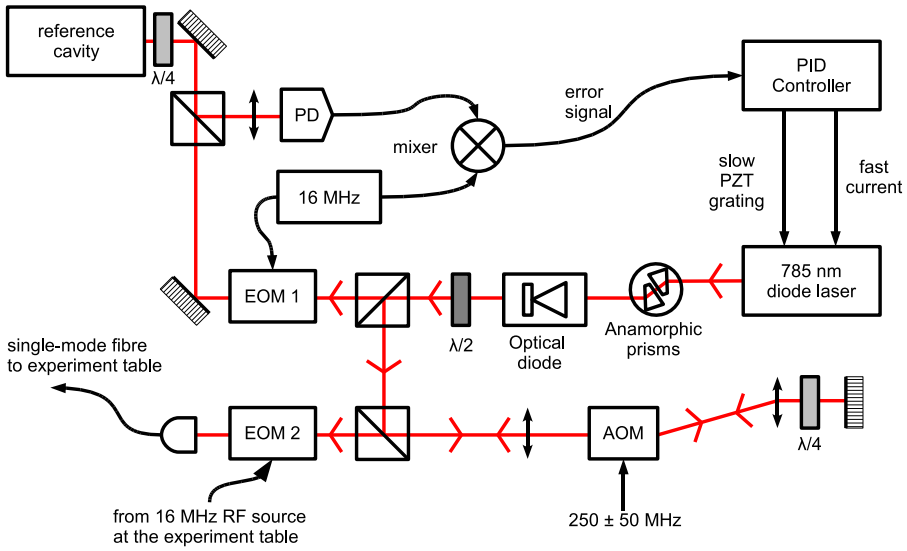

Figure 4.15: Schematic setup for the 785 nm laser. The light output by the diode laser at 785 nm is frequency-stabilised using a reference cavity and the Pound-Drever-Hall technique. The fine-tuning of the laser frequency and switching are obtained by using an acousto-optical modulator set up in double-pass configuration.

From the residual error signal, the linewidth of the 785 nm laser is estimated to be ≈ 5 kHz.

Ultra-stable reference cavity

The reference cavity currently used for the 785 nm laser was originally built for the laser system at 729 nm, and is described in [73]. The cavity mirrors are rigidly glued to an ovoid hollow spacer with a length of 15 cm, made of a special glass with a low thermal-expansion coefficient (ULE) (see [73], page 55). This cavity mount lies on top of silicon o-rings inside an evacuated chamber ($\approx 10^{-8}$ mbar). The vacuum vessel rests on a ≈ 5 mm thick rubber board on top of an optical table. The vessel is covered with heating resistors and is equipped with temperature sensors. An external electronic PI regulator injects the necessary current to keep the temperature stabilised slightly above room temperature. To improve the temperature stability, an aluminium box covered with expanded polystyrene boards was built around the vacuum vessel and was loosely filled with a thermal insulating cloth. The box is also equipped with temperature sensors and heating resistors, and can therefore be temperature stabilised, though that has not yet been deemed necessary.

The finesse of the cavity has been measured to be $\mathscr{F} \approx 2000$ at 785 nm. With a free-spectral range of $\nu_{\mathrm{FSR}} \approx 1$ GHz, its linewidth is $\delta\nu \approx 500$ kHz.

4.6.3 Trap cavity lock at 785 nm

The frequency-modulated laser light at 785 nm is coupled to the trap cavity (Figures 4.15 and 4.16). The reflected light is used to derive an error signal that is used to servo the fast PZT of the trap cavity, via a PI filter loop.

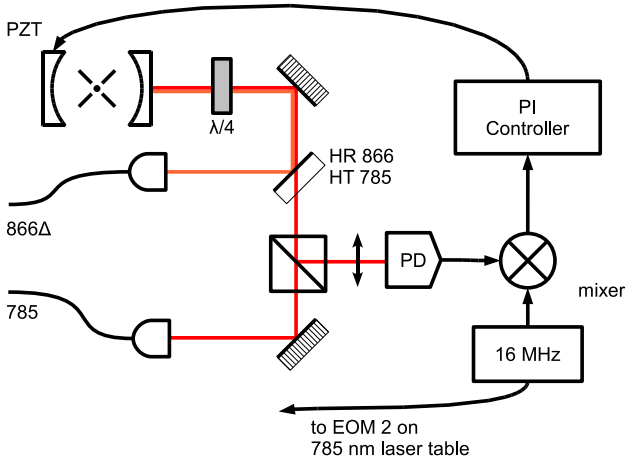

Figure 4.16: Schematic setup for the trap cavity locking scheme to the 785 nm laser.

The PZT stacks display mechanical resonances that introduce a phase of π, which in turn limits the bandwidth of the filter loop. The sound waves propagating in the cavity mount introduce mechanical stress on the PZT stacks, which in turn induce a voltage at the PZT stacks electrodes. The acoustical spectrum of the resonator can then be easily obtained by performing a Fourier transform of the induced voltage. The first mechanical resonance occurs at 5 kHz, as shown in Figure 4.17. This information was used to set the time constant of the integrator in the filter loop.

The lock ensures that the cavity resonance frequency follows the frequency of the 785 nm laser on average. Is is however important to note that the filter loop can not prevent the external excitation of resonances in the trap cavity mount. Indeed, the excessive acoustical noise present in the lab is currently limiting the stability in the millisecond timescale.

4.6.4 Trap cavity transfer-lock procedure

In order to match the Raman resonance, the trap cavity must be detuned from the $P_{1/2} \longleftrightarrow D_{3/2}$ resonance by the same detuning $\Delta \approx 400$ MHz as the driving laser.

Initially, a reference laser detuned by roughly 400 MHz from the $P_{1/2} \longleftrightarrow D_{3/2}$ resonance (866Δ in Figures 4.14 and 4.16) is overlapped with the 785 nm laser and is coupled to the trap cavity. An appropriate voltage is chosen for the slow PZT to achieve resonance at this reference frequency. By adjusting the grating and injected current, the wavelength of the 785 nm laser is coarsely chosen to simultaneously achieve resonance with its own reference cavity and with the trap cavity (double resonance). The fine adjustment is done by tuning the radio-frequency of the AOM (see Fig. 4.15). At this stage, the reference laser 866Δ is no longer necessary and is removed from the trap cavity.

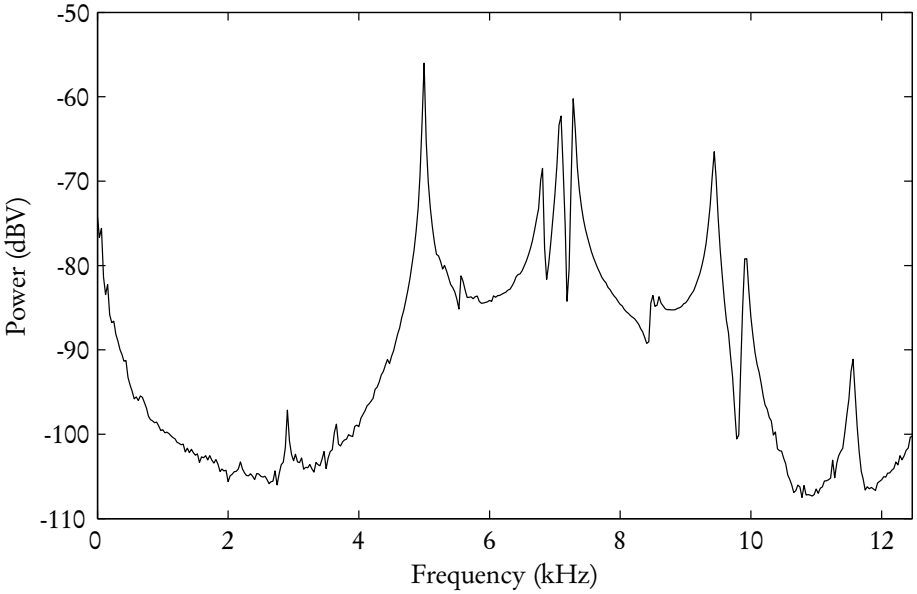

Figure 4.17: Acoustical spectrum of the trap cavity. The slow piezo was directly excited while the induced potential at the fast piezo was measured. Several resonances are visible, the most prominent of which occurs at 5 kHz.

4.7 Detection setup

4.7.1 Fluorescence detection at 397 nm

If a $^{40}Ca^{+}$ ion in the ground state is weakly driven (pumped) with a laser at some detuning Δ_p to the $S_{1/2} \leftrightarrow P_{1/2}$ transition, it will eventually absorb a photon from the laser field and the valence electron will transit to the $P_{1/2}$ state. After some time, given by the lifetime of the upper state, the ion decays back to the $S_{1/2}$ state and a photon is emitted into some direction in free space. Continuously pumping the ion forces it to radiate (isotropically) a stream of photons. If such photons are collected and detected, it is possible to obtain information about the internal state of the ion.

An additional repump laser at some small detuning Δ_r to the $D_{3/2} \leftrightarrow P_{1/2}$ transition must however be used. Otherwise, the population in the $P_{1/2}$ manifold would eventually decay to the $D_{3/2}$ state and the ion would decouple from the pump laser. The recycling laser therefore assures that the population in the $D_{3/2}$ state is transferred back to the $S_{1/2}$ state, which closes the cycle and allows the ion to emit a continuous stream of photons at both 397 and 866 nm.

Two lenses are used to collect this light, which is then detected by either a photomultiplier tube (PMT, front channel) or by an electron-multiplication charged-coupled device (EMCCD, back channel). Both of these devices are equipped with band-pass filters to prevent the detection of photons other than those at 397 nm (corresponding to the $S_{1/2} \leftrightarrow P_{1/2}$ transition).

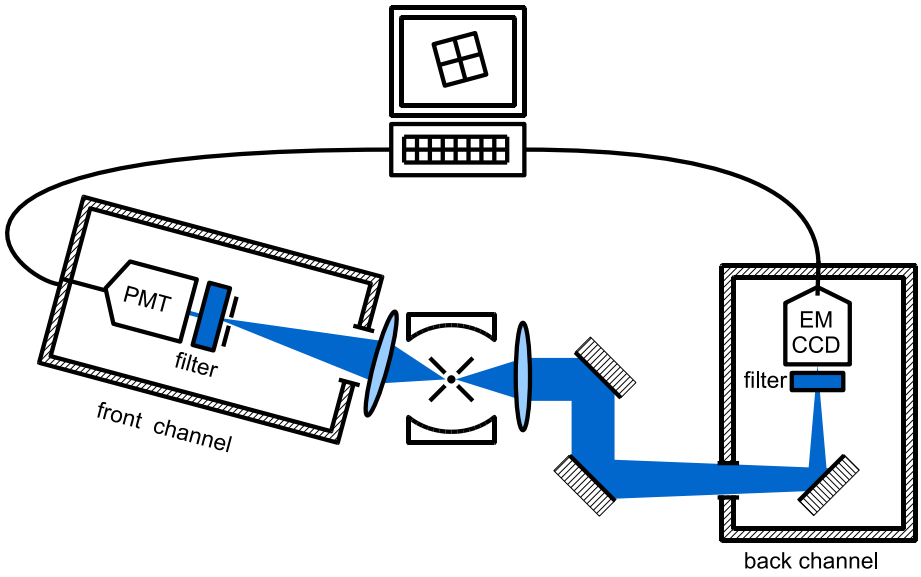

Figure 4.18: Schematic setup for the fluorescence detection at 397 nm. The front channel is displayed on the left side of the figure. The light is collected by an objective and an image of the ion is formed at a slit with a magnification ≈ 7. The slit aperture acts as a spatial filter, allowing a reduction of the background level. The light is then filtered with a bandpass filter and detected in a PMT. The back channel is represented in the right side of the figure, following a similar setup. An achromat lens is used to collect the light and an image of the ion is formed on the active area of the CCD, with a magnification of ≈ 20.

Front channel: PMT

Depending on the experiment performed, the axis of the front channel was either set perpendicular to the viewport or was setup horizontally tilted by about 10°, in order to allow optical access to the ion along the direction of the magnetic field. Figure (4.18) sketches the latter configuration. The lens in the front channel is actually a photographic objective produced by Nikon that has a working distance of ≈ 55 mm. An image (magnification ≈ 7) of the trap axis is formed in front of a rectangular aperture adjustable with four blades. This is effectively exploited to block excessive stray light: spurious scatter from the trap electrodes can therefore be largely suppressed. However, as a consequence of the relative tilt between the axis front channel and the viewport, some of the light scattered by some trap electrodes still overlaps the axis of the front channel, thus preventing a complete suppression of the spurious scatter. This imperfection does not set a hard limitation for the experiments running in this configuration: the background is only slightly higher than it could be. The remaining ambient light is further attenuated by placing an optical narrow band-pass interference filter after the aperture[3].

The aperture of the PMT objective has a diameter of 50 mm. Assuming a magnification of ≈ 7 it is possible to estimate the distance between the objective and the ion. By determining the corresponding solid angle and taking into account the loss introduced by the interference filter, the collected light available at the PMT amounts to at most $\approx 6.6\%$ of total scattered light. The supplier of the PMT model specifies a quantum efficiency of $\approx 26.5\%$, which leads to a maximum overall detection efficiency of $\approx 1.8\%$.

By fitting a series of excitation spectra of resonance fluorescence, it is possible to determine the proportionality factor R between the population in the P state and the measured count rate at the PMT. The overall detection efficiency (probability of detecting one photon emitted by the ion) can therefore be determined by $\eta_{397} = \frac{R}{\Gamma}$. For the front channel we have $\eta_{397} \approx 1.7\%$. This value agrees well with the upper limit discussed in the previous paragraph. The minor discrepancy is attributed mainly to an imperfect photon collection efficiency by the objective, and to a possible lower quantum efficiency.

Back channel: EM-CCD

The setup of the back channel is conceptually similar to the front channel and differs only in a few technical details: the axis of the channel is perpendicular to the viewport, a simple achromat lens is used instead of an objective, the CCD itself (Andor IXon DV860AC-BV) constitutes the aperture and the magnification of the image is about 20. Also, three mirrors are used to guide the collected fluorescence to the CCD. This channel is not used for the measurements, however it is of great practical importance for various routine tasks like ion loading and micromotion compensation.

[3] Semrock Brightline^{TM} FF01-377/50-25: 94% transmission at 397 nm, $< 1\%$ in the range $407 - -997$ nm

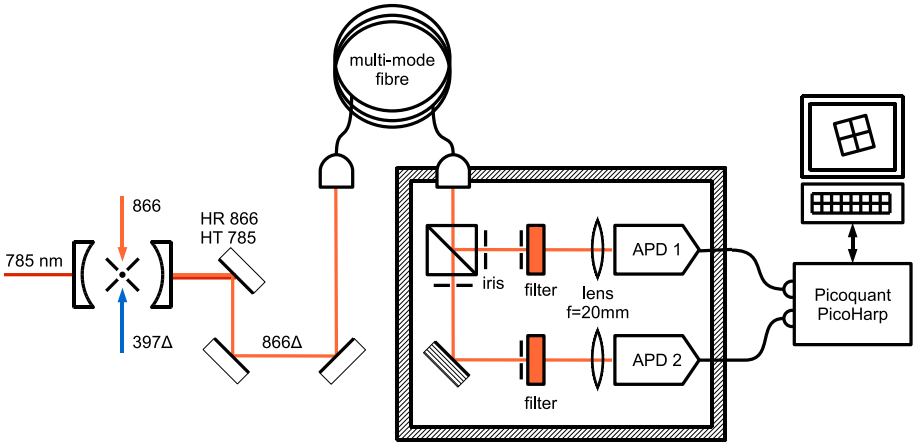

Figure 4.19: Schematic setup for the cavity output detection at 866 nm. The light at the cavity output is first filtered by three successive dichroic mirrors: light at 785 nm is transmitted whereas light at 866 nm is reflected. The filtered light is then coupled into a multi-mode fibre (core diameter 125 μm) and detected by two avalanche photodiodes (APD 1,2) in Hanbury-Brown and Twiss configuration.

4.7.2 Cavity output light detection at 866 nm

Detection setup

The light exiting the trap cavity through the output coupling mirror is collimated using a best-form lens with a focal length $f = 20$ mm, leading to a beam waist of roughly 1 mm.

The light at 785 nm is first filtered out by making use of three dichroic mirrors (see Fig. 4.19). The transmittance of the dichroic mirrors is approximately $T_{785} \approx 95\%$ at 785 nm, and the reflectance has been measured to $R_{866} = 99\%$ at 866 nm.

Most of the filtered light is therefore at 866 nm, which is then coupled into a 10 m long multimode fibre (core diameter 125 μm). The fibre was placed inside an opaque rubber hose ($\approx$ 5 mm wall thickness) to prevent the coupling of spurious ambient light through the jacket into the fibre. The amount of light transmitted by the fibre is limited by the reflections at each of the two facets ($\eta_{\text{fibre}} \approx 0.92$).

The fibre end is attached to the opaque box, which contains a beam-splitter and two avalanche photodiodes setup akin to the experiment by Hanbury-Brown and Twiss, as depicted in Figure 4.19. The box is sealed tight enough that only a negligible amount of stray light can enter.

The light coming out of the multi-mode fibre is further filtered by a band-pass filter (Omega Optical 866DF25) with 80(4)% transmission at 866 nm ($T_{\text{filter}} = 0.80(4)$) and optical density of 5 at 785 nm. To better match the beam size to the active area of the avalanche photodiodes (Perkin-Elmer SPCM-AQR-15), two best-form lenses are used.

The quantum efficiency of the single-photon detection has been measured to $\eta_{\text{APD}} = 42(1)\%$. A photoelectric detection is signalled by a TTL pulse that is 2.5 V high in a 50 Ω load, and 33 ns wide. The temporal resolution of the APDs is of 300 ps FWHM, their dead time is 88(4) ns and the specified dark-count rate is 50 Hz. The events are time-tagged and recorded using dedicated hardware (Picoquant PicoHarp)

Detection efficiency budget			
Optical losses	Dichroic mirrors	R_{866}^3	$(0.99)^3$
	Multimode fibre	T_{fibre}	0.92(5)
	Interference filter	T_{filter}	0.80(4)
Detector efficiency		η_{APD}	0.42(1)
Photon detection efficiency		η_{det}	0.38(4)

Table 4.3: Summary of the different photon losses in the detection setup at 866 nm. The photon detection efficiency η_{det} is given by $\eta_{\text{det}} = \mathrm{R}_{866}^3 \cdot T_{\text{fibre}} \cdot T_{\text{filter}} \cdot \eta_{\text{APD}}$

with a temporal resolution of 4 ps.

From the losses of the various optical elements (summarised on Table 4.3), it is possible to determine the efficiency for detecting a photon that has left the cavity, η_{det}:

$$\eta_{\text{det}} = \mathrm{R}_{866}^3 \cdot T_{\text{fibre}} \cdot T_{\text{filter}} \cdot \eta_{\text{APD}} = 0.38(4) \tag{4.28}$$

Overall photon detection efficiency

Under pulsed excitation, one photon can be emitted per trial. The probability p_{out} for that photon to leave through the output coupler is given by

$$p_{\text{out}} = \frac{\mathscr{T}_2}{\mathscr{T}_1 + \mathscr{T}_2 + \mathscr{L}} = \mathscr{T}_2 \cdot \frac{\mathscr{F}}{2\pi} \tag{4.29}$$

The probability that such a photon is actually detected is however given by p_{det}:

$$p_{\text{det}} = p_{\text{out}} \cdot \eta_{\text{det}} = 5.6\% \tag{4.30}$$

If p_{em} is the probability with which a photon is emitted into the resonator, the probability for detecting one photon upon only one excitation pulse is given by $p_{\text{succ}} = p_{\text{em}} \cdot p_{\text{det}}$.

Under continuous excitation, the photons that exit the resonator via the output coupler are a fraction of the photon stream emitted by the ion. For a stationary intra-cavity photon number n_{cav}, the rate R_{out} at which the photons leave the resonator via the output coupler is given by:

$$R_{\text{out}} = n_{\text{cav}} \cdot 2\varkappa \cdot p_{\text{out}} = n_{\text{cav}} \cdot \mathscr{T}_2 \cdot \frac{c}{2L} \tag{4.31}$$

where we used $\varkappa \approx \frac{\pi c}{2\mathscr{F}L}$. [4] The count rate at the detectors is thus given by:

$$R_{\text{det}} = R_{\text{out}} \cdot \eta_{\text{det}} = 3.8(4) \times 10^4 \cdot n_{\text{cav}}\ \text{s}^{-1} \tag{4.32}$$

[4] We can re-interpret this derivation by observing that for a photon impinging on the output coupler, the probability of it being transmitted is simply given by $\mathscr{T}_2$. The intra-cavity photons are reflected by the output mirror every roundtrip, which occurs with a frequency of $\frac{c}{2L}$. Therefore, R_{out} is simply product of the number of photons in the cavity n_{cav} with $\mathscr{T}_2 \frac{c}{2L}$.

Chapter 5

Methods

This chapter presents a basic overview of the auxiliary methods used to set up the experiment in the appropriate configuration for the various measurements. In a typical experimental run, the trap is set up, a single ion is loaded, any misalignments are corrected and the laser parameters are calibrated.

5.1 Ion loading and storage

The source of atomic calcium is an oven filled with solid calcium. By heating up the oven, the calcium vaporises and an atomic beam flows through the trapping region. There, two photo-ionisation lasers ionise the atoms [74, 79]. At the same time, a Doppler cooling laser at 397 nm and a recycling laser at 866 nm are applied. Once an ion is created, it couples to both of these lasers. To simultaneously ensure a detectable laser scattering rate and an acceptable Doppler cooling, the frequency of the blue laser at 397 nm is typically red-detuned by 160 MHz from the $S_{1/2} \leftrightarrow P_{1/2}$ transition.

The ionisation of one calcium atom is marked by a sudden increase in the laser scattering. The fluorescence photons are best detected using a differential detection scheme: the recycling laser is typically successively switched on and off every 100 ms. From the laser scattering rates, it is simple to retrieve both signal (atomic fluorescence) and background noise (spurious laser scatter). Once a signal is observed, the oven is switched off and the photo-ionisation lasers are blocked.

By continuously cycling in the $S_{1/2} \leftrightarrow P_{1/2}$ cooling transition, the ion is Doppler-cooled at an optimal detuning of γ'_{SP}, where $2\gamma'_{SP}$ is the effective (power-broadened) linewidth of the $S_{1/2} \leftrightarrow P_{1/2}$ cooling transition. Usually, the cooling transition is driven below saturation to prevent linewidth broadening and assure optimal Doppler cooling. The ion can thus reach a minimum thermal energy of the order $k_B T_{\min} \sim \hbar\gamma'_{SP}$. The frequency of the recycling laser is tuned to resonance while its power is usually set above saturation of the $D_{3/2} \leftrightarrow P_{1/2}$ transition.

Under these conditions, a single ion can be stored for days. Its fluorescence can be easily detected, as a single ion can produce a signal in excess of 50 photoelectric detections per millisecond under strong excitation.

5.2 Minimisation of micromotion

The trapping potential is only conservative if the trap centre coincides with the node of the radiofrequency potential.

If a spurious homogeneous external electric field is present at the trapping region, the equilibrium position of the ion can be shifted away from the node of the radiofrequency field. The ion is consequently driven by an extra force oscillating at the trap drive frequency. The resulting micromotion broadens the spectrum and reduces the effectiveness of laser cooling.

However, even if there is no spurious external electric field, the ponderomotive potential itself introduces some micromotion that can not be compensated [82]. The amplitude of such micromotion depends on the q-parameter of the Paul trap (see section 4.1.1).

Nevertheless, it is often the case that the micromotion present in an ion trap exceeds the minimum, due to perturbing electric fields. The literature refers multiple sources, see e.g. [82]. On the one hand, the perturbing sources may be constant over time, as is the case for the asymmetric trapping potentials introduced by an eventual excessive roughness of the surface of the trap electrodes. In the particular case of this experimental setup, the proximity of the cavity mount may also contribute to the deformation of the trapping potential in a similar fashion. On the other hand, some perturbations may change over time: it is common for an insulating patch on the trap electrodes to accumulate an electrostatic charge for some time, which can introduce a spurious electric field that may displace the trap centre.

The micromotion can be minimised by applying appropriate static potentials to the compensation electrodes [62, 72]. We followed closely the procedures described in [61, 62, 72, 73]. For completeness, we present a summarised version of the techniques used for micromotion compensation in this experimental setup.

1 A crude compensation was performed by minimising any position change of the image of the ion at the CCD while varying the radial trap potential. The best results were achieved by alternating between two different directions of the cooling beams and adjusting the voltage of the corresponding compensation electrode. The accuracy of the compensation is typically limited by the resolution of the imaging system.

2a The compensation was then improved by measuring the correlation between the photodetection and the phase of the radiofrequency field. This method is mainly limited by the quality of the signal-to-noise ratio.

2b An alternative method is based on the measurement of the width of the excitation spectrum at 397 nm. The radio-frequency field introduces sidebands at multiples of the trap drive frequency (23.4 MHz). By changing the potential of the compensation electrodes, the higher-order sidebands could be significantly suppressed, effectively reducing the linewidth of the transition.

3 The most sensitive method consisted on resolving the lines on the $S_{1/2} \longleftrightarrow D_{5/2}$ transition with the narrow-linewidth laser at 729 nm. The sidebands associated with micromotion can be well determined. The micromotion was therefore suppressed by monitoring the transition strength of one micromotion sideband while alternately adjusting the voltage of the compensation electrodes.

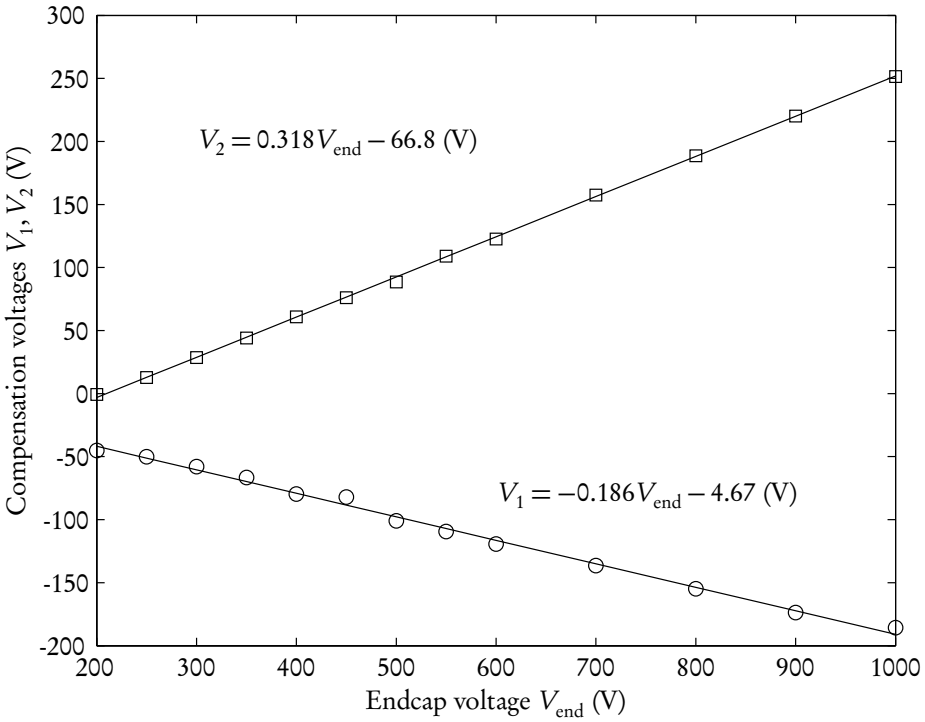

Figure 5.1: Potentials V_1 (circles) and V_2 (squares) required to compensate micromotion, as a function of the potential applied to the endcap electrodes V_{end}. The solid lines are linear fits, the best-fit solutions are given. Applying a potential V_1 to the first set of compensation electrodes shifts the equilibrium position of the trap mainly along the cavity axis, while the second set of compensation electrodes (at a potential V_2) acts mainly along axis defined by the two large viewports.

Figure 5.1 shows the results of the micromotion compensation procedure. Similarly to the linear ion trap described by S. Gulde [62], we found a linear dependence of the required compensation voltages $V_{1,2}$ on the potential applied at the endcaps, V_{end}, which is attributed to imperfect manufacturing and/or alignment of the endcap electrodes.

5.3 Positioning of the cavity relative to the trap

In the initial stages of the experiment, the trapping region was not overlapping with the cavity mode. The experimental apparatus was however designed to overcome this problem, by allowing both coarse and fine tuning of the position of the ion in the standing wave of the trap-cavity field. As the trap is rigidly attached to the vacuum chamber, the alignment is achieved by moving the cavity as a whole using piezo-driven translation stages (see section 4.2.2).

The cavity centre was aligned to the trapping region in three steps.

Step 1 A cloud of Ca^+ ions was loaded. Depending on its size, an ion cloud can easily deliver count rates of 200 kHz at the photomultiplier tube and typically has

a large spatial extension ($\sim 50\ \mu$m), exceeding the waist of the cavity mode ($w_0 \approx 13\ \mu$m).

The frequencies of both cooling and recycling lasers were first set near-resonant to the ion cloud and the trap-cavity was set resonant to the recycling light at 866 nm. The trap-cavity was filled with light at 866 nm, while the cooling laser excited the ions from the side of the cavity. Consequently, the fluorescence at 397 nm depended on the spatial overlap between the ion cloud and the cavity mode. By iteratively changing the cavity position along the various directions, it was possible to maximise the fluorescence at 397 nm.

This procedure allowed us to position the cavity axis to within $\approx 50\ \mu$m of the trapping region.

Step 2 The procedure above was then repeated for a single $^{40}Ca^{+}$ ion with some minor adaptations.

First, the sub-wavelength localisation of the ion imposed special care on each iteration, as the anti-node position had to be determined. Second, the intra-cavity field at 866 nm suffered large oscillations at the position of the ion. The residual mechanical oscillations in the trap cavity introduce a jitter in its resonance frequency. The excursion of the frequency jitter is estimated to ≈ 1 MHz, which exceeds both the laser linewidth ($\delta_{\mathrm{recyc}}/(2\pi) = 200$ kHz) and the cavity linewidth $\varkappa/(2\pi) = 54$ kHz, and is periodic with the first (and dominant) mechanical resonance at 5 kHz. Such jitter prevents the coupling of the laser light at 866 nm with a constant intensity, thus leading to variations of the intensity of the intra-cavity field. As a result, the measurement of the average fluorescence level at 397 nm was only meaningful if integrated over a period of time of around one second. Third, as the method converged and the cavity centre approached the trapping region, the average intensity of the 866 nm had to be reduced, in order to keep the excitation below saturation.

This method allowed the approximate determination of the cavity position along the axial direction to within a few Rayleigh lengths (with $z_R \approx 0.6$ mm).

Step 3 The final step consisted of maximising the coupling to the vacuum-stimulated Raman transition (explained in greater detail in section 5.5).

Both driving and recycling beams excited a single ion and were set transverse to the cavity axis. The driving laser and the trap-cavity were set to the same detuning ($\Delta \approx -400$ MHz) from the $S_{1/2} \leftrightarrow P_{1/2}$ transition, while the recycling beam was kept near-resonant to the $D_{3/2} \leftrightarrow P_{1/2}$ transition. As shall be explained in more detail in section 5.5, in this configuration the ion continuously emits photons into the cavity: a stationary cavity field builds up, and the photon stream leaving through the output-coupling mirror can be observed. The dependence of the intensity of the photon stream on the position of the ion in the cavity was used to map out the standing wave inside the cavity (see section 5.5.3), as well as the overall optimum cavity position.

Daily operation As mentioned in section 4.4, a design flaw allows a thermal contact between the calcium oven and the cavity assembly when the cavity is optimally positioned. The problem is currently circumvented by displacing the cavity whenever it is necessary to load calcium ions.

To prevent a severe misalignment, we currently use a laser pointer to mark the optimal longitudinal position of the cavity. The end of a single-mode fibre is perma-

nently secured on the experiment table and the out-coupling laser beam is directed between one edge of the cavity mount and one edge of the holder for the collimation lenses (structures D and G in Figure 4.8), such that the beam illuminates both edges. This simple procedure allows us to mark the correct position of the cavity mount. The cavity can be moved away for a few millimetres, thus allowing the loading of load ions. Once the trap is loaded, the cavity is moved back until it is in position with the laser pointer beam. The cavity position is usually very close to the optimum. For safeguard, the cavity position is corrected by using the procedure described in step 3.

5.4 Calibration of experimental parameters

In this section, the calibration procedure for the various experimental parameters is described. The results are summarised in Table 5.1.

5.4.1 Calibration of magnetic field and trap frequencies

The experimental setup is biased with a magnetic field induced by a pair of Helmholtz coils mounted in the two CF200 viewports. The magnitude of the magnetic field was initially measured by resolving the frequency of several Zeeman lines on the quadrupole transition $S_{1/2} \leftrightarrow D_{5/2}$ at 729 nm [61, 62, 69, 72, 83]. This standard procedure was repeated for different currents, effectively establishing a calibration curve with less than 5 % error.

5.4.2 Laser parameters

The multi-level structure of $^{40}Ca^{+}$ is revealed through the existence of various dark resonances [84] in the excitation spectra. Up to eight such resonances can be observed, corresponding to the possible two-photon transitions between the Zeeman states of the $S_{1/2}$ and $D_{3/2}$ manifolds. The number of dark resonances can be reduced to four by selecting the polarisations of both cooling and recycling laser beams appropriately.

In the experiments, the excitation spectra are obtained by sweeping the recycling laser frequency across resonance while the average count-rate of photoelectric detections of the resonance fluorescence of the ion in the $S_{1/2} \leftrightarrow P_{1/2}$ transition is recorded.

The excitation spectra can be easily numerically modelled. Figure 5.2 shows nine simulations of the excitation spectra, organised in three plots. These simulations make use of the 8-level model described in chapter 3 for a single calcium ion at rest.

The top, middle and bottom plots correspond to excitation spectra for different cooling and recycling Rabi frequencies. Within each plot, three curves are represented, for different magnetic fields and laser linewidths. The position and separation of the various dark resonances are given by the detuning of the cooling beam and the magnitude of the magnetic field, respectively, while their width and depth depend on the combined laser power and laser linewidth.

The sensitivity of the excitation spectra to variations of these parameters was exploited to calibrate the experimental parameters. Figure 5.3 shows an excitation spectrum and the corresponding fit, where the Rabi frequencies (Ω_{driv} and Ω_{recyc}) and the magnetic field B were set as fit variables. The shaded grey area corresponds to a 95% confidence interval on the fit parameters.

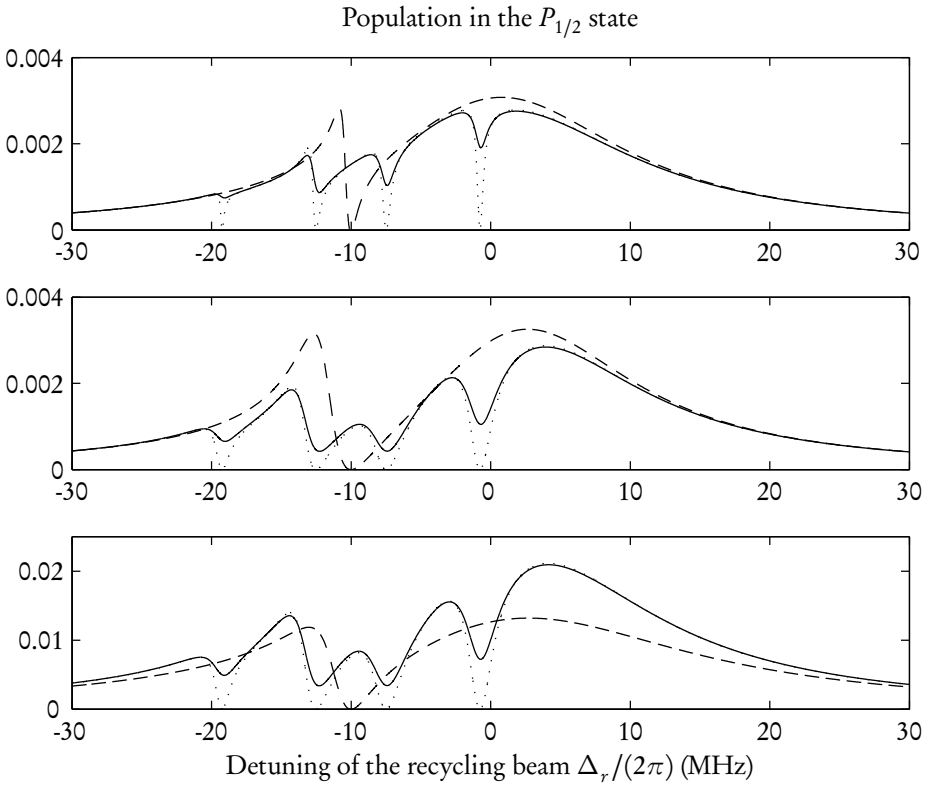

Parameters used for the simulations:

Plot	$\Omega_{\text{cool}}/(2\pi)$ (MHz)	$\Omega_{\text{recyc}}/(2\pi)$ (MHz)
Top	10	1
Middle	20	1
Bottom	20	3

Line	$\delta_{\text{driv}}/(2\pi)$ (kHz)	$\delta_{\text{recyc}}/(2\pi)$ (kHz)	B (G)
Dashed	0	0	0.03
Dotted	0	0	3
Solid	100	100	3

Figure 5.2: Simulated excitation spectra exhibiting dark resonances. The population of the $P_{1/2}$ is displayed in the vertical axis as a function of the detuning of the recycling laser. In all cases the detuning of the cooling laser was set to $\Delta_{\text{cool}}/(2\pi) = -10$ MHz and the polarisations of both lasers were set orthogonal to the direction of the magnetic field. At zero magnetic field (dashed lines), the Zeeman structure is not resolved, i.e., a single dark resonance is observed. At a magnetic field of 3 G, four resonances are resolved. The width of these resonances depends mainly on the laser power. The non-zero linewidth of the lasers introduces phase noise that partially destroys the dark resonance, consequently populating the $P_{1/2}$ state.

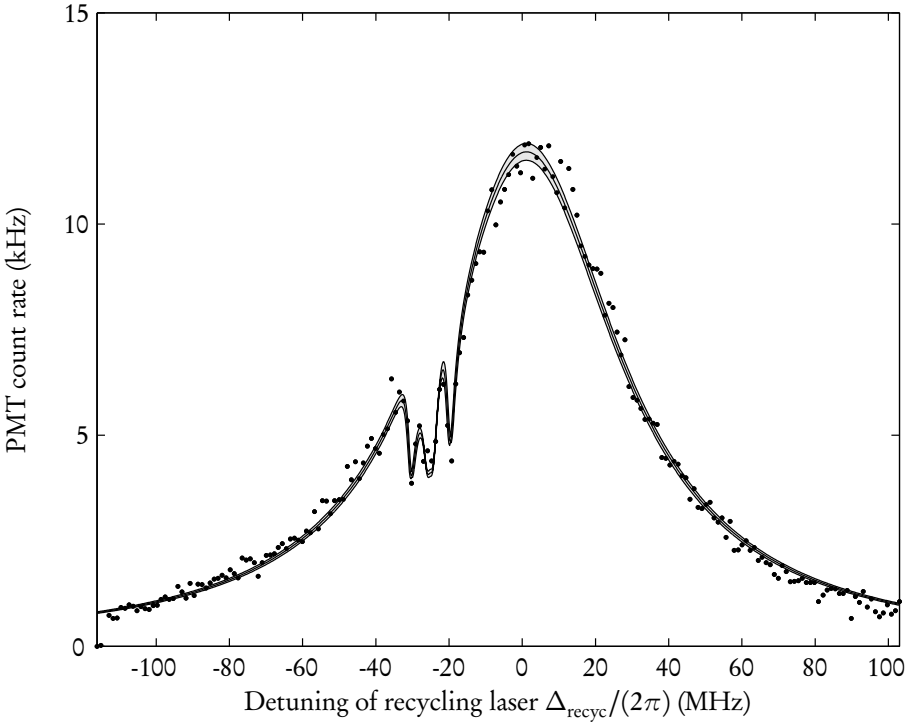

Figure 5.3: Excitation spectrum, obtained by sweeping the detuning of the recycling laser at 866 nm. The polarisations of the cooling and recycling beams were chosen parallel and perpendicular to the direction of the magnetic field, respectively. The dots mark the experimental data points, while the three solid lines are obtained from a fitting procedure. The central solid line is the best fit solution, with Rabi frequencies $\Omega_{\mathrm{cool}}/(2\pi) = 19(2)$ MHz, $\Omega_{\mathrm{recyc}}/(2\pi) = 11.9(1)$ MHz, detuning at 397 nm $\Delta_{\mathrm{cool}}/(2\pi) = -25.2$ MHz and magnetic field $B = 2.7(1)$ G. The grey shaded area delimited by the two other solid lines contains the set of solutions in a 95% confidence interval on all fitted parameters.

Calibration of the cooling and recycling beams

In a first calibration step, the cooling beam was red-detuned from the resonance by less than one linewidth. An excitation spectrum exhibiting four dark resonances is first obtained by sweeping the detuning of the recycling laser.

A series of spectra for various laser intensities and cooling laser detunings are measured and the resulting data is fitted. The laser detunings [1] ($\Delta_{\text{cool}}, \Delta_{\text{recyc}}$), laser linewidths ($\delta_{\text{driv}}$ and δ_{recyc}) and Rabi frequencies ($\Omega_{\text{cool}}, \Omega_{\text{recyc}}$) are determined, the detection efficiency is inferred and the magnitude of the magnetic field B is confirmed.

This procedure is repeated occasionally over the course of time to confirm the general stability of the setup. The laser linewidths derived with this method agree well with an estimate based on the residual error signal of the Pound-Drever-Hall lock of the lasers to stable cavities.

Under normal operation conditions, the number of spectra required to perform a consistent calibration from the fitting procedure is significantly reduced, as only the laser detunings and Rabi frequencies need to be varied. The ratio $\Omega^2_{\text{recyc}}/I_{\text{recyc}}$ between the Rabi frequency and intensity of the recycling beam was measured at low intensities, where $\Omega_{\text{recyc}} \lessapprox 20$ MHz.

At higher intensities of the recycling laser, the excitation spectra become increasingly unstable and cease to be reliable for a direct calibration of the laser intensities. Therefore, the Rabi frequency Ω_{recyc} of the recycling beam was indirectly determined by measuring the optical intensity I_{recyc} and applying the ratio $\Omega^2_{\text{recyc}}/I_{\text{recyc}}$. For the measurements presented in this regime a neutral density filter with a calibration error of 10% was introduced in front of the photodiode used for intensity stabilisation. This error adds to the calibration error of Rabi frequencies in this regime.

Calibration of the driving beam

The vacuum-stimulated Raman transitions make use of a driving beam red-detuned from the $S_{1/2} \leftrightarrow D_{3/2}$ transition by ≈ 400 MHz. The driving and cooling beams share the same laser source but follow different paths in the experimental setup. From the calibration of the cooling beam, the detuning of the driving beam can be readily calculated to within an error of $\epsilon(\Delta_{\text{cool}}) = \epsilon(\Delta_{\text{driv}}) \approx 0.3$ MHz. However, the determination of the Rabi frequency of the driving beam requires extra measurements.

The ion is illuminated with both the driving and recycling laser beams. The recycling laser frequency is swept across the resonance and a new series of excitation spectra are obtained, for several recycling laser intensities.

The off-resonant excitation of the $P_{1/2}$ state depends on the Rabi frequency of the driving beam and on the detuning of the recycling laser. Although dark resonances are no longer observed, the intensity and width of the peaks in the spectra have a dependence on the intensity of the driving laser. The Rabi frequency of the driving beam (Ω_{driv}) is therefore extracted from a fitting procedure, whose consistency is verified by recording a series of spectra for different intensities.

[1] All laser detunings are given with respect to the unperturbed atomic levels: $B = 0$ and $\Omega = 0$.

parameter	typical value (MHz)	relative error
Δ_{cool}	-10	2.5×10^{-3}
Δ_{driv}	400	2.5×10^{-3}
Ω_{cool}	$0 \ldots 250$	5%
δ_{driv}	0.3	12 %
Δ_{recyc}	$-20 \ldots 20$	10 %
Ω_{recyc} (< 20 MHz)	$0 \ldots 20$	5 %
Ω_{recyc} (> 20 MHz)	$20 \ldots 350$	15 %
δ_{recyc}	0.1	70 %
Δ_c	$390 \ldots 410$	2.5×10^{-3}

Table 5.1: Estimated uncertainties for the calibration of relevant experimental parameters. Note that the linewidth δ_{recyc} of the recycling laser has negligible influence on the experimental results. Furthermore, to stabilise the intensity of the recycling laser for $\Omega_{\text{recyc}} > 20$ MHz, a neutral density filter is inserted which introduces an additional uncertainty in this regime.

5.5 Vacuum-stimulated Raman transitions

In Chapter 2, we have shown that a laser and a cavity interacting with a three-level atom can be used to establish a Raman transition between two levels. Due to the quantum-mechanical nature of the atom-cavity coupling, such interaction exists even if the cavity is not populated by photons, hence the name *vacuum-stimulated Raman transition*.

The calcium ion has a rich level structure and the light emitted by the ion into the cavity exhibits a complex spectroscopic and polarisation structure. In order to quantitatively describe the system, the atomic Zeeman sub-states and the two polarisations of the cavity field must be considered. In the following, the experimental results will be compared to the realistic model developed in chapter 3.

5.5.1 Experimental setup

In the experiment, the stream of photons leaving through the output-coupling mirror is detected using single-photon counting avalanche photodiodes, as depicted in Figure 5.4. The ion is externally driven at 397 nm by a beam detuned by ≈ -400 MHz from the $S_{1/2} \leftrightarrow P_{1/2}$ transition. The beam configuration is sketched in Figure 5.5. The driving beam (397Δ) is orthogonal to the magnetic field and lies in the plane defined by the trap and the cavity axis. The recycling beam (866) is at an angle of 45° with the magnetic field, but lies in the plane defined by the trap axis and the magnetic field.

5.5.2 Spectra of the cavity output

An excitation spectrum of the cavity output can be observed by continuously exciting the ion with both driving and recycling lasers, while sweeping the cavity detuning and recording the count rate of the photoelectric detections.

As the cavity detuning is swept, the conditions for the different Raman transitions are successively met, which will have an impact on the stationary intracavity

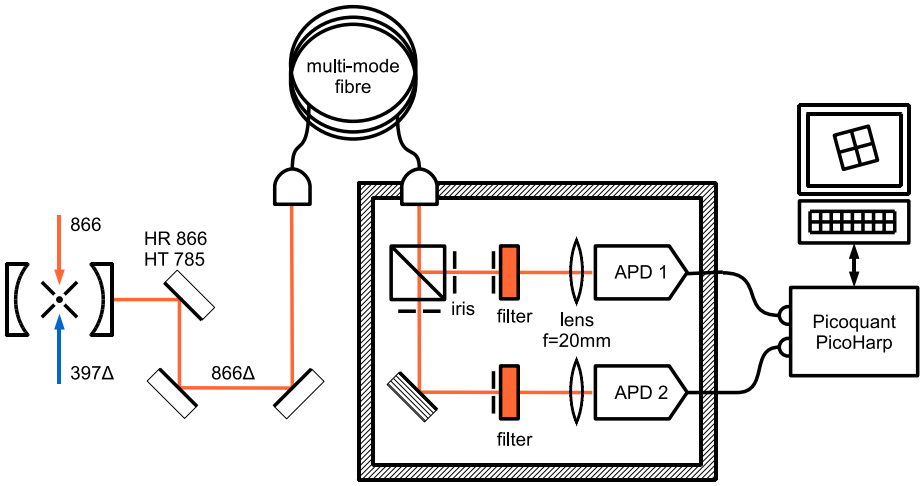

Figure 5.4: Schematic experimental setup for continuous photon generation. The driving beam (397Δ) is detuned by $\Delta_{\text{driv}}/(2\pi) \approx -400$ MHz from the $S_{1/2} \leftrightarrow P_{1/2}$ resonance, while the frequency of the recycling beam is detuned by $\Delta_{\text{recyc}}/(2\pi) \approx -20$ MHz. Both beams excite the ion from the side of the cavity. The photon stream leaving the cavity through the output coupling mirror (866Δ) is collected and detected by two single-photon counting avalanche photodiodes set up in Hanbury-Brown and Twiss configuration. The photoelectric detection times are discriminated and digitally stored for posterior processing.

photon number and thus influences the rate at which the photons leaving the cavity are detected.

Driving schemes

The Zeeman structure of the two manifolds ($S_{1/2}$ and $D_{3/2}$) must be considered in order to determine the expected spectrum of the Raman transitions. The allowed transitions are determined by imposing energy conservation on the two-photon transitions that virtually populate the $P_{1/2}$ state. For a non-zero magnetic field, there are eight possible vacuum-stimulated Raman transitions. For two configurations of the polarisation (π or σ) of the driving laser at 397 nm, the number of lines reduces to six (see Table 5.2 and Figure 5.7).

In the π driving scheme (see Fig. 5.6), the polarisation of the driving beam is parallel to the magnetic field. Under these conditions, the driving beam at 397 nm can only excite transitions that conserve the angular momentum of the atom. Therefore, only the two transitions $|S_{1/2}, m_s = \pm 1/2\rangle \leftrightarrow |P_{1/2}, m_p = \pm 1/2\rangle$ are possible.

Similarly, in the σ scheme, the polarisation of the driving beam is perpendicular to the magnetic field and only transitions between states that differ by $\pm\hbar$ in angular momentum can be excited. This effectively selects the two transitions $|S_{1/2}, m_s = \pm 1/2\rangle \leftrightarrow |P_{1/2}, m_p = \mp 1/2\rangle$.

Table 5.2 shows a list of all possible Raman transitions, as well as the detunings at which they occur (ΔE_{sd}, relative to the line at zero magnetic field) for the beam configuration described in Figure 5.5, for both π and σ configurations.

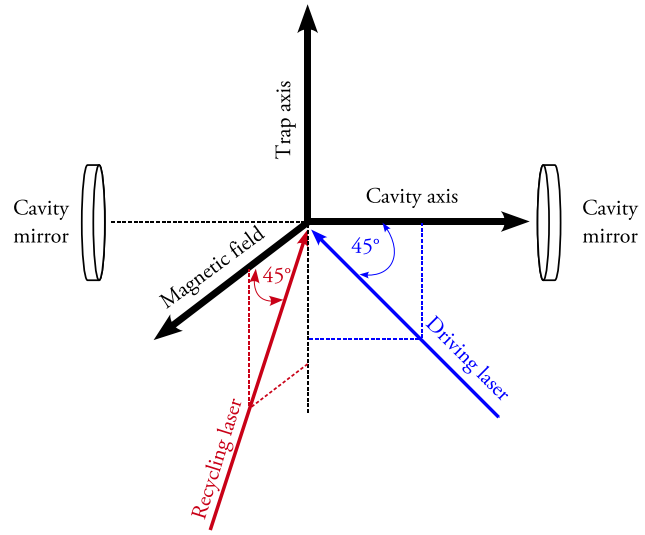

Figure 5.5: Configuration of the laser beams relative to the coordinate system defined by the trap axis, cavity mode and direction of magnetic field. The driving laser lies in the plane defined by the cavity mode and the trap axis and is at an angle of 45° with them. The recycling laser lies in the plane defined by the magnetic field and the trap axis and is at an angle of 45° with them.

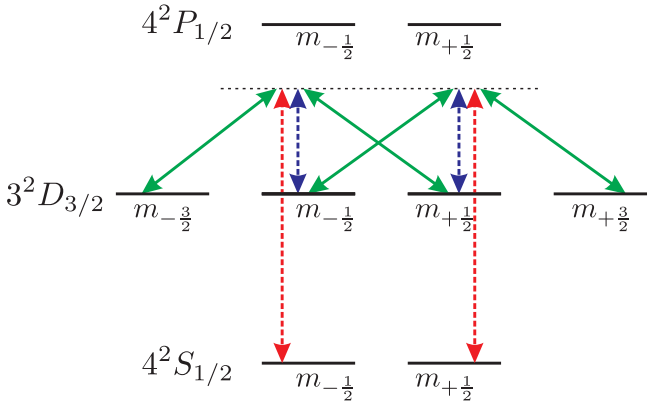

Figure 5.6: Transitions for the ion-cavity system in π configuration. The driving laser is represented in red, its polarisation allows only transitions for which $m_p = m_s$. In the experiment, the photons corresponding to transitions in green (blue) are measured with vertical (horizontal) polarisation.

The spectrum of the cavity output is sketched in Figure 5.7, which also illustrates the maximum and effective line strengths.

The maximum line strength of a particular transition $|S_{1/2}, m_s\rangle \leftrightarrow |D_{3/2}, m_d\rangle$ is given by the product of the square of Clebsch-Gordan coefficients for the corresponding $|S_{1/2}, m_s\rangle \leftrightarrow |P_{1/2}, m_p\rangle$ and $|P_{1/2}, m_p\rangle \leftrightarrow |D_{3/2}, m_d\rangle$ transitions.

The effective line strengths correspond to the experimental configuration and the polarisation of the laser and cavity fields, as well as to the direction of the quantisation axis must be taken into account.

Applying the method developed in section 2.2.2 to the full model of chapter 3, it becomes clear that the Hamiltonian for the vacuum-stimulated Raman interaction between the states $|S, m_s\rangle$ and $|D, m_d\rangle$ is given by

$$\hat{H}_{\text{Raman}} = \frac{1}{\Delta} \times \frac{\Omega_{\text{driv}}}{2} \left(\vec{\epsilon}_{\text{driv}} \cdot \mathbf{d}^{P_{1/2},\pm 1/2}_{S_{1/2},\pm 1/2} \right) e^{-i\vec{k}_{\text{driv}}\cdot\vec{r}} \times \\ \times\, g \left[(\vec{\epsilon}_a + \vec{\epsilon}_b) \cdot \mathbf{d}^{D_{3/2},m_d}_{P_{1/2},\pm 1/2} \right] \sin(\vec{k}_c \cdot \vec{r}) \times \hat{\sigma}_{D,m_d;S,m_s} + h.c. \quad (5.1)$$

Therefore, the effective strength of each line $I_{|S_{1/2},m_s\rangle \leftrightarrow |D_{3/2},m_d\rangle}$, for both in π and σ configurations, is respectively given by:

$$I^{\pi}_{|S_{1/2},\pm 1/2\rangle \leftrightarrow |D_{3/2},m_d\rangle} \propto \left| \left(\vec{\epsilon}_{\text{driv}} \cdot \mathbf{d}^{P_{1/2},\pm 1/2}_{S_{1/2},\pm 1/2} \right) \cdot \left[(\vec{\epsilon}_a + \vec{\epsilon}_b) \cdot \mathbf{d}^{D_{3/2},m_d}_{P_{1/2},\pm 1/2} \right] \right|^2 \quad (5.2)$$

$$I^{\sigma}_{|S_{1/2},\pm 1/2\rangle \leftrightarrow |D_{3/2},m_d\rangle} \propto \left| \left(\vec{\epsilon}_{\text{driv}} \cdot \mathbf{d}^{P_{1/2},\mp 1/2}_{S_{1/2},\pm 1/2} \right) \cdot \left[(\vec{\epsilon}_a + \vec{\epsilon}_b) \cdot \mathbf{d}^{D_{3/2},m_d}_{P_{1/2},\mp 1/2} \right] \right|^2 \quad (5.3)$$

where $\mathbf{d}^{V,m_v}_{U,m_u}$ is the atomic dipole vector for the $|U, m_u\rangle \leftrightarrow |V, m_v\rangle$ transition (see section 3.2.2); $\vec{\epsilon}_{a,b}$ are the polarisation vectors for the two cavity modes (which are linearly polarised along the magnetic field and the trap axis, respectively); and $\vec{\epsilon}_{\text{driv}}$ is the polarisation vector of the driving laser.

Given that it is not possible to find an experimental configuration that maximises the coupling in all lines at once, the effective line strengths are typically smaller than their maximum, as can be observed in Table 5.2 (last column) and in Figure 5.7.

The cavity is polarisation-degenerate: for a given frequency, the cavity supports two modes with orthogonal polarisations. In the experiment, the magnetic field is perpendicular to the cavity axis. As a result, the choice of a particular driving scheme means the emitted photons are detected with either vertical or horizontal polarisations (light and dark grey lines of Figure 5.7).

To illustrate the physical reality of the two driving schemes, Figure 5.8 shows the excitation spectra obtained at a low magnetic field, for both π and σ configurations. Although the individual Zeeman transitions are not resolved, it is possible to distinguish the two driving schemes. Experimentally, the two measurements correspond to the same intensity of the driving laser and were taken one after the other by rotating a $\lambda/2$ waveplate in the 397Δ beam. At a low magnetic field, the Raman transitions are not resolved. In π configuration, the frequency spacing between the lines is smaller, which leads to a better spectral overlap and higher photon emission rates.

Resolving individual Raman lines

By increasing the magnitude of the magnetic field, individual Raman resonances become visible, as shown in Figure 5.9. As with most measurements, the data was taken

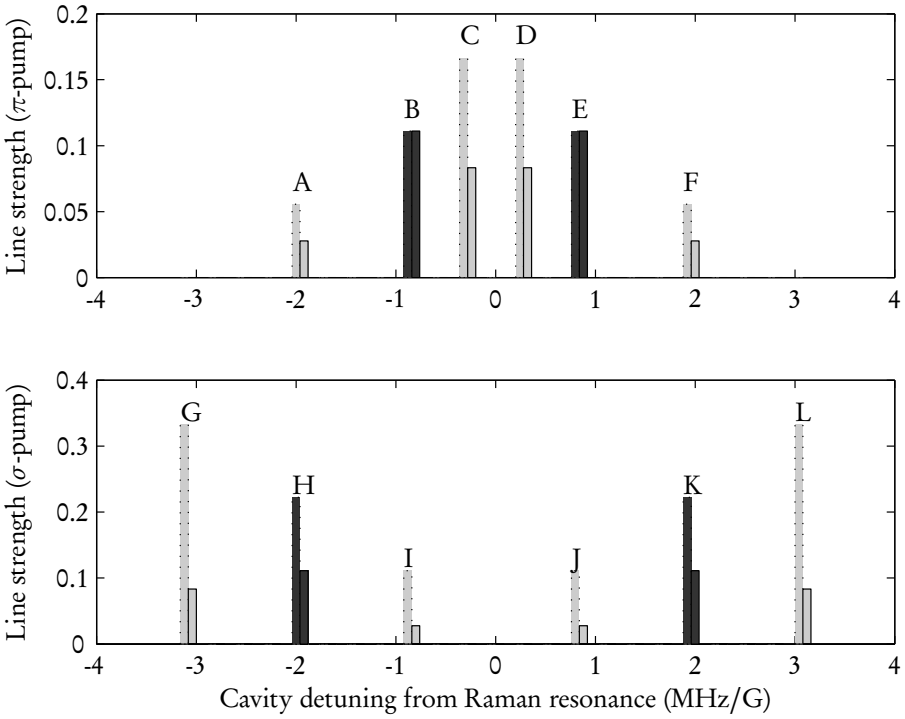

Figure 5.7: Line strengths for different driving schemes, both in the ideal case (bars with dotted lines) and as used in the experiment (bars with solid lines). The polarisation of the driving beam is set parallel to the magnetic field in the π configuration (top), whereas it is set perpendicular to the magnetic field in the σ configuration (bottom). The cavity output displays resonances at different frequencies, as obtained from energy conservation for the two-photon transitions. The height of the bars is proportional to the square of the Clebsch-Gordan coefficient associated with the Raman transition. The bars with dotted lines represent the maximum possible strength of each line. The bars with solid lines represent the spectrum that is to be expected experimentally, since they take into account the projection onto the atomic dipole of the electric fields of the driving laser and of the photons emitted into the cavity mode, in the beam configuration used in the experiment, as depicted in Figure 5.5. The lines represented by light grey bars correspond to a virtual $|P_{1/2}, m_p\rangle \leftrightarrow |D_{1/2}, m_d\rangle$ σ transition for which $m_d - m_p = \pm 1$. Likewise, the lines represented by the dark grey bars are associated to a virtual $|P_{1/2}, m_p\rangle \leftrightarrow |D_{1/2}, m_d\rangle$ π transition (with $m_d = m_p$). See Table 5.2 for more specific information on the lines A–L.

Line	from $\lvert S_{1/2}, m_s\rangle$	via virtual $\lvert P_{1/2}, m_p\rangle$	to $\lvert D_{3/2}, m_d\rangle$	m_{sp}	m_{dp}	$\Delta E_{sd}/(\mu_B B)$	max. line strength	eff. line strength
A	$+1/2$	$+1/2$	$-1/2$	0	$+1$	$-7/5$	1/18	1/36
B	$+1/2$	$+1/2$	$+1/2$	0	0	$-3/5$	1/9	1/9
C	$+1/2$	$+1/2$	$+3/2$	0	-1	$+1/5$	1/6	1/12
D	$-1/2$	$-1/2$	$-3/2$	0	$+1$	$-1/5$	1/6	1/12
E	$-1/2$	$-1/2$	$-1/2$	0	0	$+3/5$	1/9	1/9
F	$-1/2$	$-1/2$	$+1/2$	0	-1	$+7/5$	1/18	1/36
G	$+1/2$	$-1/2$	$-3/2$	-1	$+1$	$-11/5$	1/3	1/12
H	$+1/2$	$-1/2$	$-1/2$	-1	0	$-7/5$	2/9	1/9
I	$+1/2$	$-1/2$	$+1/2$	-1	-1	$-3/5$	1/9	1/36
J	$-1/2$	$+1/2$	$-1/2$	$+1$	$+1$	$+3/5$	1/9	1/36
K	$-1/2$	$+1/2$	$+1/2$	$+1$	0	$+7/5$	2/9	1/9
L	$-1/2$	$+1/2$	$+3/2$	$+1$	-1	$+11/5$	1/3	1/12

Table 5.2: Spectral lines associated with the vacuum-stimulated Raman transitions. Here $\hbar m_{sp}$ and $\hbar m_{dp}$ are the angular momenta carried by the photon absorbed at 397 nm and by the photon emitted at 866 nm respectively during the Raman transition from $S_{1/2}$ to $D_{3/2}$ via a virtual $P_{1/2}$ state. The maximum line strength is calculated as the product of the Clebsch-Gordan coefficients associated with the pump and Stokes transitions composing the Raman transition. The effective line strength takes into account the particular configuration of this experimental setup, by considering the projection onto the atomic dipole of the electric fields of the driving laser and of the photons emitted into the cavity mode. See Figure 5.7 for a graphical representation of these lines, including their individual coupling strengths.

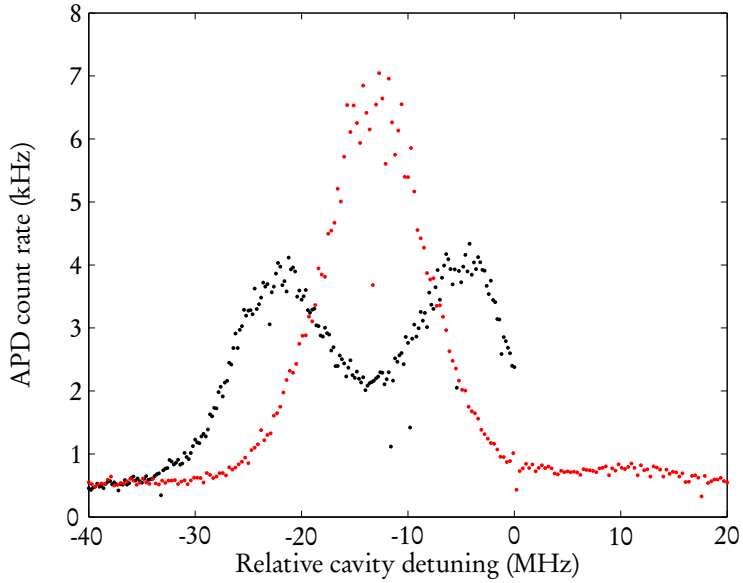

Figure 5.8: Spectrum of the cavity output at a magnetic field of $B \approx 3$ G, taken with the driving laser in π and σ configurations (red and black dots, respectively). The difference in the height of the peaks is due to a better spectral overlap of the lines for the π configuration (in red).

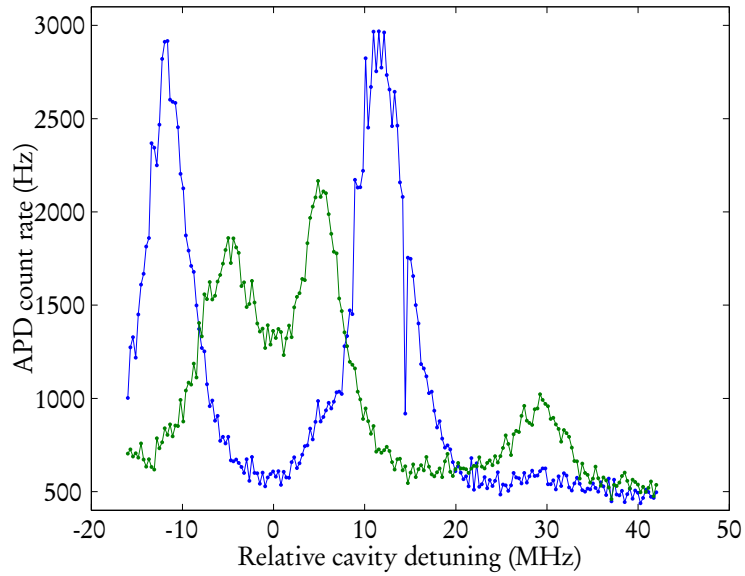

Figure 5.9: Partial spectrum of the cavity output in π configuration at a magnetic field of $B \approx 13$ G, obtained by filtering the polarisation of the output light. The blue (green) line corresponds to the horizontally (vertically) polarised light, which in turn corresponds to π ($\sigma^{\pm}$) photons emitted into the cavity. The spectrum corresponds to the configuration shown in Figure 5.7 (top).

with the driving laser in π configuration. Here, the photon stream at the cavity output was filtered by a polariser before it was detected. The axis of the polariser was set horizontally for the data set represented in blue and vertically for the green curve. The individual peaks can be resolved and compared well with the lines of Figure 5.7 (top).

5.5.3 Localisation of the ion in the intracavity standing wave

Up to now, the motion of the ion in the trap has been neglected. As we will see in this section, insufficient cooling leads to a larger size of the ion's wavefunction, effectively reducing the ion-cavity coupling. We explore this effect by mapping out the standing wave of the cavity using the ion as a probe [26].

The absolute position of the ion is determined by the trapping potential. In ion traps, the localisation of the ion is mainly limited by the residual motion of the ion, which can be controlled by appropriate cooling techniques, like Doppler- or sideband-cooling. If the ion was a point particle at rest and its positioning along the cavity axis was scanned, the cavity output would be proportional to a squared sinusoidal function of the ion-cavity displacement. The intra-cavity standing wave could be perfectly mapped: the cavity output would be zero on a node and maximum on an anti-node. This is however not exactly the case: the non-perfect localisation of the ion reduces the visibility.

We performed an experiment under conditions similar to the previous sections: the ion was driven with the detuned 397 nm laser such that photons were emitted into the cavity. The experimental parameters were optimised for maximum count rate.

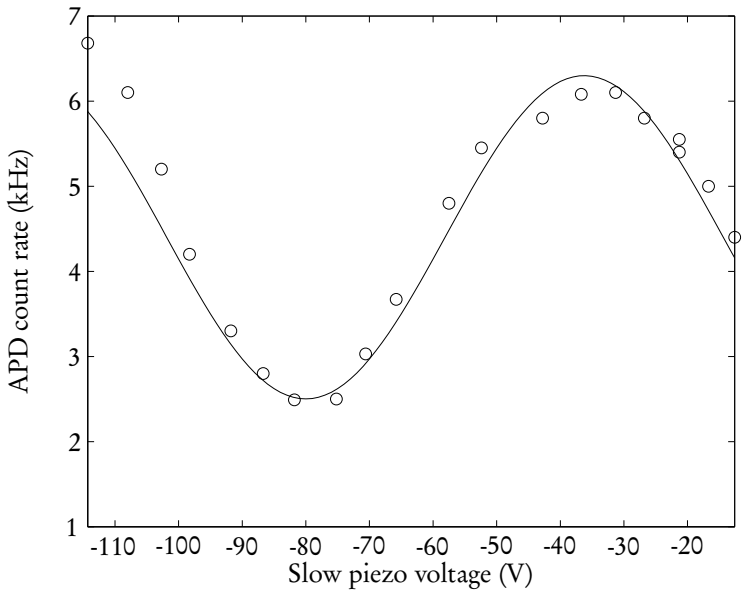

Figure 5.10: APD count rate as a function of the longitudinal position of the ion in the standing wave. The solid curve is the convolution of a scaled $\sin^2$ function with a Gaussian distribution of position spread over a standard deviation of $\sigma = 82$ nm

The variation of the measured count rate of the cavity output as a function of the relative positioning between the cavity and the ion is marked as circles in Figure 5.10. The variation of the ion-cavity relative positioning is achieved by biasing the slow PZT on one cavity mirror while keeping the cavity length locked. The solid line is a fit to a squared sinusoidal function convoluted with a Gaussian spread of the ion position. The observed visibility can be attributed to an ion wavepacket localisation $\sigma = \sqrt{\langle x^2 \rangle - \langle x \rangle^2} \approx 82$ nm along the cavity axis.

The delocalisation of the ion can be attributed to mechanical vibrations of the centre-of-mass of either the U-shaped cavity holder or the trap mount, due to excitation by external acoustical noise, but it can also be attributed to residual motion in the trap, due to imperfect cooling [26, 85]. In the first case, the extent of the mechanical vibrations could be determined by interferometric measurements. In the latter case, the only laser-cooling mechanism present in the system is the off-resonant excitation of the $P_{1/2}$ manifold by the driving laser and subsequent inelastic scattering. Please note that the ion trap can be understood in terms of a tridimensional harmonic potential with the axial and radial trap frequencies at 1 MHz and 3 MHz, respectively. If the mechanical vibrations of the cavity mount and of the ion trap turn out to be sufficiently small, the limited contrast of Figure 5.10 can be fully attributed to a delocalisation due to the motion of the ion. In such case, we estimate an upper limit for the average phonon occupation number of $\langle n_{\mathrm{phon}} \rangle \approx 90$ [2].

5.5.4 Comparison of measured and simulated spectra

The residual motion in the trap allows inelastic Raman transitions to take place, which broaden the excitation spectrum of the cavity output. Consequently, the individual Raman transitions cannot be easily resolved.

Figure 5.11 shows the spectrum of the cavity output at an anti-node for three situations: a simulation of the ideal case where the ion is at rest (solid red line), the measured spectrum (blue dots) and a simulation of the spectrum considering a motional state compatible with the measurement in Figure 5.10. The latter simulation includes transitions up to the second harmonic of the trap frequencies and is in excellent agreement with the experimental data.

[2] For such large mean phonon numbers, the system is no longer strictly in the Lamb-Dicke regime, and some usual approximations are no longer valid. The full expression for the strength of the sideband transitions must then be considered [59].

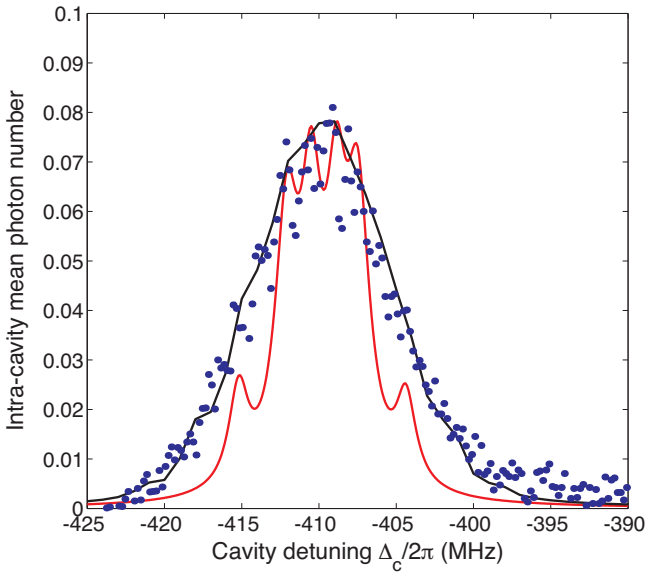

Figure 5.11: Average intra-cavity photon number at steady state, as a function of the cavity detuning Δ_c to the resonance frequency of the $P_{1/2} \leftrightarrow D_{3/2}$ transition. The Rabi frequency and detuning of the driving laser was set at $(\Omega_{\text{driv}}, \Delta_{\text{driv}})/(2\pi) \approx (220, -400)$ MHz while the recycling laser was set at $(\Omega_{\text{recyc}}, \Delta_{\text{recyc}})/(2\pi) \approx (10, -20)$ MHz. The dots mark the experimental data. The solid lines show simulations of the excitation spectrum using the experimental parameters: the simulation plotted with a red line neglects the motion of the ion, while the black line represents a simulation where a phonon occupation number $\langle n_{\text{phn}} \rangle = 90$ for the secular motional modes of the ion was assumed. The values for the Rabi frequencies and detunings were obtained from independent measurements.

5.6 Photon statistics

The experimental setup employs single-photon counting avalanche photodiodes that issue short electric pulses upon the detection of a photon. The fact that such pulses are well-defined in time enables the measurement of time-resolved second-order correlations.

The *unnormalised* intensity correlation function $G^{(2)}(\tau)$ of a light source reveals information on the photon statistics and can be estimated from the cumulative measurement of the photoelectric detections. For a light source with intensity $I(t)$, it is given by the following time average:

$$G^{(2)}(\tau) = \langle I(t+\tau)I(t)\rangle = \frac{1}{T}\int_0^T I(t+\tau)I(t)dt \tag{5.4}$$

Upon the detection of one photon, the detector is inactive for a certain period of time, known as *dead time*. To prevent the loss of information of short delay times τ, the problem is circumvented by splitting the light under study between two detectors. The photon arrival times at both detectors are recorded over a large time T, ranging from minutes to several hours, and the cross-correlation of the detection coincidences is obtained. This information can be used to build an histogram of correlations $H(t_k)$, which can be used to estimate the unnormalised intensity correlation function $G^{(2)}(\tau)$.

The intensities $I_{1,2}(t)$ at the two detectors are proportional to the count rates $r_{1,2}(t)$ of the photoelectric detections: $r_{1,2}(t) = (\eta/(\hbar\omega))I_{1,2}(t) = (\eta/(2\hbar\omega))I(t)$. The cross-correlation function of the detection coincidences $H(\tau)$ is therefore proportional to the unnormalised intensity correlation function $G^{(2)}(\tau)$:

$$H(\tau) = \int_0^T r_2(t+\tau)r_1(t)dt \tag{5.5}$$

$$= \langle I_2(t+\tau)I_1(t)\rangle \cdot T \cdot \left(\frac{\hbar\omega}{\eta}\right)^2 = G^{(2)}(\tau)\cdot T\cdot\left(\frac{2\hbar\omega}{\eta}\right)^2 \tag{5.6}$$

where $\hbar\omega$ is the energy of one photon and η is the quantum efficiency of the detectors.

The *normalised* intensity correlation function $g^{(2)}(\tau)$ can therefore be obtained from

$$g^{(2)}(\tau) = \frac{\langle r_2(t+\tau)r_1(t)\rangle}{\langle r_1(t)\rangle\cdot\langle r_2(t+\tau)\rangle} = \frac{H(\tau)}{\bar{r}_1\cdot\bar{r}_2}\cdot\frac{1}{T} \tag{5.7}$$

where $\bar{r}_{1,2} = \langle r_{1,2}(t)\rangle$ are the average count rates at the two detectors.

5.6.1 Estimation of the intensity correlation function from a correlation histogram

In our experiments, the photoelectric detection events at the two detectors are recorded with a finite temporal resolution of $t_{\text{res}} = 4$ ps. It is therefore possible to build two lists, $(a_1, a_2, \ldots, a_n)$ and $(b_1, b_2, \ldots, b_n)$, where the k-th entry is either 1 or 0, depending on the detection of a photon during the time interval $[k\cdot t_{\text{res}}, (k+1)\cdot t_{\text{res}}[$ in the corresponding detector.

Although the cross-correlation $H(\tau)$ is a continuous function, it can be approximated by a histogram $H(t_k;t_{\text{res}})$ obtained from the convolution of the two lists of photoelectric detections [86]:

$$H(\tau)\approx H(t_k;t_{\text{res}})=\sum_n a_n b_{n+k} \tag{5.8}$$

where $\tau = t_k = kt_{\text{res}}$ is the central time associated with the k-th bin and each bin comprises a temporal width t_{res}.

However, it is often the case that the data is further binned into a more meaningful time base Δt_{bin}. The resulting histogram of correlations $H(t_k;\Delta t_{\text{bin}})$ is simply

$$H(t_k;\Delta t_{\text{bin}})=\sum_{m=-\Delta t_{\text{bin}}/(2t_{\text{res}})}^{\Delta t_{\text{bin}}/(2t_{\text{res}})} H(t_k;t_{\text{res}})=\sum_{m=-\Delta t_{\text{bin}}/(2t_{\text{res}})}^{\Delta t_{\text{bin}}/(2t_{\text{res}})}\sum_n a_n b_{n+k+m} \tag{5.9}$$

and corresponds to the integration of the cross-correlation function $H(\tau)$ over a binning time Δt_{bin}:

$$H(t_k;\Delta t_{\text{bin}})=\int_{t_k-\Delta t_{\text{bin}}/2}^{t_k+\Delta t_{\text{bin}}/2} H(\tau)d\tau\approx H(\tau=t_k)\cdot\Delta t_{\text{bin}} \tag{5.10}$$

Here, Δt_{bin} is assumed to be sufficiently small compared to the time scale of the dynamics of the light source. The normalised intensity correlation function $g^{(2)}(\tau)$ can therefore be estimated from the correlation histogram $H(t_k;\Delta t_{\text{bin}})$ as

$$g^{(2)}(\tau=t_k)=\frac{H(t_k;\Delta t_{\text{bin}})}{\bar{r}_1\cdot\bar{r}_2}\cdot\frac{1}{T\cdot\Delta t_{\text{bin}}} \tag{5.11}$$

In the experiments, the correlation histogram $H(t_k,\Delta t_{\text{bin}})$ is obtained using a different (but equivalent) algorithm. The photodetection times at the two detectors is directly available as two time ordered lists. Rather than building the two lists a_k and b_k by placing 0 or 1 on each entry and *then* convolve the two lists, the histogram $H(t_k,\Delta t_{\text{bin}})$ can be built by binning all the time differences between the events on one list and the events on the other list. The latter method has the advantage of being friendlier with the computational resources.

It is interesting to note that for detections totalling N_1 and N_2 events at the two detectors, the histogram contains a total of $\sum_k H(t_k;\Delta t_{\text{bin}})=N_1N_2$ correlations. In contrast, in the traditional "start-stop" technique, a photon detection on one detector triggers one timer while the detection of a second photon on the second detector stops the timer, which leads to a much lower total of $\sum_k H(t_k;\Delta t_{\text{bin}})=\min\{N_1,N_2\}$ such correlations. By time-tagging the photoelectric detections it is possible to make a better use of the acquired information than with the traditional "start-stop" technique.

5.6.2 APD flashes

The absorption of one single photon in any of our APDs triggers an electron avalanche that is then detected. In the course of the recombination processes that follow, a broadband flash of light (700 – 900 nm) is emitted by the semiconductor [87].

In the early stages of the experiments, this caused the correlation histogram to show two narrow peaks (FWHM 3 ns), at time delays of $\tau = 4$ ns and of $\tau = 125$ ns.

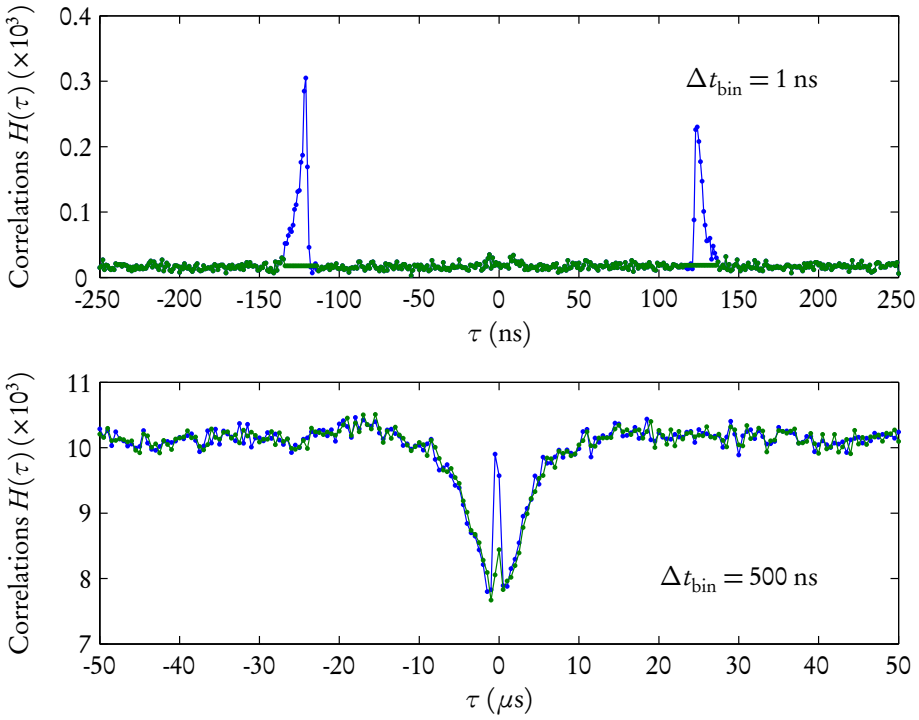

Figure 5.12: Histogram of the two-channel coincidences for different delay times τ and for two binning times Δt_{bin}. With a binning time $\Delta t_{\text{bin}} = 1$ ns, two sharp peaks at $|\tau| = 125$ ns are visible (top plot, blue line). These are caused by the flashes of light emitted by the APD upon a photoelectric detection. The green line on the top plot shows the post-processed histogram. The bottom plot shows the raw and post-processed binned in 500 ns intervals.

The first peak corresponds to the time required by one flash of light to propagate from the detector to the collimator of the fibre coupler inside the Hanbury-Brown and Twiss setup, be partially reflected and propagate to the other detector. The second (larger) peak is associated with light that couples to the multi-mode fibre, propagates to the cavity and is reflected back, finally reaching the other detector. The peak at 4 ns could be virtually eliminated by placing apertures in front of the detectors and close to the beam splitter. The second peak could not be completely eliminated, but its amplitude could be drastically reduced. It is then removed during the post-processing of the data, as described below.

From the data, we first obtain a histogram of the time interval between any two detections by considering a binning time of 1 ns, which is a time scale well below any of the relevant physical processes of the system. The values of bins corresponding to the spurious peak caused by the APD flashes are then replaced by the average values of the first 12 bins in the vicinity of the peak region. The resulting correlation histogram is then typically re-binned using a considerably larger bin size ($\Delta t_{\text{bin}} = 500$ ns). Figure 5.12 compares the correlation histograms obtained using raw and post-processed data: for a final binning size of $\Delta t_{\text{bin}} = 500$ ns, the effects of the APD flashes are entirely contained in one bin.

This experimental imperfection can be potentially eliminated by replacing the multi-mode fibre with a single-mode fibre, and eventually using more selective optical filters.

5.6.3 Background subtraction

The photoelectric detections at the avalanche photodiodes used for single-photon counting at 866 nm can be triggered not only by light emitted by the ion (signal), but also by other sources, which leads to the presence of noise.

Such noisy sources include mainly unfiltered light at 785 nm from the trap cavity lock, but also residual broadband ambient light, light at 866 nm scattered from the trap electrodes and the dark counts in the detectors. The noise introduces a background in the detection rates of the two detectors. By performing experiments in which there was no ion in the trap, we have established that the background noise is constant over an experimental run and is characterised by a flat intensity correlation function.

A periodic determination of the background levels of each detector allows for the correction of the experimental results. This is performed by blocking the laser at 397 nm: the ion remains in the fundamental state $S_{1/2}$ and the measurement of the count rate of the detectors is sufficient to determine the background.

Assuming the photons emitted by the ion into the cavity mode are detected at rates $s_{1,2}(t)$ at detectors 1,2 and background noise is detected at rates $b_{1,2}(t)$ (with $r_{1,2}(t) = s_{1,2}(t) + b_{1,2}(t)$), the histogram $H(t_k;\Delta t_{\text{bin}})$ obtained from the coincidence measurements is an estimation of the following correlation function:

$$H(t_k;\Delta t_{\text{bin}}) = T \cdot \int_{t_k-\Delta t_{\text{bin}}/2}^{t_k+\Delta t_{\text{bin}}/2} \langle [s_1(t+\tau)+b_1(t+\tau)][s_2(t)+b_2(t)]\rangle d\tau \qquad (5.12)$$

where T is the total acquisition time. If the noise follows a Poissonian distribution, the time dependence can be dropped, that is, $b_{1,2}(t) = b_{1,2}$. The contribution of the background-background correlations was measured by recording the coincidences in the absence of an ion in the trap and was confirmed to be flat, as in the Poissonian case. Accepting the assumption of Poissonian background, equation (5.12) simplifies to

$$H(t_k;\Delta t_{\text{bin}}) = T \cdot \int_{t_k-\Delta t_{\text{bin}}/2}^{t_k+\Delta t_{\text{bin}}/2} \langle s_1(t+\tau)s_2(t)\rangle d\tau + (b_1\bar{s}_2 + \bar{s}_1 b_2 + b_1 b_2)\cdot\Delta t_{\text{bin}}\cdot T \qquad (5.13)$$

where we have introduced the average count rates at the two detectors $\bar{s}_{1,2} = \langle s_{1,2}(t)\rangle$. The first term is proportional to the second-order intensity correlation function $G^{(2)}(\tau)$. The second and third terms describe the accidental background-signal correlations, whereas the last term accounts for the two-channel background-background correlations.

By recalling that the normalised intensity correlation function $g^{(2)}$ is effectively given by

$$g^{(2)}(\tau) = \frac{\langle s_1(t+\tau)s_2(t)\rangle}{\bar{s}_1\bar{s}_2} \qquad (5.14)$$

it becomes clear that for sufficiently small binning times, it can be estimated as fol-

lows:

$$g^{(2)}(\tau = t_k) \approx \frac{\int_{t_k-\Delta t_{\text{bin}}/2}^{t_k+\Delta t_{\text{bin}}/2} \langle s_1(t+\tau)s_2(t)\rangle \, d\tau}{\bar{s}_1\bar{s}_2 \cdot \Delta t_{\text{bin}}} \tag{5.15}$$

$$\approx \frac{H(t_k;\Delta t_{\text{bin}})}{\bar{s}_1\bar{s}_2 \cdot T \cdot \Delta t_{\text{bin}}} - \frac{b_1\bar{s}_2 + \bar{s}_1 b_2 + b_1 b_2}{\bar{s}_1\bar{s}_2} \tag{5.16}$$

In the laboratory environment, it is often simpler to normalise the histogram $H(t_k;\Delta t_{\text{bin}})$ first, and then subtract the background to obtain the correlation functions. Following the argumentation leading to (5.11), the normalised histogram of correlations $h(t_k;\Delta t_{\text{bin}})$ is given by:

$$h(t_k;\Delta t_{\text{bin}}) = \frac{H(t_k;\Delta t_{\text{bin}})}{\bar{r}_1 \cdot \bar{r}_2} \cdot \frac{1}{T \cdot \Delta t_{\text{bin}}} \tag{5.17}$$

From $\bar{r}_{1,2} = \bar{s}_{1,2} - b_{1,2}$, we can estimate the normalised second-order correlation function using

$$g^{(2)}(\tau = t_k) = \frac{h(t_k;\Delta t_{\text{bin}}) - 1}{\left(1 - \bar{b}_1/\bar{r}_1\right) \cdot \left(1 - \bar{b}_2/\bar{r}_2\right)} + 1 \tag{5.18}$$

Chapter 6

Deterministic single-photon source

In this chapter we discuss the results of an implementation of a single-photon source, based on the excitation of a vacuum-stimulated Raman transition with laser pulses. The results are preliminary, in the sense that not all technical problems have been solved yet, namely regarding background and laser linewidth. After briefly reviewing the literature, we provide details on the pulse sequence and present the measurement of second-order correlation functions. The experimental results agree very well with the results of the numerical simulations using the model described in chapter 3. This confirms the validity of both the calibration procedure and the characterisation of the experimental setup. We complement the discussion by comparing our preliminary results to other results found in the literature.

6.1 Introduction

The deterministic generation of single photons in a well-defined spatial and spectral mode of the radiation field represents the ultimate control of the light emission process. Many applications in the field of quantum information science [15, 88] such as quantum cryptography or linear optical quantum computing [89] require a deterministic source of single photons.

An ideal single-photon source should output single photons at a high repetition rate into a single mode of the radiation field with unit efficiency. It should also allow for on-demand action, that is, it should be triggerable without delay.

Most of the proposed and/or demonstrated schemes for single-photon generation rely on the spontaneous decay of an excited emitter, but the inherent disadvantage of spatial and spectral uncertainties constitute a shortcoming. Such triggered single-photon emitters have been realised in diverse systems, including atoms or ions [90, 91], molecules [92, 93], quantum well p-i-n hetero-junctions [94], colour centres [95, 96] and semiconductor quantum dots [97, 98].

However, there have been proposals [29, 30, 99] and experiments that make use of stimulated processes on neutral atoms or ions. They are generally associated with high single-photon generation efficiencies [90, 91, 100]. The schemes based on stimulated transitions in single atoms coupled to a cavity mode offer the advantage of photon emission into a single spatial and spectral mode of the radiation field [29, 30, 99–

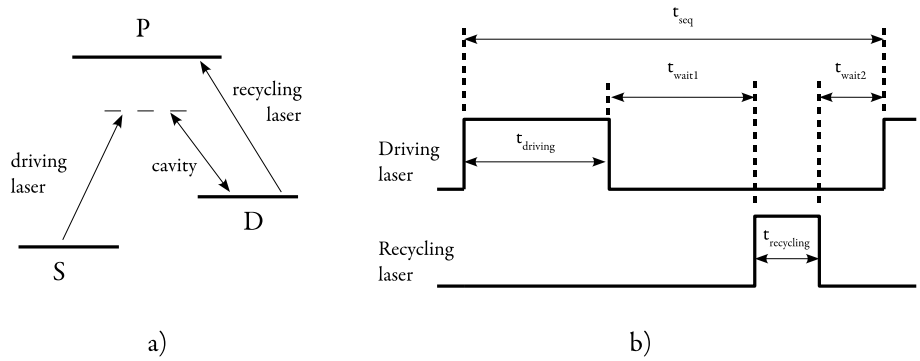

Figure 6.1: Experimental configuration for the single-photon source (a) and timing of the pulse sequence (b). The ion is alternately excited with square light pulses of the driving and recycling lasers. By pulsing the driving laser, the vacuum-stimulated Raman transition is excited, the population in S is transferred to D and a photon is emitted into the cavity. After a waiting time t_{wait1}, the recycling laser is pulsed and the atomic population in D is reset in S.

102]. Such schemes are good candidates for the implementation of proposals like atom-photon entanglement [102, 103], which is a fundamental resource for quantum state transfer [24, 104], for the realisation of quantum networks and for quantum information processing [88].

6.2 Implementation

Our implementation of a single-photon source operates on the vacuum-stimulated Raman transition (see section 5.5) and employs a sequence in which the pulsed excitation of driving and recycling lasers is alternated (Figure 6.1). The single-photon source relies on the fact that at most one photon can be emitted into the cavity mode while the driving laser is exciting the single-ion device. Unlike the schemes based on adiabatic passages, no particular pulse shape is required [31, 76].

Following the setup described in section 5.5, the driving laser is set up in π configuration and detuned by ≈ 400 MHz from the $S_{1/2} \leftrightarrow P_{1/2}$ transition, while the recycling laser is set near-resonant. The cavity detuning is set to fulfill the Raman condition with the driving laser and the ion is prepared in the $|S,0\rangle$ state. By switching on a first driving pulse of duration t_{driving}, the population in $|S,0\rangle$ is transferred via the vacuum-stimulated Raman interaction to the state $|D,1\rangle$, at a rate $\Omega_{\text{eff}} = g\Omega_{\text{driv}}/(2\Delta)$: one photon is emitted into the cavity mode while the ion is transferred to the D manifold. The light pulse has a rectangular temporal profile and is obtained by switching the radiofrequency drive of the appropriate acousto-optical modulator. A waiting time of duration t_{wait1} follows, in which the lasers are blocked, thus allowing the photon to exit the resonator through the output-coupling mirror. The detection of the photon projects the ion-cavity system in the state $|D,0\rangle$. The ion is then excited with the recycling laser for a period $t_{\text{recycling}}$: the population in $|D,0\rangle$ is excited to the state $|P,0\rangle$, which eventually decays via spontaneous emission to the initial state $|S,0\rangle$.

As the sequence is repeated, the photon detection times at the two detectors are recorded. The analysis of the experimental results is based on the statistical properties of the photon stream, namely the intensity correlation function, $g^{(2)}(\tau)$ (see sections 2.3 and 5.6).

In order to ensure there is no time overlap between driving and recycling pulses due to any experimental imperfections, an extra waiting time of duration t_{wait2} is introduced before the sequence is repeated. The total duration of the sequence is therefore $t_{\text{seq}} = t_{\text{driving}} + t_{\text{wait1}} + t_{\text{recycling}} + t_{\text{wait2}}$.

6.3 Results

The results on the single-photon source presented in this section are also discussed by Andreas Stute in his Diploma thesis [81].

We have evaluated the statistical properties of the single-photon source in the form of intensity correlations for different sequences. As an example, Figure 6.2 shows the intensity correlations normalised to the mean intensity, for two sequences consisting of two distinct waiting times t_{wait1}, but for constant driving and recycling pulse lengths. The peak separation corresponds to the sequence duration, with the peak at $\tau = 0$ being absent, signalling the single-photon nature of our source. The spurious peaks caused by the APD flashes (see section 5.6.2) were removed and the background was subtracted (see section 5.6.3). The solid red line is the result of a simulation (see chapter 3) using the calibrated experimental parameters and agrees very well with the experimental results, which highlights the full understanding of the dynamics of the system.

The single-photon source is however limited by a relatively large background. For both measurements in Figure 6.2, the light at 785 nm used for stabilising the cavity length is not perfectly blocked and contributes with a Poissonian background of $622\,\text{s}^{-1}$. Additionally, the dark count rate from the avalanche photodiodes is $\approx 100\,\text{s}^{-1}$. In contrast, the average detection count rate of photons emitted by cavity was $813\,\text{s}^{-1}$ for the top measurement and $337\,\text{s}^{-1}$ for the bottom measurement, resulting in a signal-to-noise ratio of 1.1 and 0.5, respectively.

By operating the single-ion device as a single photon source, it is possible to obtain more information from the system, namely regarding the efficiency of the single-photon generation process. Nevertheless, the poor signal-to-noise ratio prevents us from giving a meaningful number for the probability of simultaneously emitting more than one photon.

Once the background has been subtracted, the *overall probability for a successful detection* (p_{succ}) can be estimated from the ratio between the number of photoelectric detections relative to signal at the two detectors (S_1 and S_2, respectively) and the number of trials (N_{trials}).

$$p_{\text{succ}} = \frac{S_1 + S_2}{N_{\text{trials}}} \tag{6.1}$$

On the other hand, p_{succ} is the product of the *probability for the emission of a single photon into the cavity mode*, p_{em}, with the *probability that a photon in the cavity is eventually detected*, p_{det}:

$$p_{\text{succ}} = p_{\text{em}} \cdot p_{\text{det}} \tag{6.2}$$

As the latter (p_{det}) can be independently measured (see section 4.7.2), it is possible

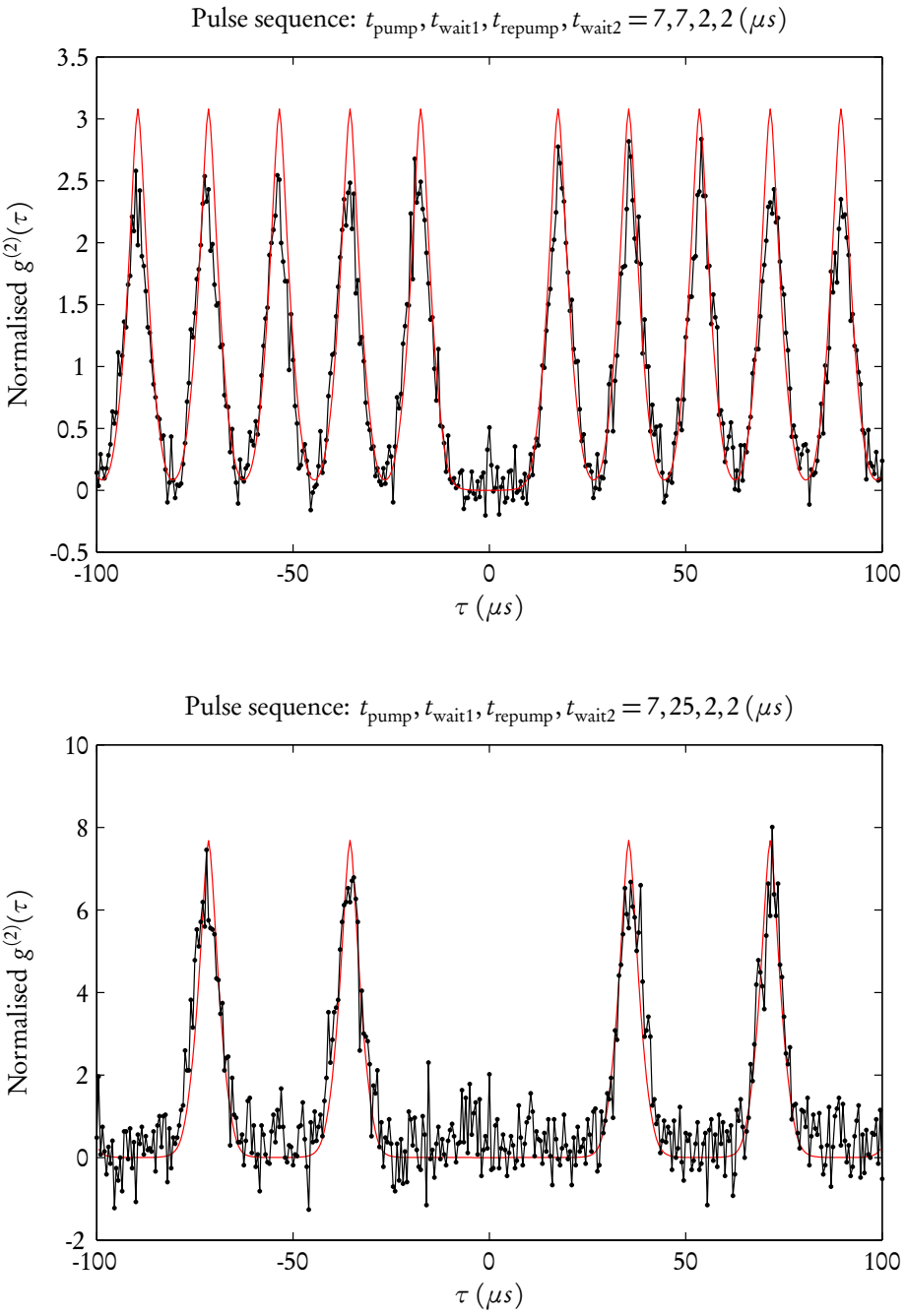

Figure 6.2: Normalised intensity correlation of the single-photon source, for two different waiting times t_{wait1}, at driving Rabi frequency and detuning $(\Omega_{\text{driv}}, \Delta_{\text{driv}})/(2\pi) = (228, -384.6)$ MHz. Each bin comprises a time interval of 0.5 μs. The background has been subtracted, and the correlations have been normalised to the mean intensity over the measurement period (about 30 minutes). The solid red line is the result of a numerical simulation using independently measured experimental parameters.

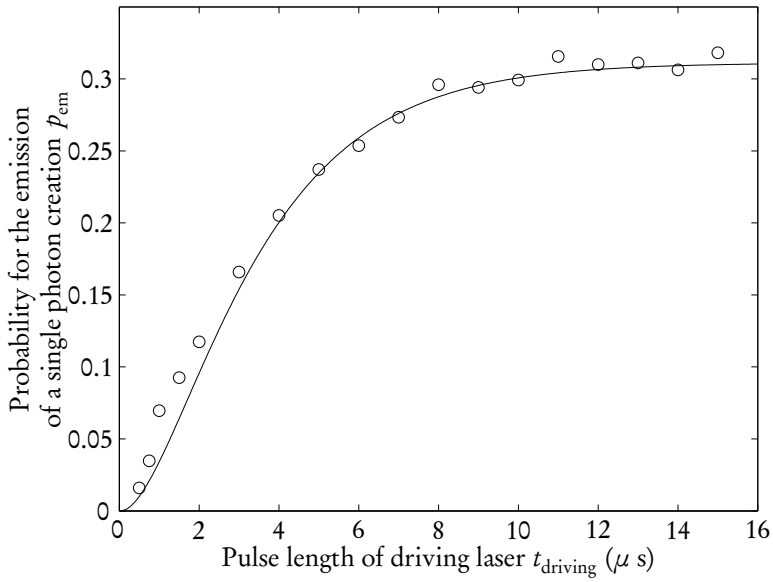

Figure 6.3: Measurement of the probability for the emission of a single photon into the cavity in one trial, p_{em}, as a function of the duration of the driving pulse $t_{driving}$, for fixed parameters $(t_{wait1}, t_{recycling}, t_{wait2}) = (7,2,2)$ μs and a driving Rabi frequency and detuning of $(\Omega_{driv}, \Delta_{driv})/(2\pi) = (228, -384.6)$ MHz. The experimental data is represented by the circles whereas the solid line is the result of a numerical simulation using independently measured experimental parameters. A maximum $p_{em} = 32\%$ was measured.

to determine the *probability for the emission of a single photon*, p_{em} :

$$p_{em} = \frac{p_{succ}}{p_{det}} = \frac{S_1 + S_2}{N_{trials} \cdot p_{det}} \tag{6.3}$$

Figure 6.3 shows the probability for the emission of a single photon into the cavity p_{em} as a function of the duration of the driving pulse $t_{driving}$, for fixed sequence parameters $(t_{wait1}, t_{recycling}, t_{wait2}) = (7,2,2)$ μs and at driving laser Rabi frequency and detuning of $(\Omega_{driv}, \Delta_{driv})/(2\pi) = (228, -384.6)$ MHz, as well as the results of a numerical simulation using the calibrated experimental parameters.

The probability for a single photon emission p_{em} increases monotonously with the length of the driving pulse $t_{driving}$, until saturation is reached at $t_{driving} \approx 12$ μs. The measurement shows that we have achieved a maximum probability of $p_{em} = 32\%$. One must note that for this intensity of the driving laser, the ion-cavity system is in an intermediate regime. Consequently, the photons are spontaneously emitted and Rabi oscillations are not observed. The Raman transition is broadened by dissipative processes that compete with the coherent excitation. The efficiency is in principle limited by the competition between the stimulated Raman process and the off-resonant excitation of the P state, which is followed by spontaneous decay into the manifolds D and S.

To better illustrate the dynamics of the competing processes, Figure 6.4 shows the various mechanisms present while driving the single-ion device. Their respective rates have already been introduced in section 2.2.3.

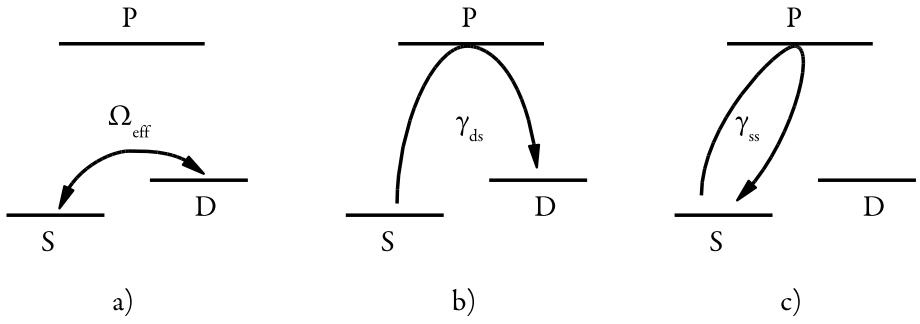

Figure 6.4: Processes present during the pulsed excitation of the system. The photons are emitted in the cavity following the excitation of the vacuum-stimulated Raman transition, represented in a). However, the driving laser can induce the off-resonant excitation of the P state, which is followed by spontaneous decay, to either the D or S states. The first case is depicted in b) and results in population loss from S at a rate γ_{ds}. The second case is sketched in c), and introduces phase noise at a rate γ_{ss}: the population in S remains constant albeit with a different phase.

In the process sketched in Figure 6.4b, the population in the $|S,0\rangle$ state is irreversibly transferred to $|D,0\rangle$. This final state is decoupled from the driving laser and the cavity mode is not populated. This incoherent process occurs at a rate given by γ_{ds} (see section 2.2):

$$\gamma_{ds} = \gamma_{s \rightsquigarrow p \rightsquigarrow d} \approx \left(\frac{\Omega_{\text{driv}}}{2\Delta_{\text{driv}}} \right)^2 \cdot \gamma_{dp} \tag{6.4}$$

The mechanism in Figure 6.4c, introduces phase noise into $|S,0\rangle$ via spontaneous scattering on the $S \leftrightarrow D$ transition, which increases the linewidth associated with the vacuum-stimulated Raman transition and effectively reduces the coherent coupling rate. This noise is introduced at a rate given by γ_{ss}:

$$\gamma_{ss} = \gamma_{s \rightsquigarrow p \rightsquigarrow s} \approx \left(\frac{\Omega_{\text{driv}}}{2\Delta_{\text{driv}}} \right)^2 \cdot \gamma_{sp} \tag{6.5}$$

It should be noted that the driving beam itself also contains phase noise, which is associated with its linewidth $\delta_{\text{driv}}/(2\pi) \approx 300$ kHz.

The total linewidth associated with the Raman transition (γ_{eff}) is therefore given by

$$\gamma_{\text{eff}} = \gamma_{ss} + \gamma_{ds} + \delta_{\text{driv}} \approx \left(\frac{\Omega_{\text{driv}}}{2\Delta_{\text{driv}}} \right)^2 \cdot \gamma_p + \delta_{\text{driv}} \tag{6.6}$$

where $\gamma_p = \gamma_{sp} + \gamma_{dp}$.

The coherent population transfer $|S,0\rangle \rightarrow |D,1\rangle$ at a rate Ω_{eff} competes with the incoherent processes. In principle, the single-photon emission process reaches unit efficiency if it is a coherent process, that is, if $\Omega_{\text{eff}} \gg \gamma_{\text{eff}}$.

To improve the coherence of the process, it is important to reduce the ratio $\Omega_{\text{driv}}/\Delta_{\text{driv}}$ and decrease the linewidth of the driving laser to below the cavity linewidth ($\varkappa/(2\pi) = 54$ kHz).

If the driving laser were a perfectly coherent light source, we would have $\delta_{\text{driv}} = 0$ and the probability for the emission of a single photon into the cavity could be improved solely by reducing the ratio $\Omega_{\text{driv}}/\Delta_{\text{driv}}$, which would suppress the off-resonant excitation of the P state at the cost of a smaller repetition rate. In the limit of very weak intensity of the driving laser, unit photon emission probability could be reached. In reality, this is not entirely correct due to the constant phase noise introduced by the non-zero linewidth of the driving laser, which partially frustrates the excitation of the Raman transition. Instead, there is an optimum ratio $\Omega_{\text{driv}}/\Delta_{\text{driv}}$ at which the photon emission into the cavity is maximum.

At the moment of the writing of this thesis, the laser system at 397 nm is under technical improvements, which will hopefully lead to a laser linewidth for the driving laser of $\delta_{\text{driv}}/(2\pi) \approx 30$ kHz.

With a reduced linewidth, preliminary simulations predict a probability for the emission of a single photon into the cavity up to $p_{\text{em}} = 57\%$, for $(\Omega_{\text{driv}}, \Delta_{\text{driv}})/(2\pi) = (70, -400)$ MHz.

6.4 Comparison with other experiments

The literature describes several single-photon sources that use atoms or ions as emitters. It is therefore interesting to compare the results from the different implementations. Table 6.1 summarises the relevant results of selected experiments, namely the repetition rate (f_{rep}), the probability for the emission of a single photon in one trial (p_{em}), the probability of detecting an emitted photon (p_{det}), the overall probability of successfully generating and detecting a photon in one attempt ($p_{\text{succ}} = p_{\text{em}} \cdot p_{\text{det}}$) and the overall average photon detection rate when the single-photon source is operating.

Experiment	f_{rep} (kHz)	p_{em}	p_{det}	p_{succ}	Photons/s
Grangier et al. [90]	5000	98.1%	0.6%	0.6%	9600
Monroe et al. [91]	8100	95%	0.06%	0.057%	4600
Rempe et al. [102]	100	9%	11%	0.9%	932
Walther et al. [101]	100	3%	4.6%	0.14%	137
Kimble et al. [100]	100	99%	2.4%	2.4%	2400
this work (now)	55	32%	5.6%	1.7%	935
this work (future)	55	60%	6.6%	4%	2200

Table 6.1: Comparison of the characteristic parameters for five different experiments using neutral atoms or ions. From left to right and for each case, the columns list the repetition rate (f_{rep}), the probability for the emission of a single photon in one trial (p_{em}), the probability of detecting an emitted photon (p_{det}), the overall probability of successfully detecting a photon in one attempt to generate one photon (p_{succ}) and the overall average photon detection rate when the single-photon source is operating.

The first two entries refer to experiments where the trapped atom was coherently excited and the spontaneously emitted photons were collected by good quality optics.

Grangier et al. [90] stored individual ^{87}Rb atoms in a tight optical tweezer for typical trapping times of 34 ms. They illuminated these atoms with short resonant pulses (4 ns longs) at a wavelength of 780.2 nm and collected the spontaneously emitted photons by using a high numerical aperture of 0.7. They triggered a

sequence consisting of 885 μs of cooling and 115 μs of pulsed excitation, which was repeated 100 times before a new atom was loaded. The efficiency on the excitation of the upper state could be as high 98.1%, consequently they were able to observe Rabi oscillations. However, the overall detection efficiency (p_{det}) was only 0.6%. The long-term performance of the single-photon source is mainly limited by the difficulty in storing the atoms due to heating. Consequently the photon emission rate varies over time: although they have achieved a peak photon detection rate of 29000 s^{-1}, the average count rate was 9600 s^{-1}.

Monroe et al. [91] used a Paul trap to store single $^{174}Yb^{+}$ ions. The $S_{1/2} \leftrightarrow P_{1/2}$ transition was excited with ultra-short laser pulses (2 ps long) at a wavelength of 369.5 nm. The sequence consisted on 10 μs of Doppler cooling followed by 40 μs of excitation and measurement. They showed that the emitted photons were indistinguishable. [105]. Unlike the previous case, the mean storage time of the ions in the trap was of several days.

The remaining entries on the table correspond to a second group of independent experiments where the coupling to a cavity was exploited.

Rempe et al. [102] have implemented a single-photon source based on a stimulated Raman adiabatic passage (STIRAP) [106], where neutral ^{85}Rb atoms were coupled to the vacuum field of a high-finesse optical cavity. The atoms could be stored inside the cavity for an average of $\approx$ 10 s, by using a transverse dipole trap in standing-wave configuration. The sequence consisted on ramping the intensity of a trigger pulse for 5 μs, followed by a waiting period of 1 μs and a period of 4 μs for cooling and recycling of the atomic population. A photon-generation probability of 9% was measured.

Walther et al. [101] used a similar STIRAP scheme on a single Ca^{+} trapped ion coupled to an optical cavity resonant to the $P_{1/2} \leftrightarrow D_{3/2}$ transition. The sequence started with 3 μs of Doppler cooling on the $S_{1/2} \leftrightarrow P_{1/2}$ transition, followed by state preparation in the $S_{1/2}$ manifold for 0.5 μs. Subsequently, the ion was pumped by using a pulse with predefined intensity profile of up to 6 μs of duration. The sequence was then repeated at a rate of 100 kHz. In their experiment, the probability for photon emission into the cavity mode was of only 3%. It was also shown that the temporal wave-packet of the output photons could be shaped by modulating the driving beam.

Kimble et al. [100] reported the deterministic generation of single photons with high efficiency ($p_{\mathrm{em}} \approx$ 100%) from single Cs atoms trapped inside a cavity. In their experiment, one atom could be trapped for about 0.14 s. The sequence consisted of pulsing two counter-propagating driving beams for 1 μs, followed by an unspecified waiting time, 5 μs of two counter-propagating recycling beams and another unspecified waiting time. At a repetition rate of 100 kHz, each atom produced an average of 1.4×10^4 photons. In 3% of all storage events, two atoms were trapped, leading to non-zero $g^{(2)}(0)$. Nevertheless, they achieved up to a 16-fold suppression of two-photon events relative to a Poissonian process.

Although the experiments in the first group could almost reach unit photon emission efficiency, the detection efficiency (p_{det}) was significantly smaller than for the

second group of experiments, where the coupling to a cavity ensured better photon collection.

The experiments in the second group differ basically in the photon emission efficiency, but share high detection efficiencies due to the coupling to a cavity mode. On the one hand, the experiments by Walther et al. and Rempe et al. employ adiabatic Raman passages that rely on the stability of a dark state, which can be harmed by fluctuating magnetic fields or by phase noise in the driving laser, thus reducing the photon emission efficiency. On the other hand, both Kimble et al. and this work explore the coherent coupling to a transition, but have different coupling strengths to the respective transitions: the mechanism behind the single-photon emission can only achieve unit photon emission efficiency in the strong coupling regime.

In fact, the experiments presented in this chapter were performed in an effective intermediate coupling regime. With an improved linewidth for the driving laser, it should be possible to approach a stronger coupling regime, which should in turn allow for higher photon emission efficiency. Such single-photon source could potentially provide the necessary tools to map the atomic state into a Fock state of the cavity field, or even enable the creation of ion-photon entanglement. The emitted photons could be easily coupled into optical fibres and propagate over long distances to other nodes containing identical ion-cavity systems.

Such characteristics highlight that this system is ideal for the implementation of an atom-photon interface for long-distance quantum communication and distributed quantum computing.

Chapter 7

Tunable photon statistics

In chapter 6, we have seen that by pulsing the driving and recycling lasers alternately, the photons were emitted into the cavity one at a time. The physics of the system was marked by two timescales of relevance:

1. the average dead time between the emission of two successive photons;

2. the average storage time for a photon in the cavity.

The fact that the dead time between two photon emissions was much larger than the cavity storage time prevented the formation of states involving two photons and thus ensured the device behaved as a single-photon source. In other words, the existence of a large dead time was the fundamental reason behind such particular photon statistics.

In this chapter, we proceed by changing the time between two photon emissions, while exciting the system continuously.

Under continuous excitation of both driving and recycling lasers, the atomic population follows the cycle $S_{1/2} \rightarrow D_{3/2} \rightarrow P_{1/2} \rightsquigarrow S_{1/2}$ and photons are continuously emitted into the cavity. On the one hand, the time required for a photon to be emitted into the cavity is set by the Rabi frequency of the driving beam. On the other hand, the dead time associated with the population residing in the D state before being reset in the S manifold is set by the intensity of the recycling beam.

We perform experiments in which the intensity of the driving beam is kept constant, while the intensity of the recycling beam is increased. Consequently, the probability for forming cavity states with two photons increases, which has dramatic consequences for the photon statistics: the system goes from a quantum, sub-Poissonian regime, dominated by single-photon emissions to a classical, super-Poissonian regime, marked by photon bunching. In other words, we can control the statistical properties of the light emitted by the single-ion device. The experimental results agree very well with the outcome of a set of numerical simulations using the model developed in chapter 3 and the calibrated experimental parameters, which highlights that the dynamics of the system is fully understood, qualitatively and quantitatively.

Hennrich et al. [107] have previously reported on tunable photon statistics emitted from a cavity interacting with an ensemble of atoms. The tunability was achieved by changing the mean number of trapped atoms. While the photoelectric detections originating from the same atom contributed with sub-Poissonian statistics, the coincident photons from different atoms contributed with super-Poissonian statistics.

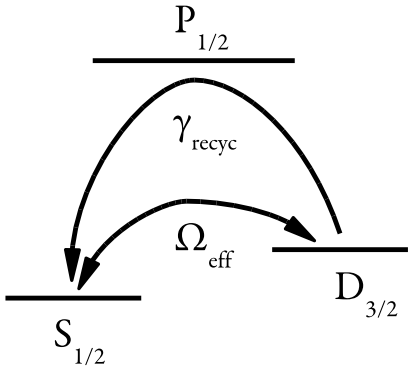

Figure 7.1: Simplified picture for the system under continuous excitation. On the one hand, the Raman interaction transfers population from the $S_{1/2}$ manifold to the $D_{3/2}$ state, populating the cavity with photons at a rate Ω_{eff}. On the other hand, the recycling beam resets the population in the the $S_{1/2}$ state at a rate γ_{recyc}, by excitation of the $P_{1/2}$ manifold, which is followed by spontaneous emission.

However, in contrast to our results, the observed photon statistics was always super-Poissonian.

7.1 Introduction

The photons are emitted into the cavity by exciting the vacuum-stimulated Raman transition $|S,0\rangle \leftrightarrow |D,1\rangle$ at a rate given by the Raman-Rabi frequency $\Omega_{\text{eff}} = g\Omega_{\text{driv}}/(2\Delta)$ (see chapter 6). In the absence of the recycling beam, only Fock states with zero and one intra-cavity photons can be occupied.

As the recycling laser becomes available, the population in $D_{3/2}$ is transferred to $P_{1/2}$. Within a very short time (7 ns), this population decays spontaneously to either $S_{1/2}$ or back to $D_{3/2}$ (see Figure 7.1). At steady state, the population in the $P_{1/2}$ manifold is very small. This fact can be used to simplify the theoretical description: the $P_{1/2}$ state can be factored out and the system can be characterised solely in terms of the $S_{1/2}$ and $D_{3/2}$ manifolds and the cavity Fock states (see section 2.2).

The process is effectively characterised by the population transfer $|D,n\rangle \rightsquigarrow |S,n\rangle$ implementing the *recycling mechanism* at a rate γ_{recyc} which is approximately given by:

$$\gamma_{\text{recyc}} \approx \frac{\Omega_{\text{recyc}}^2/4}{\Delta_{\text{recyc}}^2 + \gamma_p^2 + \Omega_{\text{recyc}}^2/2} \cdot \gamma_{sp} \tag{7.1}$$

where we recall that Ω_{recyc} and Δ_{recyc} are the Rabi frequency and detuning of the recycling beam, $2\gamma_{sp}$ and $2\gamma_{dp}$ are the spontaneous emission rates from the excited state P to S and D, respectively, with $\gamma_p = \gamma_{sp} + \gamma_{dp}$.

The recycling laser introduces a second mechanism that is characterised by the transformation $|D,n\rangle \rightsquigarrow |D,n\rangle$: it leaves the total population in the D manifold invariant but introduces phase noise in the D state at a rate γ_{dd} :

$$\gamma_{dd} \approx \frac{\Omega_{\text{recyc}}^2/4}{\Delta_{\text{recyc}}^2 + \gamma_p^2 + \Omega_{\text{recyc}}^2/2} \cdot \gamma_{dp} \tag{7.2}$$

The recycling laser itself is not a perfectly coherent light source: it also contains phase noise, which is associated with its linewidth $\delta_{\text{recyc}}/(2\pi) \approx 200$ kHz.

The dissipative processes associated with the recycling laser lead to a broadening of the linewidth of the Raman transition, $\gamma_{\text{eff}} = \gamma_{\text{eff}}^{(\text{driv})} + \gamma_{\text{eff}}^{(\text{recyc})}$, where

$$\gamma_{\text{eff}}^{(\text{recyc})} = \gamma_{\text{recyc}} + \gamma_{dd} + \delta_{\text{recyc}} \tag{7.3}$$

and $\gamma_{\text{eff}}^{(\text{driv})}$ is given by (6.6).

The second-order correlation function of the single-ion device is determined by the distribution of the population amongst the Fock states of the cavity field, which is in turn given by the balance between driving, recycling and photon loss mechanisms. In other words, the dynamics is determined by the effective atom-cavity coherent coupling rate Ω_{eff}, the recycling rate γ_{recyc} and the cavity decay rate $2\varkappa$.

In the intermediate regime where $\Omega_{\text{eff}} \approx \gamma_{\text{eff}}$, the total time τ_{tot} required for a photon to be added to the cavity field and the atomic population to complete a cycle $|D,0\rangle \rightarrow |D,1\rangle$ is given by

$$\tau_{\text{tot}} = \frac{1}{\Omega_{\text{tot}}} \sim \frac{1}{\Omega_{\text{eff}}} + \frac{1}{\gamma_{\text{recyc}}} \tag{7.4}$$

The intensity correlation function is marked by the balance of the rates at which photons are created and lost, Ω_{tot} and $2\varkappa$, respectively:

- If $\Omega_{\text{tot}} \ll \varkappa$, the photons leave the cavity as they are created. Consequently, only the cavity Fock states $|0\rangle$ and $|1\rangle$ are populated and the photon statistics is sub-Poissonian.
- If $\Omega_{\text{tot}} \gg \varkappa$, the photons accumulate in the cavity as they are lost at a rate much slower than they are produced and higher cavity Fock states are allowed to be populated. The exact nature of the photon statistics will however depend on the phase relationship between the populations in the various Fock states. If dynamics is dominated by incoherent processes, such phase relationship is random and the photon statistics of the cavity field will resemble a thermal source.

The experimental setup allows for the control of Ω_{tot}, which is achieved by setting the intensities of the driving and recycling beams. While the former is mainly used to tune the Raman-Rabi frequency Ω_{eff}, the latter can be use to set the recycling rate γ_{recyc} and consequently Ω_{tot}.

7.2 Measurement of intensity correlations

The experiment was set up in the configuration described in section 5.5: the cavity and the driving laser were detuned by ≈ -400 MHz, while the recycling laser was set near-resonant. In a first stage, the experimental parameters were calibrated and independently measured (see sections 5.4 and 5.5). The second-order photon correlations were studied in a regime in which the ion-cavity system is operated in an intermediate coupling regime: $\Omega_{\text{eff}} \sim \gamma_{\text{eff}} \approx 2\pi \times 150$ kHz.

Figure 7.2 shows the measured results for the normalised intensity correlation function in three situations, where the Rabi frequency of the recycling beam is progressively increased: $\Omega_{\text{recyc}}/(2\pi) = (7, 12, 16)$ MHz. For each case, the red line shows the results of a numerical simulation using the values of the experimental parameters

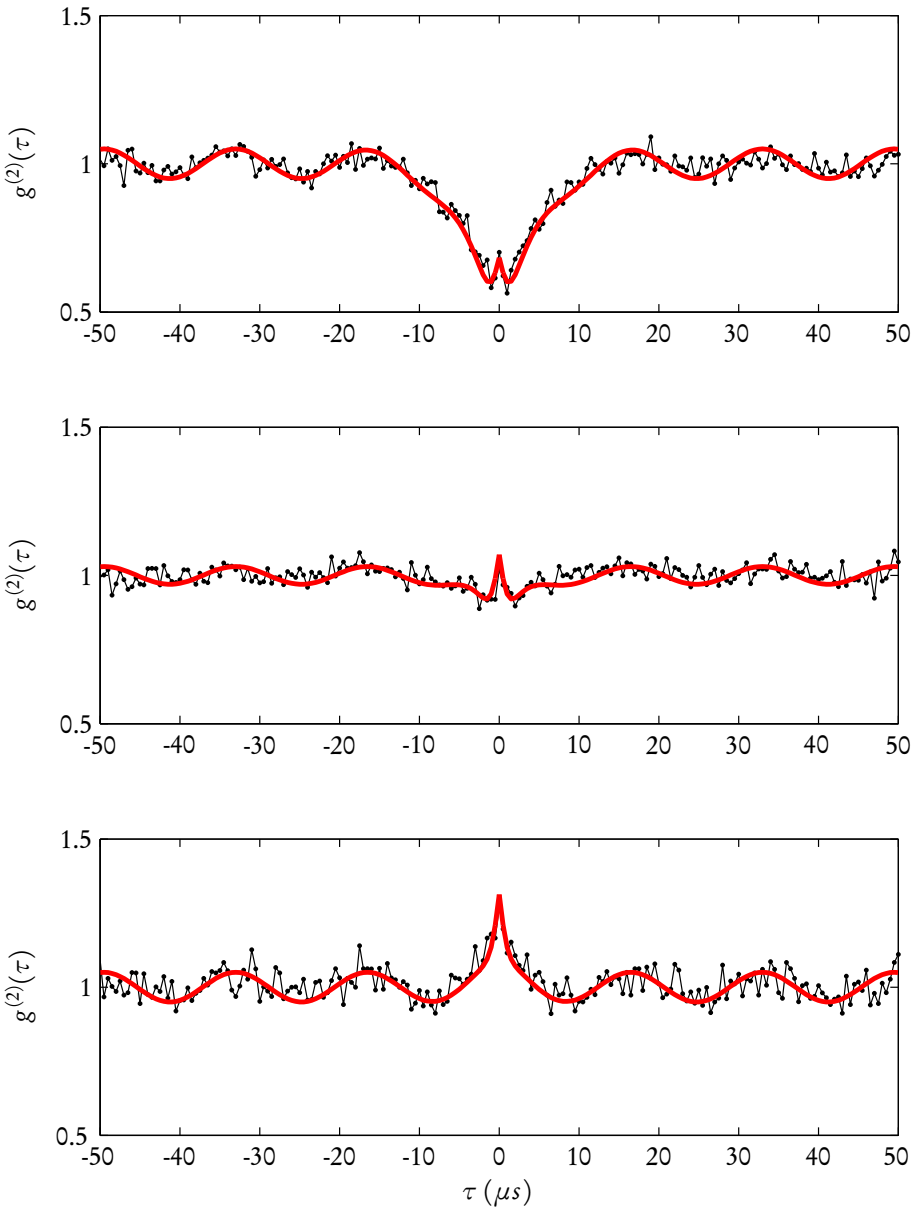

Figure 7.2: Experimental estimation of the normalised intensity correlation for a driving Rabi frequency of $\Omega_{\text{driv}}/(2\pi) = 95$ kHz, for three different recycling Rabi frequencies, namely $\Omega_{\text{recyc}}/(2\pi) = (7, 12, 16)$ MHz. The measurements are represented by the black dots. Accidental correlations with the background have been deducted, and the data was binned to a temporal resolution of 500 ns. The red lines are the result of numerical simulations using the independently measured experimental parameters. The top case (a) is obtained for the lowest intensity of the recycling beam and is characterised by sub-Poissonian statistics ($g^{(2)}(0) < 1$). This is in marked contrast with the bottom case (c), obtained for a higher intensity of the recycling beam, for which the photon statistics is super-Poissonian ($g^{(2)}(0) > 1$). The middle plot (b) is an intermediate case, where the photon statistics nearly coincides with the Poissonian case. The correlations shown here are modulated by the residual motion of the ion in the trap: the sinusoidal modulation corresponds to the beat of the two radial motional eigenfrequencies at ≈ 61 kHz.

obtained during the calibration stage of the experiment. Globally, as the total cycling rate Ω_{tot} of the Raman transition is increased, the intensity correlation functions are marked by the growth of a peak at short delay times $\tau \approx 0$ μs, resulting from the fact that Fock states with more than one cavity photon become populated.

In Figure 7.2a), the total cycling rate was set small: $\Omega_{tot}/(2\pi) \approx 95$ kHz. The photon statistics is clearly sub-Poissonian, with a negative Mandel-Q parameter of $-1.2(1)$ %, because the slow recycling process is limiting the emission of photons into the cavity [108, 109] and the cavity stores the photons for a limited (and shorter) period of time. The single-ion device is operated in a regime of single-photon emissions.

The two different timescales associated with the cavity storage time and with the photon emission process are set by the rates $\varkappa$ and Ω_{tot}, respectively, as can be observed in Figure 7.2a):

- The peak of the $g^{(2)}$-function for $|\tau| < 1.5$ μs reveals the fact that the cavity stores photons for a characteristic time $\tau_c = 1/(2\varkappa)$.
- For time delays $1.5 \lesssim \tau \lesssim 15$ μs, the $g^{(2)}$-function grows slowly until unity is reached. This longer timescale is associated with the increasing probability of emitting one photon into the cavity mode, which is in turn set by the total cycling time τ_{tot}.

For even longer delay times τ, a modulation of the correlation function is observed. This is attributed to the beat note between the ion's two quasi-degenerate radial modes of motion in the trap. The motion of the ion projected along the cavity standing wave induces an intensity modulation [110]. The amplitude of the modulation depends on the extension of the ion's wavepacket. The fact that such modulation can be observed already means the localisation of the ion along the cavity axis is defined to below half a wavelength, that is, 433 nm. In fact, we recall that we infer a localisation of ≈ 82 nm from the contrast of the cavity output rate as a function of the position of the ion relative to the cavity (see section 5.5.3). In the experimental conditions of Figure 7.2, the secular motional frequencies along the trap axis and the radial directions are ≈ 1 MHz and ≈ 3 MHz, respectively. Due to manufacturing asymmetries, the secular frequencies of the two radial modes differ by ≈ 61 kHz. However, none of the secular frequencies can be observed in the spectrum of the cavity output. This is because the cavity stores photons for a characteristic time $\tau_c = (2\varkappa)^{-1}$ and effectively acts as a low-pass filter with cutoff frequency at $2\varkappa/(2\pi) = 108$ kHz. Consequently, only the frequency difference between the two radial modes can be actually observed [111].

In Figure 7.2b), the recycling rate is slightly increased, which also increases the total cycling rate $\Omega_{tot} \approx 125$ kHz. The photon flux remains almost constant ($n_{ss} \approx 0.04$), but the statistical properties of the emitted photons change dramatically: the second-order correlation function becomes almost flat (with $Q = 0.0(1)$ %), akin to a Poissonian source of light.

Figure 7.2c) shows the intensity correlation function at a higher cycling rate: $\Omega_{tot}/(2\pi) \approx 135$ kHz. The photon statistics of the cavity output resembles that of a thermal source and the Mandel parameter is $Q = +1.0(1)$ %.

The measured coincident photon correlations, $g^{(2)}(0)$, are in fact governed by the population of cavity Fock states with two photons, p_2, so that $g^{(2)}(0) \sim 2p_2/p_1^2$ where p_1 is the population of states with only one photon. The population p_2 is established through an interplay between the rate Ω_{tot} at which photons are added

to the cavity and the rate $2\varkappa$ at which the photons decay from the cavity. Table 7.1 shows the simulated populations of the Fock states with one and two photons, using the formalism developed in chapter 3. The experimentally estimated $g^{(2)}(0)$ compares well with $2p_2/p_1^2$, thus confirming the validity of the argument.

Figure	p_1	p_2	$2p_2/p_1^2$	$g^{(2)}_{\mathrm{exp}}(0)$
7.2a)	3.5×10^{-2}	4.1×10^{-4}	0.67	0.70
7.2b)	4.2×10^{-2}	9.7×10^{-4}	1.09	1.02
7.2c)	4.4×10^{-2}	13×10^{-4}	1.34	1.27

Table 7.1: Simulated populations of one- and two-photon Fock states. These leads to $g^{(2)}(0) \approx 2p_2/p_1^2$ which is compared to the experimentally observed $g^{(2)}_{\mathrm{exp}}(0)$.

In summary, the control of the intensity of the recycling laser in an intermediate-coupling regime allows the control of the population of photons in the cavity, which in turn sets the statistical properties of the light emitted by the single-ion device.

This flexibility could be used in the study of the properties of cascaded quantum systems [37]: the single-ion device could be used to drive another (target) quantum system, an obvious example being another trapped $^{40}Ca^{+}$ ion coupled to a cavity mode. It is reasonable to expect that the properties of the target system suffers modifications that depend on the statistical properties of the light emitted by the single-ion device.

Another interesting possibility would be the investigation of the consequences of the application of diverse feedback techniques, such as coupling into the cavity a fraction of its own output. It is not clear if such techniques could be used to further reduce the intensity fluctuations.

Chapter 8

Single-ion laser

The single-ion device is composed by the same building blocks as a laser: a gain medium (the ion), a pumping mechanism (the external laser excitation) and a feedback mechanism (the optical cavity).

In chapter 7, we have shown that the excitation of the single-ion device with an increasing intensity of the recycling beam allowed an increase of the rate at which the photons were spontaneously emitted into the cavity, which in turn had an effect on the photon statistics.

The natural question arises: if the single-ion device is subject to stronger excitation, will it ever reach a point where the cavity field is sufficiently large to allow stimulated emission of light? In other words, can the single-ion device behave as a laser?

In this chapter, we discuss measurements on our single-ion device in a regime that shows evidence of a laser threshold. The analysis shows that other characteristics of a "classical" conventional laser, such as linewidth narrowing and noise reduction can also be observed. The discussion is complemented with the results of a numerical simulation of the system for a wider set of experimental parameters, which show what are the accessible photon emission regimes.

8.1 Introduction

The first laser was demonstrated by Maiman et al. in 1960 [8]. The gain medium was a synthetic ruby crystal that was externally pumped by a flashlamp. Since then, lasers have become ubiquitous, being present in consumer electronics devices such as laser printers and optical storage devices, namely CD and DVD players. Lasers are widely used for fibre-optic communication and have become essential to telecommunication and entertainment industries. The interaction of high power laser radiation with biological tissue has also led to the development of medical and cosmetic techniques such as laser surgery and laser hair removal. The fact that high power lasers can deposit heat in a well-defined spot has been exploited in manufacturing processes, namely in cutting and welding metal. Laser technology is a very active field and is currently at the heart of research potentially leading to development of new technologies, such as inertial confined fusion.

A conventional laser is commonly associated with a macroscopic gain medium weakly coupled to an optical resonator and usually consists of a large number of

interacting atoms and photons. It is characterised by the existence of a threshold, which is reached when the rate at which photons are fed into the cavity mode exceeds losses [37, 50]. This is usually achieved through population inversion in the gain medium. At the same time, the linewidth of the emitted light is narrowed below the cavity linewidth. Above threshold, the laser intensity increases while intensity fluctuations are reduced with increasing pump power.

From a fundamental point of view, a laser employing a single atom as gain medium is a very attractive instrument to probe the description of lasers in the quantum regime, both theoretically and experimentally [32, 33, 49, 112–116].

The first experimental investigations in the optical regime using few atoms as a gain medium were performed in 1994 by An et al. [112]. They followed the same concept behind experiments on the one-atom maser [117], in the sense that they used a diluted beam of excited atoms traversing the cavity. If the atomic beam is sufficiently diluted, the atoms interact with the cavity one at a time, independent from each other. The cavity field results from the cumulative photon emissions from successive atoms.

However, a single atom coupled to the cavity field and in permanent interaction with the external pumping field is fundamentally different from the situation in which an inverted atom is injected into a cavity: upon the emission of a photon, the atom decouples from the cavity field and is unable to add another photon for a certain period of time. Consequently, the emitted light has characteristics that strongly deviate from standard laser properties, in particular regarding the question of the existence of a threshold.

On the one hand, it was shown theoretically that a single-ion laser can exhibit a threshold which corresponds to the region where the intensity fluctuations pass through a maximum while the output intensity is enhanced [33, 108].

On the other hand, such a threshold may not even exist: as the coupling to the cavity mode increases, the external pump power necessary to reach the threshold decreases. Moreover, depending on the pumping parameters, the system can be lasing without the population being inverted (as in the case of thresholdless lasers in the strong coupling regime) and the population can be inverted without the system showing any lasing action (as in the regime of self-quenching) [32, 33]. In the limit of very strong coupling, the laser threshold disappears and the photon statistics is sub-Poissonian, as experimentally demonstrated in 2003 by McKeever et al. [48, 49].

8.2 Overview

The tunability of the effective ion-cavity coupling of our single-ion device allows for the implementation of a single-ion laser in an intermediate coupling regime.

From chapters 2 and 7, we recall that the single-ion device can be approximated by an effective two-level system under external incoherent excitation. In this picture, it becomes clear that the incoherent pumping mechanism depends mainly on the recycling process, while the effective ion-cavity coupling is determined by the driving laser. Nevertheless, this picture is only valid as long as the recycling beam is set below saturation.

The experiments were pursued in a regime of a strong driving laser, in order to allow a large photon emission rate. The photon emission rate into the cavity generally follows the intensity of the recycling laser, provided the latter is set below saturation.

For lower recycling intensities (and consequently smaller photon emission rates) the photons are spontaneously emitted into the cavity mode: the coherence of the Raman transition is hindered by a lack of phase stability between the photons successively emitted into the cavity. The phase stability is limited by the width of the Raman transition, γ_{eff}, which results from the combination of cavity linewidth and broadening mechanisms introduced by both the driving and recycling lasers.

With increasing intensity of the recycling laser, the $D_{3/2} \leftrightarrow P_{1/2}$ transition approaches saturation and the rate of photon emission slows down, as it is not possible to quench the $D_{3/2}$ state any faster.

If the intensity of the recycling laser is increased beyond saturation, the states in the $P_{1/2}$ and $D_{3/2}$ manifolds suffer a pronounced dynamic Stark shift. The most notorious manifestation is the fact that the strong recycling beam introduces different light shifts to the various $D_{3/2} \leftrightarrow P_{1/2}$ Zeeman transitions and consequently modifies the spectrum of the vacuum-stimulated Raman transitions. Several Raman lines overlap and merge, effectively leading to an increase of the rate of photon emission into the cavity. Provided there is sufficient photon population in the cavity, this leads to an increase of stimulated emission into the cavity mode which can be perceived from the reduction of the intensity noise.

However, the increase in the photon emission rate cannot be maintained for a wide range of the intensity of the recycling laser: for excessive intensities, the $D_{3/2} \leftrightarrow P_{1/2}$ transition is dressed to the point that the recycling mechanism becomes inefficient. Consequently, the laser goes out.

It is reasonable to assume that there is one quantity that parametrises the behaviour of the single-ion device with respect to the photon emission into the cavity. The question arises: what would be the parameter for the smooth transition from a regime dominated by incoherent single-photon emission to a domain characterised by stimulated processes? We follow Boozer et al. [49] in the definition of the R parameter as the ratio of stimulated to spontaneous emission on the $P_{1/2} \leftrightarrow D_{3/2}$ transition:

$$R = \frac{2\varkappa \cdot \bar{n}}{2\gamma_{dp} \cdot \rho_{pp}} \tag{8.1}$$

If the off-resonant excitation of the $P_{1/2}$ state followed by spontaneous emission into free space dominates over the coherent Raman process, the photons are incoherently emitted into the cavity and the R parameter approaches 0. If the system behaves as a laser, in the sense that stimulated processes on the Raman transition are dominant, $R \gg 1$. We therefore loosely define $R \sim 1$ as the *threshold region*: the regime in which spontaneous and stimulated processes have a similar weight.

We follow Meyer et al. [33] in the identification of a lasing region in terms of measurable properties of the output light: a regime in which the intensity of the cavity output increases while the intensities fluctuations decrease. The former can be parametrised by the average intra-cavity photon number $\bar{n}$, while the latter can be quantified using Mandel's Q parameter (see section 2.3). Furthermore, we confirm through simulations that the linewidth of the emitted light is smaller than the cavity linewidth.

8.3 Experimental results

At a magnetic field of $B = 2.6$ G, and for a constant Rabi frequency of the driving beam of $\Omega_{\text{driv}}/(2\pi) = 220$ MHz, we recorded excitation spectra of the cavity output. Under these conditions, we have obtained a maximum average intracavity photon number at steady state of $\bar{n} \approx 0.1$, corresponding to a photon emission rate $2\varkappa \cdot \bar{n} \approx 6.8 \times 10^4\ \text{s}^{-1}$.

The cavity detuning was then set to fulfill the Raman condition ($\Delta_c/2\pi \approx -407$ MHz) and second order correlation functions were measured for different powers of the recycling laser.

From the data, we were able to extract both the average intra-cavity photon number at steady state $\bar{n}$ and Mandel's Q-parameter. The results are presented in Figure 8.1. We complete the discussion by including the results of the simulations on the R parameter, the spectral half width at half maximum of the light at the cavity output and the populations of the $S_{1/2}$, $P_{1/2}$ and $D_{3/2}$ manifolds (Figures 8.1b), 8.1c) and 8.1d), respectively). The parameters used in the simulations were obtained using the experimental parameters measured during the calibration stage.

We identify four different regimes for different ranges of the Rabi frequency of the recycling laser.

Region I: single-photon emitter

The first region (marked "I" in Figure 8.1) is characterised by slow recycling rates. The average intra cavity photon number is small and the photon statistics is sub-Poissonian: at $\Omega_{\text{recyc}}/(2\pi) \approx 10$ MHz, we measure $\bar{n} = 0.070(4)$ and $Q = -0.53(5)\%$.

The single-ion device is operated in a regime where it behaves as a single-photon emitter. The rise of the cavity photon number is due to the progressive inversion of population. As the cavity storage time is shorter than the average time between successive photon emissions, there are rarely two photons in the cavity. Akin to an atom under weak external excitation, the photons are spontaneously emitted into the cavity mode and the single-ion device exhibits non-classical output light.

One must note, however, that at the beginning of region I, an increase of the recycling rate enhances the intra-cavity mean photon number while intensity fluctuations are at the same time reduced (the Q-parameter decreases). This behaviour can in principle be the signature of a quantum laser without threshold for which stimulated emission into the cavity mode dominates [48, 49]. The conflict of interpretations can be clarified by using the R parameter defined above (Figure 8.1c)). We find that $R \approx 0.2$ in the region I of Figure 8.1, which clearly establishes that spontaneous emission is the dominant process. For a thresholdless quantum laser, one would have $R \gtrsim 1$ [48].

Region II: Build-up of cavity field

In region II, the intra-cavity photon number and the Q-parameter both increase as a function of the recycling rate. At the same time, population inversion is established.

As the recycling rate increases, the atomic population is inverted and the cavity photon number increases, mostly because the recycling process becomes increasingly efficient.

The slope $d\bar{n}/d\Omega_{\text{recyc}}$ (associated with the increase of the average intra-cavity photon number as a function of the Rabi frequency of the recycling beam) is at first

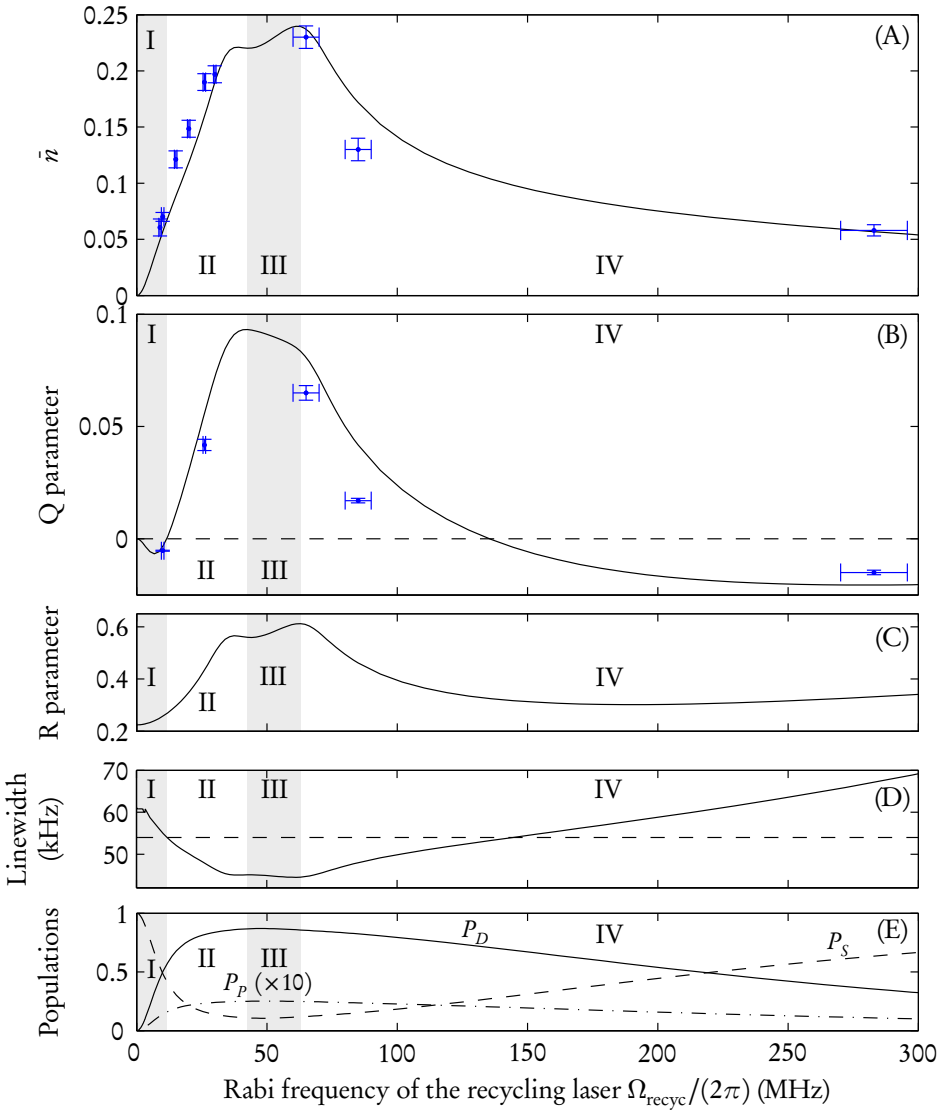

Figure 8.1: Measured and simulated results for a driving Rabi frequency of $\Omega_{driv}/(2\pi) = 220$ MHz, corresponding to a Raman-Rabi frequency of $\Omega_{eff}/(2\pi) = 95$ kHz, as a function of the Rabi frequency of the recycling laser. The blue points represent the experimentally measured data, while the lines represent simulated results using experimental parameters measured independently. A) average intra-cavity photon number at steady state. B) Mandel Q parameter. C) Simulation of the linewidth of the photon emission at the cavity output. D) Simulation of the population of the $S_{1/2}$, $P_{1/2}$ and $D_{3/2}$ manifolds at steady state (solid, dash-dotted and dashed lines, respectively). The population of the $P_{1/2}$ manifold is represented with a magnification factor of 10.

slightly smaller than in region I. In the end of region II, the $D_{3/2} \leftrightarrow P_{1/2}$ transition of the single-ion device approaches saturation and consequently the cavity photon number stagnates.

The statistics becomes super-Poissonian: the higher recycling rate implies that the time between two photon emissions reduces to below the cavity storage time. The photons are stored long enough to allow Fock states $n > 1$ to be populated. Nevertheless, the increase of the photon population in the cavity leads to a narrowing of the linewidth of the emitted light.

It must be noted that the R parameter and the rate of stimulated emission into the cavity increase as a consequence of the increase of photon emission into the cavity. However, at this stage, the rate of stimulated emission is not high enough to prevent the distribution of the photon population across the cavity Fock states to be anything else than a (super-Poissonian) thermal distribution.

In this regime, the single-ion device behaves classically and has a response (in terms of the intensity and its fluctuations) which is linear with the intensity of the recycling beam. This is the characteristic behaviour of a conventional laser below threshold.

Region III: Single-ion laser at threshold

In the third regime (region III in Figure 8.1), the average intracavity photon number $\bar{n}$ increases while the Q parameter has passed through a maximum. In other words, the cavity output intensity increases while intensity fluctuations are reduced. This is the signature of a laser threshold for the single-ion device [33].

To further corroborate this observation, note that in this region we derive a ratio $R \approx 0.6$ between stimulated and spontaneous emission of photons (Figure 8.1c) together with a linewidth narrowing below the cavity linewidth (Figure 8.1d). These are signatures of a semiclassical laser operating at threshold [64].

It is interesting to further discuss the mechanism behind the establishment of the threshold. As the Rabi frequency of the recycling beam is increased, the time gap between two photon emissions is reduced, but eventually the $P_{1/2} \leftrightarrow D_{3/2}$ transition is broadened by the laser field and the inversion of the atomic population reaches a maximum. A side-effect is that the various Zeeman $P_{1/2} \leftrightarrow D_{3/2}$ transitions are dressed by the laser field and suffer different dynamic Stark shifts. If the intensity of the recycling laser is further increased, these level shifts result in the merging vacuum-stimulated Raman transitions, which in turn lead to an increase in the photon emission rate and a reduction in the intensity fluctuations.

In the particular experimental conditions of our single-ion device, the recycling laser only excites σ transitions. Therefore, the resulting dressed eigenstates are mainly composed of two $D_{3/2}$ Zeeman sub-states and one $P_{1/2}$ sub-level. To clarify this point, we have performed numerical simulations where the cavity was removed entirely from the system. Figures 8.2 and 8.3 show respectively the eigenvalues and the decomposition of some of the corresponding eigenstates in terms of the bare atomic levels, as a function of the Rabi frequency of the recycling laser, for $(\Omega_{\text{driv}}, \Delta_{\text{driv}})/(2\pi) = (220, -400)$ MHz and $\Delta_{\text{recyc}}/(2\pi) = -20$ MHz, in the absence of a cavity field.

At very low intensities, the eigenstates coincide with the bare states. In particular, we identify the eigenstates $|C\rangle$ and D with $|D_{3/2}, m_d = +3/2\rangle$ and $|D_{3/2}, m_d = +1/2\rangle$, respectively. As the Rabi frequency of the recycling laser Ω_{recyc} increases, the atomic levels are dressed by the laser field and suffer different dynamic Stark shifts (see Figure

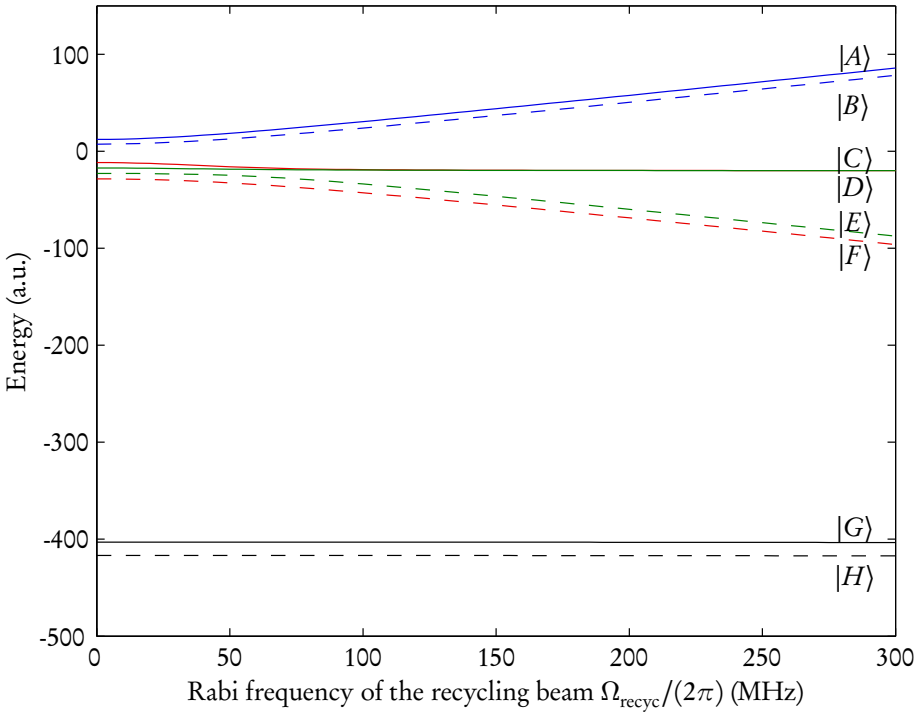

Figure 8.2: Energy associated with the atomic eigenstates ($|A\rangle$–$|H\rangle$) in the interaction picture as a function of the Rabi frequency of the recycling beam, Ω_{recyc}, for $(\Omega_{driv}, \Delta_{driv})/(2\pi) = (220, -400)$ MHz and $\Delta_{recyc}/(2\pi) = -20$ MHz. The eigenstates A–F result in a mixture of the various sublevels in the $P_{1/2}$ and $D_{3/2}$ manifolds, while the eigenstates $|G\rangle$ and $|H\rangle$ are reminiscent of the bare $|S_{1/2}, \pm 1/2\rangle$ levels. At high intensities, states $|C\rangle$ and $|D\rangle$ are nearly degenerate.

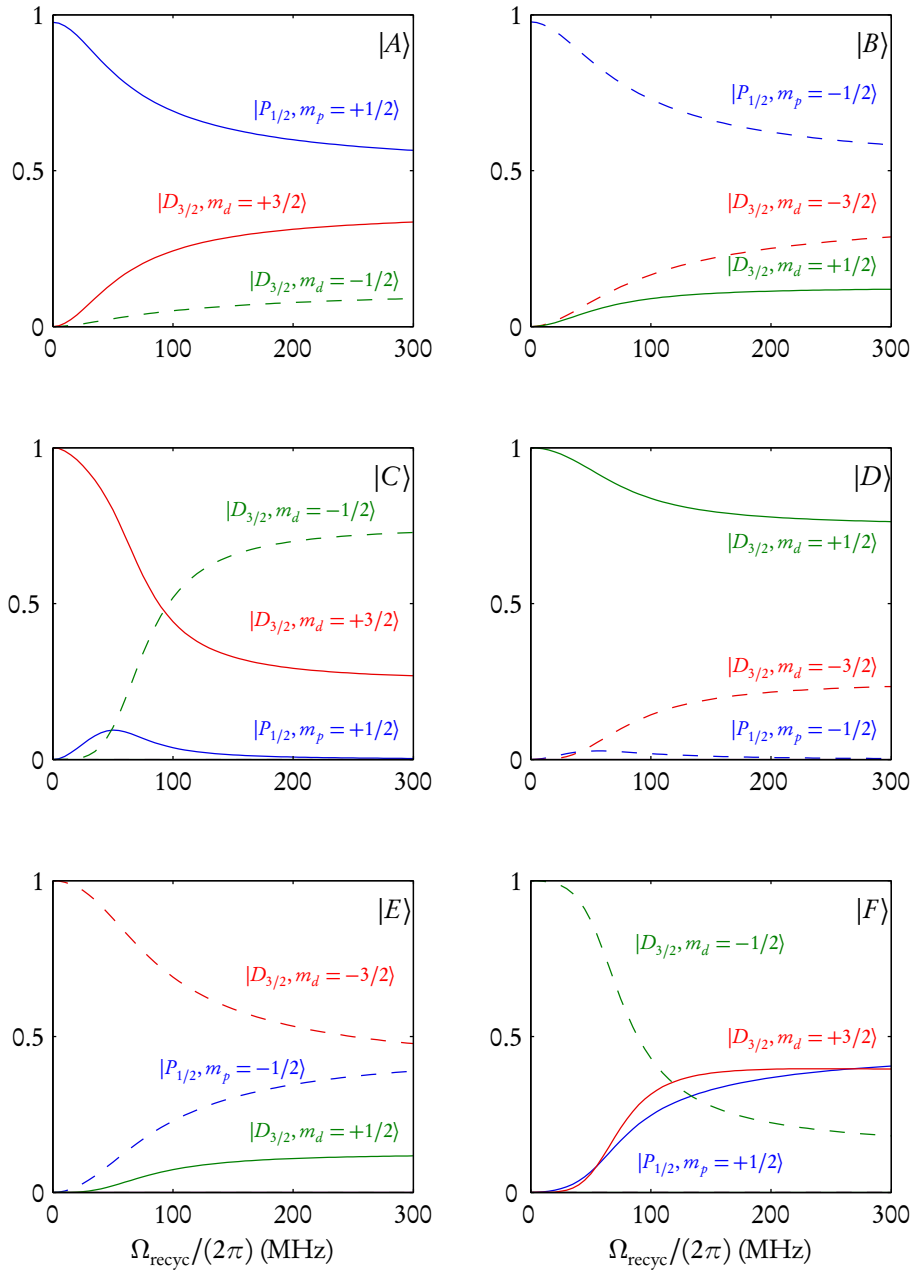

Figure 8.3: Decomposition of some of the eigenstates in the basis of bare states, as a function of the Rabi frequency of the recycling beam, Ω_{recyc}, for $(\Omega_{\text{driv}}, \Delta_{\text{driv}})/(2\pi) = (220, -400)$ MHz and $\Delta_{\text{recyc}}/(2\pi) = -20$ MHz. The overlap of the dressed eigenstates $|A\rangle$-$|F\rangle$ with the bare states $|D_{3/2}, m_d = +3/2\rangle$, $|D_{3/2}, m_d = +1/2\rangle$ and $|P_{1/2}, m_p = +1/2\rangle$ is represented by the solid red, green and blue lines, respectively. Similarly, the overlap with the bare states $|D_{3/2}, m_d = -3/2\rangle$, $|D_{3/2}, m_d = -1/2\rangle$ and $|P_{1/2}, m_p = -1/2\rangle$ is represented by the dashed red, green and blue lines. At low intensities of the recycling laser, the eigenstates $|A\rangle$, $|C\rangle$ and $|E\rangle$ are composed mainly of the states $|P_{1/2}, m_p = +1/2\rangle$, $|D_{3/2}, m_d = +3/2\rangle$ and $|D_{3/2}, m_d = -1/2\rangle$, respectively, while the eigenstates $|B\rangle$, $|D\rangle$ and $|F\rangle$ are essentially given by $|P_{1/2}, m_p = -1/2\rangle$, $|D_{3/2}, m_d = +1/2\rangle$ and $|D_{3/2}, m_d = -3/2\rangle$. The contributions of the P states to the eigenstates $|C\rangle$ and $|D\rangle$ are maximal at around $\Omega_{\text{recyc}}/(2\pi) \approx 50$ MHz.

8.2). The eigenstates $|C\rangle$ and $|D\rangle$ are now composed of a mixture of one $P_{1/2}$ and two $D_{3/2}$ sub-levels (see Figure 8.3). The $P_{1/2}$ component is maximal at $\Omega_{\text{recyc}}/(2\pi) \approx 50$ MHz. This point marks the optimum recycling efficiency and is associated with the end of region II.

For higher intensities of the recycling laser, the dynamic Stark shifts increase to the point that the energies of the states $|C\rangle$ and $|D\rangle$ are nearly identical. For instance, the vacuum-Raman transitions $G \leftrightarrow C$ and $G \leftrightarrow D$ are nearly degenerate: for a given cavity detuning, both transitions contribute to the cavity field. In turn, the additional ion-cavity interactions contribute to an increase of the rate of photon emission into the cavity. In other words, the dressing by the recycling laser field leads to a merging of the Raman transitions: the increase in the gain of the medium leads to an increase in the photon emission rate.

At some point, the photon population in the cavity is sufficiently large to allow stimulated processes to play a significant role: the photon emission rate increases further while the intensity fluctuations decrease.

Similarly to a conventional laser, the single-ion device displays a threshold that marks the beginning of laser action.

In summary, the threshold is established because the dynamic Stark shift leads to a merging of Raman transitions which in turn leads to the growth of the intra-cavity photon number in region III.

Region IV: (Self-)quenching

Lasing far above threshold, however, is not possible. In region IV of Figure 8.1, $\bar{n}$ and Q both decrease and the photon statistics even returns to the quantum domain, with $Q = -2.0(2)$ % and $\bar{n} = 0.06(6)$ for $\Omega_{\text{recyc}}/2\pi \approx 283$ MHz : the laser turns off. This behaviour has been predicted in the literature [32, 33] and is the so-called *self-quenching* of single-atom lasers.

The self-quenching mechanism we observe is independent of the cavity field. It originates from the complex internal level structure of the ion and is a direct consequence of the dressing of states by the recycling laser. This can be understood by continuing the analysis of Figure 8.3: for increasing intensities of the recycling laser, the amplitude of the $P_{1/2}$ component in both $|C\rangle$ and $|D\rangle$ eigenstates vanishes, rendering the recycling mechanism progressively less and less efficient. Consequently, the photon emission rate will eventually decrease, despite the merging of Raman transitions.

8.4 Accessible photon emission regimes

In order to frame the experimental results in the parameter space, we have performed numerical simulations of the single-ion device for a range of Rabi frequencies for the driving and recycling lasers, while approximately maintaining the Raman resonance with one of the Zeeman transitions ($|S_{1/2}, m_s = +1/2\rangle \leftrightarrow |D_{3/2}, m_d = +3/2\rangle$), thus mimicking the experimental procedure in the previous section, albeit at a different cavity detuning. This particular choice of detuning highlights the transition between two lasing regimes: the thresholdless quantum laser and the semiclassical laser on threshold. The simulations were performed using a magnetic field of $B = 2.7$ G, an ion-cavity coupling of $g/(2\pi) = 1.3$ MHz, and driving and recycling laser linewidths of $\delta_{\text{driv}} = 20$ kHz and $\delta_{\text{recyc}} = 200$ kHz respectively.

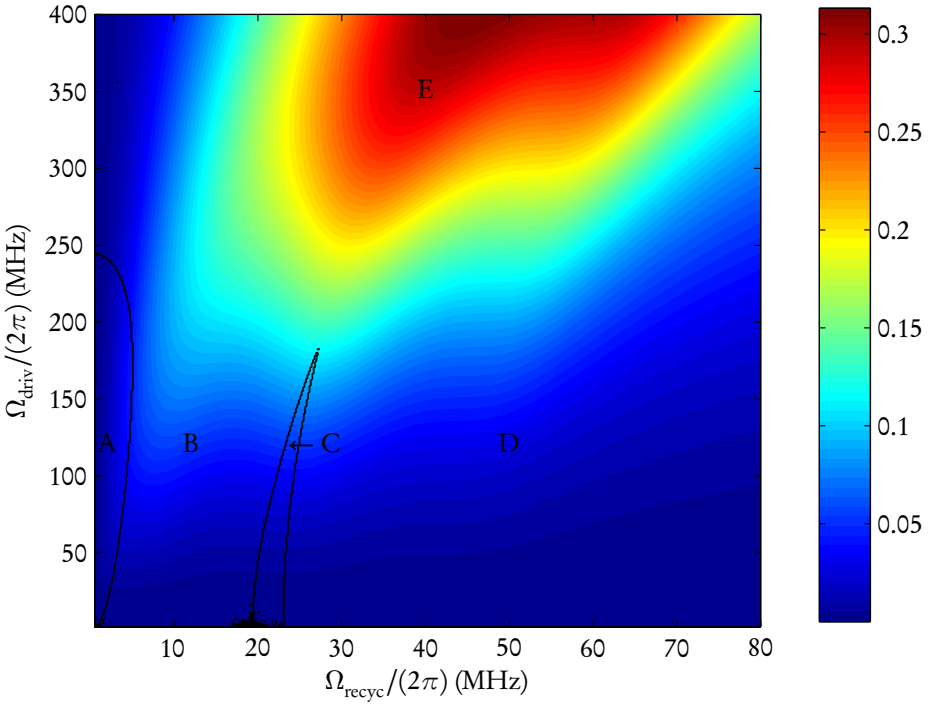

Figure 8.4: Average intracavity photon number as a function of the Rabi frequencies of the driving and recycling lasers (Ω_{driv} and Ω_{recyc}, respectively). The solid black lines correspond to the limits of the potential lasing regions, A and C, in which the average photon number grows while the noise fluctuations decrease.

Figures 8.4 and 8.5 show the intra-cavity photon number $\bar{n}$ and Mandel Q parameter as a function of the Rabi frequencies of the driving and recycling lasers. The regions (A and C) in the parameter space that obey the criterion of increasing $\bar{n}$ and decreasing Q for increasing Ω_{recyc} are delimited by the black line. As discussed in the previous section, these regions mark potential lasing regimes. To confirm the increase of stimulated emission in these regions, we present the R parameter in Figure 8.6.

Regions A, B, C and D relate well to regions I-IV in Figure 8.1.

Region A occurs at low intensities of both driving and recycling laser ($\Omega_{recyc}/(2\pi) \approx$ 10 MHz and ($\Omega_{driv}/(2\pi) < 150$ MHz). Consequently, the ion-cavity system is in an effective strong coupling regime. This regime is characterised by a simultaneous increase of the cavity output and decrease of the intensity fluctuations (Q). No threshold is observed. The fundamental difference between region A in Figures 8.4,8.5 and 8.6 and region I in Figure 8.1 is the fact that in the case of the latter the R parameter is high, indicating the stimulated emission dominates over the spontaneous processes. Since the light at the cavity output follows sub-Poissonian statistics, the single-ion device is acting as a thresholdless quantum laser. This is a consequence of the narrow linewidth of the driving laser assumed for the simulations. If broadband lasers would be used instead, the coherent Raman transition would suffer a larger damping due to the additional dephasing, which could frustrate photon emission into the cavity mode. Consequently, $\bar{n}$ would decrease and it would not be possible to reach such

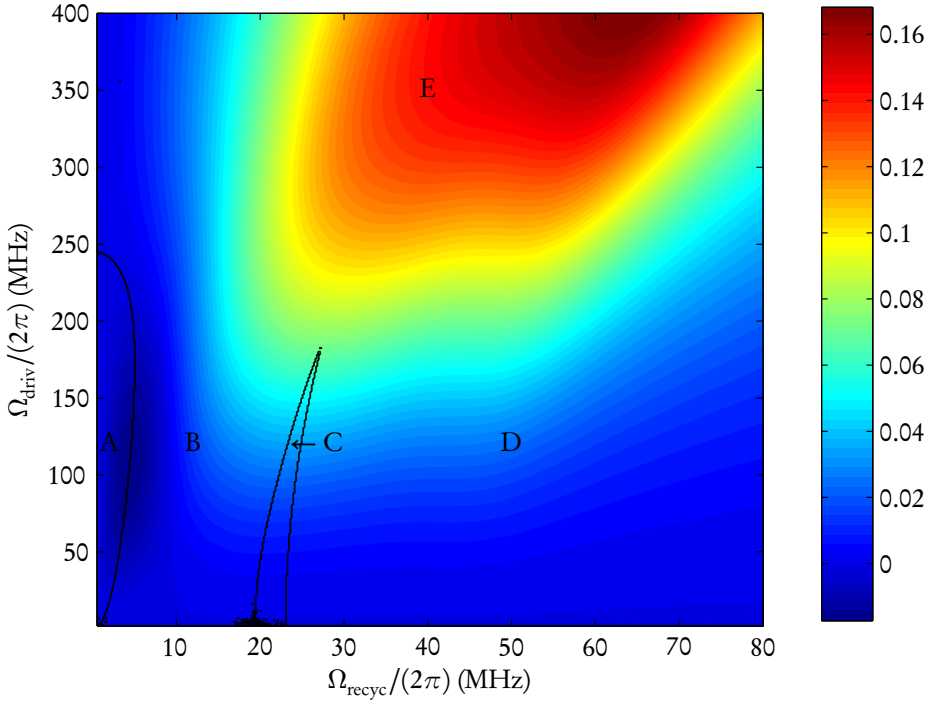

Figure 8.5: Mandel Q-parameter as a function of the Rabi frequencies of the driving and recycling lasers. The solid black lines correspond to the limits of the potential lasing regions, A and C, in which the average photon number grows while the noise fluctuations decrease. The single-ion device displays both sub- and super-Poissonian light.

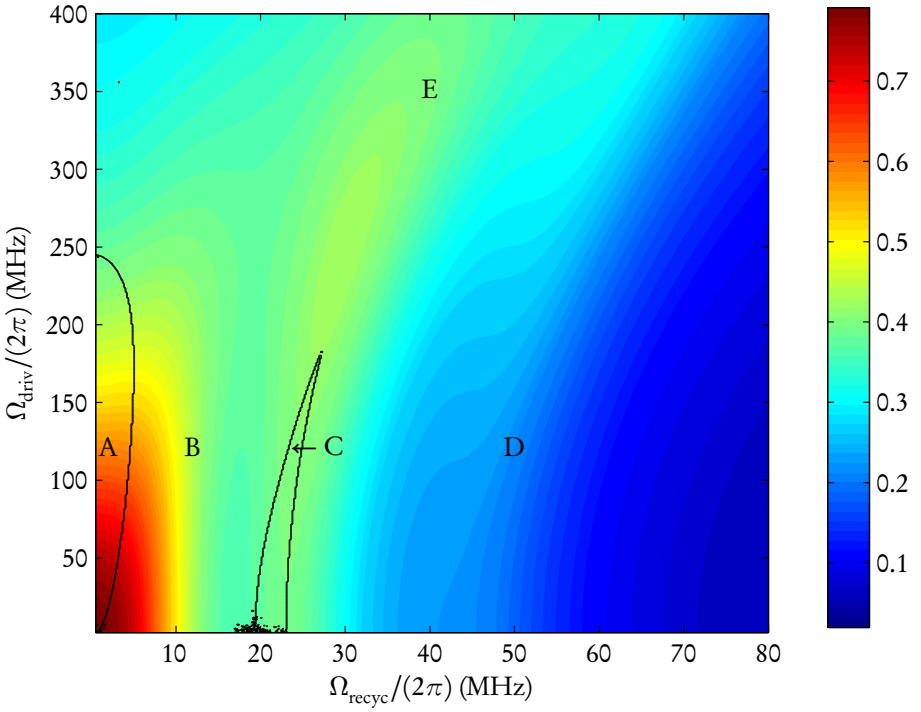

Figure 8.6: R parameter as a function of the Rabi frequencies of the driving and recycling lasers. The solid black lines correspond to the limits of the potential lasing regions, A and C, in which the average photon number grows while the noise fluctuations decrease. The R parameter has local maxima in regions A and C.

a low value for the Q parameter. Likewise, the R parameter would drop to a lower value and the light at the cavity output would present a wider linewidth.

Region B is the intermediate case between regions A and C: for increasing strengths of driving and recycling lasers, the ion-cavity system moves away from the strong coupling regime. Both $\bar{n}$ and Q increase, due to the increasing role of the incoherent processes. The results of chapter 7 were obtained in this region.

Region C is similar to region III of Figure 8.1, as it is characterised by an increasing intracavity photon number $\bar{n}$ and decreasing Mandel Q parameter, for positive Q. The R parameter displays a local maximum, which marks the emergence of a threshold. Within this regime, the single-ion device behaves as a semiclassical laser on threshold.

Region D corresponds to the self-quenching regime (region IV of Figure 8.1): the recycling process become inefficient and the photon emission rate decreases.

Region E is defined by very high intensities of the driving laser ($\Omega_{\text{driv}}/(2\pi) > 300$ MHz). The coherence of the effective ion-cavity coupling is weakened by the excessive off-resonant excitation of the $P_{1/2}$ state, which increases the linewidth γ_{eff} of the Raman transition. Consequently, and despite the fact that the intra-cavity photon number continues to increase, the R parameter smoothly decreases with increasing intensity of the driving laser and the system no longer displays any lasing behaviour. In other words, the single-ion device reaches the bad-atom limit (see section 2.1.4): its dynamics is completely dominated by incoherent processes.

8.5 Addendum: single-ion laser in the quantum regime

Recently, during the revision stage of this dissertation, a series of significant experimental improvements lead to a reduction of the linewidth of the driving laser at 397 nm to $\delta_{\text{driv}}/(2\pi) = 30$ kHz.

Under these improved conditions, a new series of measurements was completed before submission of this dissertation. Nonetheless, we found it timely to present some experimental results that demonstrate a single-ion laser in the quantum regime.

As previously discussed, at low Rabi frequencies of the driving laser, the single-ion device can behave as a single-ion laser in the quantum regime. However, it is not practicable to choose a very low Rabi frequency of the driving laser, since that would slow down the photon emission process, leading to a poor signal-to-noise ratio. Given the experimental conditions, we found $\Omega_{\text{driv}}/(2\pi) \sim 80$ MHz to be a good compromise. The cavity detuning was set to match the peak relative to the bare $|S_{1/2}, +1/2\rangle \leftrightarrow |D_{3/2}, +3/2\rangle$ transition, which corresponds to enforcing the condition: $\Delta_c = \Delta_p - \frac{3}{5} \cdot \mu_B B$. The choice of this particular vacuum-stimulated Raman transition allows a maximum intracavity photon number.

Akin to the procedure described in section 8.3, the photodetection events were recorded as the intensity of the recycling laser was progressively increased. The experimental improvements also allowed the measurement of fluorescence at 397 nm, which allowed the direct measurement of the R parameter.

We present in Figure 8.7 the results obtained for $(\Omega_{\text{driv}}, \Delta_{\text{driv}}) \approx (88, -353)$ MHz, namely the average intracavity photon number ($\bar{n}$, top plot), the Mandel Q parameter (middle plot) and the R parameter (bottom plot). The points mark the experimental results while the solid lines show the results of the numerical simulation of our model. In general, we find good quantitative agreement with the experimental results, the slight disagreement at large Rabi frequencies of the recycling laser (Ω_{recyc}) is

attributed to the fact that the model assumes that the ion is at rest, which is obviously not the case, since no additional laser cooling mechanism was introduced.

The results are characterized by three distinctive regions, marked with capital Roman numerals I–III.

Region I is loosely delimited by the condition $0\,\text{MHz} < \Omega_{\text{recyc}}/(2\pi) \lesssim 5\,\text{MHz}$: it is characterized by an increase of the intensity of the cavity output (increasing n_{ss}) and a simultaneous decrease of the intensity fluctuations (decreasing Q parameter), as a function of the Rabi frequency of the external recycling laser. In contrast with the results obtained in region I of Figure 8.1 in section 8.3, the R parameter approaches 1 and the single-ion device behaves like a thresholdless laser exhibiting quantum statistics.

In Region II ($5\,\text{MHz} \lesssim \Omega_{\text{recyc}}/(2\pi) \lesssim 10\,\text{MHz}$), the average intracavity photon number increases but so do the Q and R parameters. In this region, the phase noise introduced by the photon scattering in the $|P_{1/2}\rangle \longleftrightarrow |D_{3/2}\rangle$ transition dampens the coherence introduced by the effective ion-cavity coupling and the single-ion device ceases lasing. Nevertheless, the intracavity photon number continues to grow, because the strong recycling laser leads to a shorter cycling time of the atomic population, meaning that photons can be produced at a faster rate, albeit at the cost of added noise.

Finally, in region III ($10\,\text{MHz} \lesssim \Omega_{\text{recyc}}/(2\pi) \lesssim 30\,\text{MHz}$), the average intracavity photon number decreases, as well as the Mandel Q parameter. The interaction of the ion with the recycling laser leads to light shifts on the $P_{1/2}$ and $D_{3/2}$ manifolds, which in turn detunes the vacuum-stimulated Raman transitions and photon emission into the cavity mode decreases. Akin to region IV of Figure 8.1, this corresponds to the regime of self-quenching.

Globally, these results compare well with theoretical analyses found in the literature [32, 33] on the thresholdless one-atom laser.

8.6 Summary and Conclusion

In summary, we have discussed measurements on the photon statistics of our single-ion device. We observe the photon statistics of the cavity output as a function of the intensity of the external excitation.

In particular, we have found a regime in which the single-ion device resembles a conventional laser operating at threshold and that is characterised by super-Poissonian statistics. We have provided a detailed analysis regarding the establishment of the threshold and the self-quenching mechanism.

Very recently, we were also able to demonstrate that the single-ion device resembles a thresholdless (quantum) laser, as described in the literature.

Moreover, we have developed a numerical model which allows us to predict the various photon emission regimes that can be reached with our single-photon device. Even though the model does not include motional effects, it correctly predicts that the same single-ion device can behave as a laser both in a manifestly quantum regime as well as in a clearly classical regime.

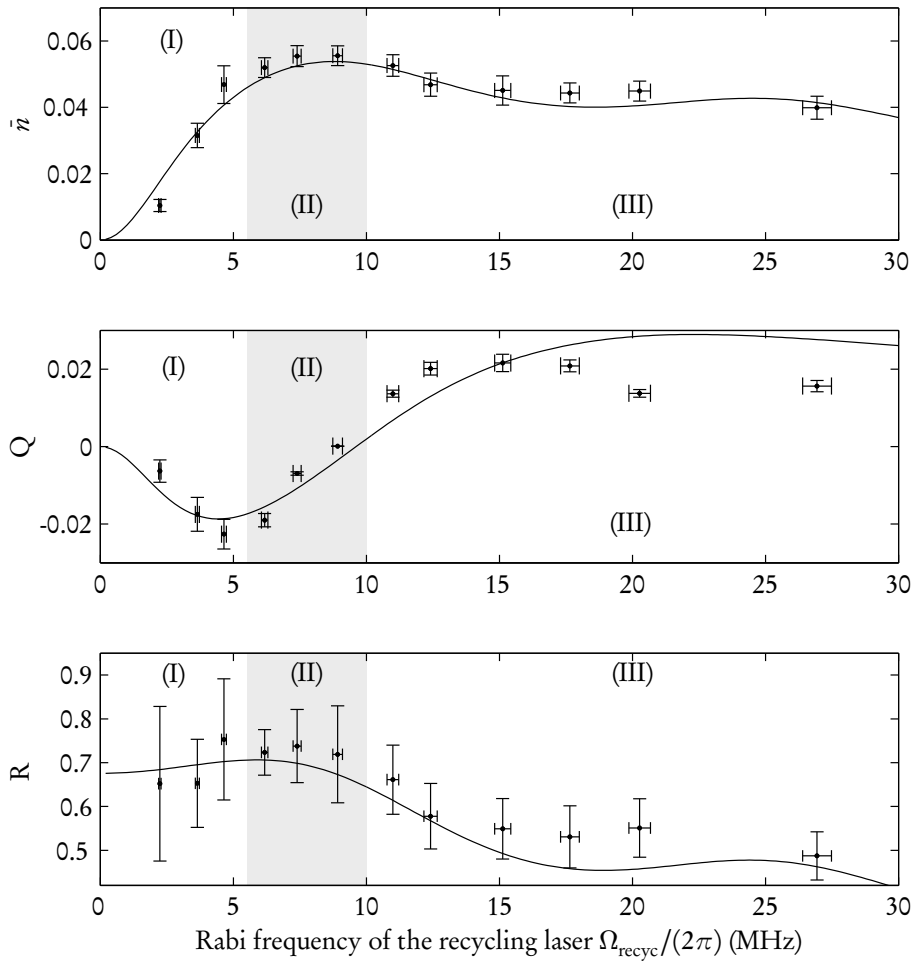

Figure 8.7: Experimental results obtained for $(\Omega_{\mathrm{driv}}, \Delta_{\mathrm{driv}})/(2\pi) = (88, -353)$ MHz (points) and respective simulated results (solid lines). Top: average intracavity photon number ($\bar{n}$). Middle: Mandel Q parameter. Bottom: R parameter. Regions I–III mark the regimes of thresholdless lasing, turning off of the laser and self-quenching, respectively.

Chapter 9

Summary and Outlook

Summary

A new experimental setup was designed and built with the necessary degrees of freedom to allow tunable coupling of one or more ions to a cavity mode. The system was extensively calibrated and all relevant physical quantities were independently measured. The excellent agreement of the experimental results with numerical simulations confirm that the system is completely understood.

The experiments reported in this dissertation demonstrate the flexibility of a single-ion device composed by a single trapped ion coupled to a cavity. In particular we have explored the fact that such a system is a light source with highly configurable properties. The exact frequency and polarisation of the output can be chosen by controlling the detunings of the driving laser and the optical resonator. The statistical properties of the light at the cavity output can be controlled by setting the intensity of the driving and recycling lasers: under pulsed excitation we have demonstrated an efficient triggerable single-photon source; under continuous excitation we have shown tunable photon statistics. Moreover, we have shown that our single-ion device exhibits a smooth transition from a single-photon emitter with manifestly quantum behaviour to a semi-classical single-ion laser operating at threshold. Finally, recent progress on the improvement of the linewidth of the driving laser at 397 nm allowed the exploration of the quantum regime of the single-ion laser.

Outlook

The experimental setup allows for further fundamental study of the emergence of a threshold in the semiclassical laser regime. One possible route would be the investigation of the different regimes when two or more ions are coupled to the cavity mode. Another possible route would be the study of the effects of an increased feedback mechanism. Such conditions could be achieved by collecting a fraction of the photon stream at the cavity output into a fibre and coupling the other end to the cavity input, or by simply building an external cavity around the single-ion device. Alternatively, a quantum laser amplifier could be implemented: by seeding light at 866 nm from an external source, it may be possible to observe amplification of light by the ion at the cavity output.

Now that the recent improvements on the linewidth of the driving laser at 397 nm have allowed the exploration of the quantum regime of the single-ion laser, the pulsed

operation of the single-ion device introduces interesting possibilities: it allows the implementation of a single-photon source with improved coherence properties, due to the higher single-photon emission efficiencies. By introducing a delay line, two-photon interference experiments could also be performed, which could be used to further characterize the single-photon source: the indistinguishability of the emitted photons could be tested.

Furthermore, by implementing the single-photon source on the Λ-system composed by the manifolds $S_{1/2}$, $P_{3/2}$ and $D_{5/2}$, the laser at 729 nm could be used to read out the atomic state by probing the $S_{1/2} \leftrightarrow D_{5/2}$ quadrupole transition: it would then be possible to create entangled atom-photon states and simultaneously measure the atomic and photonic subspaces. With these tools, several protocols are at reach, namely reversible quantum mapping of the state of an atom into a photonic state, as well as the teleportation of the internal state of an atom over a distance of several hundred meters to another atom.

It becomes clear that such coherent control over a larger number of qubits could be used to link quantum processors of medium size (nodes) to create a cluster with many qubits. Future setups with improved ion-cavity coupling could eventually be used to establish a quantum network, thus transforming the concept of quantum information processing into a real commonplace.

Bibliography

[1] R. H. Brown and R. Q. Twiss, *Correlation between Photons in two Coherent Beams of Light*, Nature **177**, 27 (1956).
Cited in page(s): 1, 23

[2] R. H. Brown and R. Q. Twiss, *A Test of a New Type of Stellar Interferometer on Sirius*, Nature **178**, 1046 (1956).
Cited in page(s): 1, 23

[3] H. J. Kimble, M. Dagenais, and L. Mandel, *Photon Antibunching in Resonance Fluorescence*, Physical Review Letters **39**, 691 (1977).
Cited in page(s): 1, 23

[4] R. Short and L. Mandel, *Observation of Sub-Poissonian Photon Statistics*, Physical Review Letters **51**, 384 (1983).
Cited in page(s): 1

[5] G. Rempe, F. Schmidt-Kaler, and H. Walther, *Observation of sub-Poissonian photon statistics in a micromaser*, Physical Review Letters **64**, 2783 (1990).
Cited in page(s): 1

[6] G. Rempe and H. Walther, *Sub-Poissonian atomic statistics in a micromaser*, Physical Review A **42**, 1650 (1990).
Cited in page(s): 1

[7] M. C. Teich and B. E. A. Saleh, *Effects of random deletion and additive noise on bunched and antibunched photon-counting statistics*, Optics Letters **7**, 365 (1982).
Cited in page(s): 1

[8] T. H. Maiman, *Stimulated Optical Radiation in Ruby*, Nature **187**, 493 (1960).
Cited in page(s): 1, 109

[9] J. P. Gordon, H. J. Zeiger, and C. H. Townes, *Molecular Microwave Oscillator and New Hyperfine Structure in the Microwave Spectrum of NH_3*, Physical Review **95**, 282 (1954).
Cited in page(s): 1

[10] J. P. Gordon, H. J. Zeiger, and C. H. Townes, *The Maser: New Type of Microwave Amplifier, Frequency Standard, and Spectrometer*, Physical Review **99**, 1264 (1955).
Cited in page(s): 1

[11] R. van Dyck, P. Ekstrom, and H. Dehmelt, *Axial, magnetron, cyclotron and spin-cyclotron-beat frequencies measured on single electron almost at rest in free space (geonium)*, Nature **262**, 776 (1976).
Cited in page(s): 1

[12] W. Neuhauser, M. Hohenstatt, P. E. Toschek, and H. Dehmelt, *Localized visible Ba^+ mono-ion oscillator*, Physical Review A **22**, 1137 (1980).
Cited in page(s): 1

[13] W. Paul, *Electromagnetic traps for charged and neutral particles*, Reviews of Modern Physics **62**, 531 (1990).
Cited in page(s): 1, 35, 36

[14] T. Rosenband, D. B. Hume, P. O. Schmidt, C. W. Chou, A. Brusch, L. Lorini, W. H. Oskay, R. E. Drullinger, T. M. Fortier, J. E. Stalnaker, S. A. Diddams, W. C. Swann, N. R. Newbury, W. M. Itano, D. J. Wineland, and J. C. Bergquist, *Frequency Ratio of Al^+ and Hg^+ Single-Ion Optical Clocks; Metrology at the 17th Decimal Place*, Science **319**, 1808 (2008).
Cited in page(s): 1

[15] D. Bouwmeester, A. K. Ekert, and A. Zeilinger, *The Physics of Quantum Information: Quantum Cryptography* (Springer, 2000), 1 edn. [link].
Cited in page(s): 2, 93

[16] M. A. Nielsen and I. L. Chuang, *Quantum Computation and Quantum Information* (Cambridge University Press, 2000), 1 edn. [link].
Cited in page(s): 2

[17] F. Schmidt-Kaler, H. Häffner, M. Riebe, S. Gulde, G. P. T. Lancaster, T. Deuschle, C. Becher, C. F. Roos, J. Eschner, and R. Blatt, *Realization of the Cirac-Zoller controlled-NOT quantum gate*, Nature **422**, 408 (2003).
Cited in page(s): 2

[18] D. Leibfried, B. DeMarco, V. Meyer, D. Lucas, M. Barrett, J. Britton, W. M. Itano, B. Jelenkovic, C. Langer, T. Rosenband, and D. J. Wineland, *Experimental demonstration of a robust, high-fidelity geometric two ion-qubit phase gate*, Nature **422**, 412 (2003).
Cited in page(s): 2

[19] S. Gulde, M. Riebe, G. P. T. Lancaster, C. Becher, J. Eschner, H. Häffner, F. Schmidt-Kaler, I. L. Chuang, and R. Blatt, *Implementation of the Deutsch-Jozsa algorithm on an ion-trap quantum computer*, Nature **421**, 48 (2003).
Cited in page(s): 2

[20] M. Riebe, H. Häffner, C. F. Roos, W. Hansel, J. Benhelm, G. P. T. Lancaster, T. W. Korber, C. Becher, F. Schmidt-Kaler, D. F. V. James, and R. Blatt, *Deterministic quantum teleportation with atoms*, Nature **429**, 734 (2004).
Cited in page(s): 2

[21] R. Ursin, F. Tiefenbacher, T. Schmitt-Manderbach, H. Weier, T. Scheidl, M. Lindenthal, B. Blauensteiner, T. Jennewein, J. Perdigues, P. Trojek, B. Omer, M. Furst, M. Meyenburg, J. Rarity, Z. Sodnik, C. Barbieri, H. Weinfurter, and A. Zeilinger, *Entanglement-based quantum communication over*

144 km, Nature Physics **3**, 481 (2007).
Cited in page(s): 2

[22] O. Landry, J. A. W. van Houwelingen, A. Beveratos, H. Zbinden, and N. Gisin, *Quantum teleportation over the Swisscom telecommunication network*, Journal of the Optical Society of America B: Optical Physics **24**, 398 (2007).
Cited in page(s): 2

[23] T. Pellizzari, S. A. Gardiner, J. I. Cirac, and P. Zoller, *Decoherence, Continuous Observation, and Quantum Computing: A Cavity QED Model*, Physical Review Letters **75**, 3788 (1995).
Cited in page(s): 2

[24] J. I. Cirac, P. Zoller, H. J. Kimble, and H. Mabuchi, *Quantum State Transfer and Entanglement Distribution among Distant Nodes in a Quantum Network*, Physical Review Letters **78**, 3221 (1997).
Cited in page(s): 2, 94

[25] Q. A. Turchette, R. J. Thompson, and H. J. Kimble, *One-dimensional atoms*, Applied Physics B: Lasers and Optics **60**, S1 (1995).
Cited in page(s): 2, 12

[26] G. R. Guthohrlein, M. Keller, K. Hayasaka, W. Lange, and H. Walther, *A single ion as a nanoscopic probe of an optical field*, Nature **414**, 49 (2001).
Cited in page(s): 2, 84, 85

[27] A. B. Mundt, A. Kreuter, C. Becher, D. Leibfried, J. Eschner, F. Schmidt-Kaler, and R. Blatt, *Coupling a Single Atomic Quantum Bit to a High Finesse Optical Cavity*, Physical Review Letters **89**, 103001 (2002).
Cited in page(s): 2

[28] A. Kreuter, C. Becher, G. P. T. Lancaster, A. B. Mundt, C. Russo, H. Häffner, C. Roos, J. Eschner, F. Schmidt-Kaler, and R. Blatt, *Spontaneous Emission Lifetime of a Single Trapped $^{40}Ca^{+}$ Ion in a High Finesse Cavity*, Physical Review Letters **92**, 203002 (2004).
Cited in page(s): 2

[29] C. K. Law and H. J. Kimble, *Deterministic generation of a bit-stream of single-photon pulses*, Journal of Modern Optics **44**, 2067 (1997).
Cited in page(s): 2, 93

[30] A. S. Parkins, P. Marte, P. Zoller, and H. J. Kimble, *Synthesis of arbitrary quantum states via adiabatic transfer of Zeeman coherence*, Physical Review Letters **71**, 3095 (1993).
Cited in page(s): 2, 93

[31] C. Maurer, C. Becher, C. Russo, J. Eschner, and R. Blatt, *A single-photon source based on a single Ca^{+} ion*, New Journal of Physics **6**, 94 (2004).
Cited in page(s): 2, 94

[32] Y. Mu and C. M. Savage, *One-atom lasers*, Physical Review A **46**, 5944 (1992).
Cited in page(s): 3, 19, 110, 117, 122

[33] G. M. Meyer, H. J. Briegel, and H. Walther, *Ion-trap laser*, Europhysics Letters (EPL) **37**, 317 (1997).
Cited in page(s): 3, 20, 110, 111, 114, 117, 122

[34] M. O. Scully and M. S. Zubairy, *Quantum Optics* (Cambridge University Press, 1997). [link].
Cited in page(s): 5

[35] E. Jaynes and F. Cummings, *Comparison of quantum and semiclassical radiation theories with application to the beam maser*, Proceedings of the IEEE **51**, 89 (1963).
Cited in page(s): 6

[36] H. Carmichael, *An Open Systems Approach to Quantum Optics: Lectures Presented at the Universite Libre De Bruxelles October 28 to November 4, 1991 (Lecture Notes in Physics New Series M)* (Springer, 1993).
Cited in page(s): 9, 12, 23, 33

[37] C. Gardiner and P. Zoller, *Quantum Noise: A Handbook of Markovian and Non-Markovian Quantum Stochastic Methods with Applications to Quantum Optics*, Springer Series in Synergetics (Springer, 2004), 3 edn. [link].
Cited in page(s): 9, 108, 110

[38] E. M. Purcell, *Spontaneous Emission Probabilities at Radio Frequencies*, Physical Review **69**, 681 (1946).
Cited in page(s): 12

[39] A. Kreuter, *Spontaneous emission of a single trapped Ca^+ ion*, Doctoral dissertation, University of Innsbruck (2004). [link].
Cited in page(s): 12, 56, 60

[40] D. Kleppner, *Inhibited Spontaneous Emission*, Physical Review Letters **47**, 233 (1981).
Cited in page(s): 12

[41] P. Goy, J. M. Raimond, M. Gross, and S. Haroche, *Observation of Cavity-Enhanced Single-Atom Spontaneous Emission*, Physical Review Letters **50**, 1903 (1983).
Cited in page(s): 12

[42] C. C. Gerry and J. H. Eberly, *Dynamics of a Raman coupled model interacting with two quantized cavity fields*, Physical Review A **42**, 6805 (1990).
Cited in page(s): 14

[43] M. Alexanian and S. K. Bose, *Unitary transformation and the dynamics of a three-level atom interacting with two quantized field modes*, Physical Review A **52**, 2218 (1995).
Cited in page(s): 14

[44] Y. Wu, *Effective Raman theory for a three-level atom in the Lambda configuration*, Physical Review A **54**, 1586 (1996).
Cited in page(s): 14, 16

[45] C. Di Fidio, S. Maniscalco, W. Vogel, and A. Messina, *Cavity QED with a trapped ion in a leaky cavity*, Physical Review A **65**, 033825 (2002).
Cited in page(s): 14

[46] W. Vogel and D. G. Welsch, *Lectures on Quantum Optics* (Wiley-VCH, 1994).
Cited in page(s): 18, 33

[47] G. S. Agarwal and S. Dutta Gupta, *Steady states in cavity QED due to incoherent pumping*, Physical Review A **42**, 1737 (1990).
Cited in page(s): 19

[48] J. McKeever, A. Boca, A. D. Boozer, J. R. Buck, and H. J. Kimble, *Experimental realization of a one-atom laser in the regime of strong coupling*, Nature **425**, 268 (2003).
Cited in page(s): 20, 110, 112

[49] A. D. Boozer, A. Boca, J. R. Buck, J. McKeever, and H. J. Kimble, *Comparison of theory and experiment for a one-atom laser in a regime of strong coupling*, Physical Review A **70**, 023814 (2004).
Cited in page(s): 20, 110, 111, 112

[50] L. Mandel and E. Wolf, *Optical Coherence and Quantum Optics* (Cambridge University Press, 1995), 1 edn. [link].
Cited in page(s): 21, 110

[51] P. L. Kelley and W. H. Kleiner, *Theory of Electromagnetic Field Measurement and Photoelectron Counting*, Physical Review **136**, A316 (1964).
Cited in page(s): 21

[52] R. J. Glauber, *The Quantum Theory of Optical Coherence*, Physical Review **130**, 2529 (1963).
Cited in page(s): 22

[53] R. J. Glauber, *Coherent and Incoherent States of the Radiation Field*, Physical Review **131**, 2766 (1963).
Cited in page(s): 22

[54] A. Kreuter, C. Becher, G. P. T. Lancaster, A. B. Mundt, C. Russo, H. Häffner, C. Roos, W. Hansel, F. Schmidt-Kaler, R. Blatt, and M. S. Safronova, *Experimental and theoretical study of the 3d ^{2}D-level lifetimes of $^{40}Ca^+$*, Physical Review A **71**, 032504 (2005).
Cited in page(s): 25

[55] P. A. Barton, C. J. S. Donald, D. M. Lucas, D. A. Stevens, A. M. Steane, and D. N. Stacey, *Measurement of the lifetime of the $3d^2D_{5/2}$ state in $^{40}Ca^+$*, Physical Review A **62**, 032503 (2000).
Cited in page(s): 25

[56] S. M. Tan, *A computational toolbox for quantum and atomic optics*, Journal of Optics B: Quantum and Semiclassical Optics **1**, 424 (1999).
Cited in page(s): 34

[57] D. Leibfried, R. Blatt, C. Monroe, and D. Wineland, *Quantum dynamics of single trapped ions*, Reviews of Modern Physics **75**, 281 (2003).
Cited in page(s): 36

[58] M. G. Raizen, J. M. Gilligan, J. C. Bergquist, W. M. Itano, and D. J. Wineland, *Ionic crystals in a linear Paul trap*, Physical Review A **45**, 6493 (1992).
Cited in page(s): 37

[59] D. J. Wineland, C. Monroe, W. M. Itano, D. Leibfried, B. E. King, and D. M. Meekhof, *Experimental Issues in Coherent Quantum-State Manipulation of Trapped Atomic Ions*, Journal of Research of the National Institute of Standards and Technology **103**, 259 (1998).
Cited in page(s): 37, 85

[60] M. Drewsen and A. Brøner, *Harmonic linear Paul trap: Stability diagram and effective potentials*, Physical Review A **62**, 045401 (2000).
Cited in page(s): 37

[61] C. Roos, *Controlling the quantum state of trapped ions*, Doctoral dissertation, University of Innsbruck (2000). [link].
Cited in page(s): 37, 56, 70, 73

[62] S. Gulde, *Experimental realization of quantum gates and the Deutsch-Josza algorithm with trapped $^{40}Ca^{+}$-ions*, Doctoral dissertation, University of Innsbruck (2003). [link].
Cited in page(s): 37, 38, 56, 70, 71, 73

[63] M. Riebe, *Preparation of entangled states and quantum teleportation with atomic qubits*, Doctoral dissertation, University of Innsbruck (2005). [link].
Cited in page(s): 38, 56

[64] A. Siegman, *Lasers* (University Science Books, Mill Valley, California, 1986).
Cited in page(s): 41, 42, 114

[65] B. E. A. Saleh and M. C. Teich, *Fundamentals of Photonics (Wiley Series in Pure and Applied Optics)* (Wiley and Sons, 1991).
Cited in page(s): 41

[66] N. Hodgson and H. Weber, *Optische Resonatoren. Grundlagen, Eigenschaften, Optimierung* (Springer, Berlin, 1992).
Cited in page(s): 41

[67] C. J. Hood, M. S. Chapman, T. W. Lynn, and H. J. Kimble, *Real-Time Cavity QED with Single Atoms*, Physical Review Letters **80**, 4157 (1998).
Cited in page(s): 43

[68] M. Hennrich, T. Legero, A. Kuhn, and G. Rempe, *Vacuum-Stimulated Raman Scattering Based on Adiabatic Passage in a High-Finesse Optical Cavity*, Physical Review Letters **85**, 4872 (2000).
Cited in page(s): 43

[69] A. Mundt, *Cavity QED with single trapped $^{40}Ca^{+}$-ions*, Doctoral dissertation, University of Innsbruck (2003). [link].
Cited in page(s): 47, 56, 60, 73

[70] T. Monz, *A frequency offset lock for cavity-driven Raman transitions*, Master's thesis, University of Innsbruck (2005). [link].
Cited in page(s): 49, 56

[71] C. J. Hood, H. J. Kimble, and J. Ye, *Characterization of high-finesse mirrors: Loss, phase shifts, and mode structure in an optical cavity*, Physical Review A **64**, 033804 (2001).
Cited in page(s): 50

[72] H.-C. Nägerl, *Ion strings for Quantum Computation*, Doctoral dissertation, University of Innsbruck (1998). [link].
Cited in page(s): 56, 70, 73

[73] B. H. Rohde, *Experimente zur Quanteninformationsverarbeitung in einer linearen Ionenfalle*, Doctoral dissertation, University of Innsbruck (2001). [link].
Cited in page(s): 56, 61, 70

[74] D. Rotter, *Photoionisation von Kalzium*, Master's thesis, University of Innsbruck (2003). [link].
Cited in page(s): 56, 69

[75] M. Bacher, *Sättigungsspektroskopie an Kalziumdampf und Laserstabilisierung fur Photoionisationsexperimente*, Master's thesis, University of Innsbruck (2005). [link].
Cited in page(s): 56, 59

[76] C. Maurer, *Kontrolle der Einphotonenemission eines einzelnen Ca^+-Ions*, Master's thesis, University of Innsbruck (2004). [link].
Cited in page(s): 56, 94

[77] M. Chwalla, *In preparation*, Doctoral dissertation, University of Innsbruck (2008).
Cited in page(s): 56, 57

[78] R. W. P. Drever, J. L. Hall, F. V. Kowalski, J. Hough, G. M. Ford, A. J. Munley, and H. Ward, *Laser phase and frequency stabilization using an optical resonator*, Applied Physics B: Lasers and Optics **31**, 97 (1983).
Cited in page(s): 56, 60

[79] S. Gulde, D. Rotter, P. Barton, F. Schmidt-Kaler, R. Blatt, and W. Hogervorst, *Simple and efficient photo-ionization loading of ions for precision ion-trapping experiments*, Applied Physics B: Lasers and Optics **73**, 861 (2001).
Cited in page(s): 59, 69

[80] G. Blasbichler, *Ein Lambdameter mit 10^{-7} Meßunsicherheit*, Master's thesis, University of Innsbruck (2000). [link].
Cited in page(s): 59

[81] A. Stute, *Ein Einzelphotonquelle mit einem $^{40}Ca^+$-Cavity-QED System*, Master's thesis, Universities of Innsbruck and Freiburg (2007). [link].
Cited in page(s): 59, 95

[82] D. J. Berkeland, J. D. Miller, J. C. Bergquist, W. M. Itano, and D. J. Wineland, *Minimization of ion micromotion in a Paul trap*, Journal of Applied Physics **83**, 5025 (1998).
Cited in page(s): 70

[83] H. C. Nägerl, C. Roos, D. Leibfried, H. Rohde, G. Thalhammer, J. Eschner, F. Schmidt-Kaler, and R. Blatt, *Investigating a qubit candidate: Spectroscopy on the S_{1/2} to D_{5/2} transition of a trapped calcium ion in a linear Paul trap*, Physical Review A **61**, 023405 (2000).
Cited in page(s): 73

[84] G. Alzetta, A. Gozzini, L. Moi, and G. Orriols, *An experimental method for the observation of rf transitions and laser beat resonances in oriented Na vapour*, Nuovo Cimento B **36**, 5 (1976).
Cited in page(s): 73

[85] J. Eschner, *Sub-wavelength resolution of optical fields probed by single trapped ions: Interference, phase modulation, and which-way information*, The European Physical Journal D - Atomic, Molecular, Optical and Plasma Physics **22**, 341 (2003).
Cited in page(s): 85

[86] R. H. Brown and R. Q. Twiss, *Interferometry of the Intensity Fluctuations in Light.I. Basic Theory: The Correlation between Photons in Coherent Beams of Radiation*, Proceedings of the Royal Society of London. Series A, Mathematical and Physical Sciences **242**, 300 (1957).
Cited in page(s): 88

[87] C. Kurtsiefer, P. Zarda, S. Mayer, and H. Weinfurter, *The breakdown flash of silicon avalanche photodiodes—back door for eavesdropper attacks?*, Journal of Modern Optics **48**, 2039 (2001).
Cited in page(s): 88

[88] D. P. DiVincenzo, *The Physical Implementation of Quantum Computation*, Fortschritte der Physik **48**, 771 (2000).
Cited in page(s): 93, 94

[89] E. Knill, R. Laflamme, and G. J. Milburn, *A scheme for efficient quantum computation with linear optics*, Nature **409**, 46 (2001).
Cited in page(s): 93

[90] B. Darquie, M. P. A. Jones, J. Dingjan, J. Beugnon, S. Bergamini, Y. Sortais, G. Messin, A. Browaeys, and P. Grangier, *Controlled Single-Photon Emission from a Single Trapped Two-Level Atom*, Science **309**, 454 (2005).
Cited in page(s): 93, 99

[91] P. Maunz, D. L. Moehring, S. Olmschenk, K. C. Younge, D. N. Matsukevich, and C. Monroe, *Quantum interference of photon pairs from two remote trapped atomic ions*, Nature Physics **3**, 538 (2007).
Cited in page(s): 93, 99, 100

[92] C. Brunel, B. Lounis, P. Tamarat, and M. Orrit, *Triggered Source of Single Photons based on Controlled Single Molecule Fluorescence*, Physical Review Letters **83**, 2722 (1999).
Cited in page(s): 93

[93] B. Lounis and W. E. Moerner, *Single photons on demand from a single molecule at room temperature*, Nature **407**, 491 (2000).
Cited in page(s): 93

[94] J. Kim, O. Benson, H. Kan, and Y. Yamamoto, *A single-photon turnstile device*, Nature **397**, 500 (1999).
Cited in page(s): 93

[95] C. Kurtsiefer, S. Mayer, P. Zarda, and H. Weinfurter, *Stable Solid-State Source of Single Photons*, Physical Review Letters **85**, 290 (2000).
Cited in page(s): 93

[96] R. Brouri, A. Beveratos, J.-P. Poizat, and P. Grangier, *Photon antibunching in the fluorescence of individual color centers in diamond*, Optics Letters **25**, 1294 (2000).
Cited in page(s): 93

[97] P. Michler, A. Kiraz, C. Becher, W. V. Schoenfeld, P. M. Petroff, L. Zhang, E. Hu, and A. Imamoglu, *A Quantum Dot Single-Photon Turnstile Device*, Science **290**, 2282 (2000).
Cited in page(s): 93

[98] C. Santori, M. Pelton, G. Solomon, Y. Dale, and Y. Yamamoto, *Triggered Single Photons from a Quantum Dot*, Physical Review Letters **86**, 1502 (2001).
Cited in page(s): 93

[99] A. Kuhn, M. Hennrich, T. Bondo, and G. Rempe, *Controlled generation of single photons from a strongly coupled atom-cavity system*, Applied Physics B: Lasers and Optics **69**, 373 (1999).
Cited in page(s): 93

[100] J. McKeever, A. Boca, A. D. Boozer, R. Miller, J. R. Buck, A. Kuzmich, and H. J. Kimble, *Deterministic generation of single photons from one atom trapped in a cavity*, Science **303**, 1992 (2004).
Cited in page(s): 93, 99, 100

[101] M. Keller, B. Lange, K. Hayasaka, W. Lange, and H. Walther, *Continuous generation of single photons with controlled waveform in an ion-trap cavity system*, Nature **431**, 1075 (2004).
Cited in page(s): 93, 99, 100

[102] M. Hijlkema, B. Weber, H. P. Specht, S. C. Webster, A. Kuhn, and G. Rempe, *A single-photon server with just one atom*, Nature Physics **3**, 253 (2007).
Cited in page(s): 93, 94, 99, 100

[103] B. B. Blinov, D. L. Moehring, L. M. Duan, and C. Monroe, *Observation of entanglement between a single trapped atom and a single photon*, Nature **428**, 153 (2004).
Cited in page(s): 94

[104] S. J. Van Enk, J. I. Cirac, P. Zoller, H. J. Kimble, and H. Mabuchi, *Quantum state transfer in a quantum network: A quantum-optical implementation*, Journal of Modern Optics **44**, 1727 (1997).
Cited in page(s): 94

[105] L. Mandel, *Quantum effects in one-photon and two-photon interference*, Reviews of Modern Physics **71**, S274 (1999).
Cited in page(s): 100

[106] K. Bergmann, H. Theuer, and B. W. Shore, *Coherent population transfer among quantum states of atoms and molecules*, Reviews of Modern Physics **70**, 1003 (1998).
Cited in page(s): 100

[107] M. Hennrich, A. Kuhn, and G. Rempe, *Transition from Antibunching to Bunching in Cavity QED*, Physical Review Letters **94**, 053604 (2005).
Cited in page(s): 103

[108] H.-J. Briegel, G. M. Meyer, and B.-G. Englert, *Dynamic noise reduction in multilevel lasers: Nonlinear theory and the pump-operator approach*, Physical Review A **53**, 1143 (1996).
Cited in page(s): 107, 110

[109] H.-J. Briegel, G. M. Meyer, and B.-G. Englert, *Pump operator for lasers with multi-level excitation*, Europhysics Letters (EPL) **33**, 515 (1996).
Cited in page(s): 107

[110] P. Bushev, D. Rotter, A. Wilson, F. Dubin, C. Becher, J. Eschner, R. Blatt, V. Steixner, P. Rabl, and P. Zoller, *Feedback Cooling of a Single Trapped Ion*, Physical Review Letters **96**, 043003 (2006).
Cited in page(s): 107

[111] D. Rotter, M. Mukherjee, F. Dubin, and R. Blatt, *Monitoring a single ion's motion by second-order photon correlations*, New Journal of Physics **10**, 043011 (2008).
Cited in page(s): 107

[112] K. An, J. J. Childs, R. R. Dasari, and M. S. Feld, *Microlaser: A laser with One Atom in an Optical Resonator*, Physical Review Letters **73**, 3375 (1994).
Cited in page(s): 110

[113] T. Pellizzari and H. Ritsch, *Photon Statistics of the Three-level One-atom Laser*, Journal of Modern Optics **41**, 609 (1994).
Cited in page(s): 110

[114] T. Pellizzari and H. Ritsch, *Preparation of stationary Fock states in a one-atom Raman laser*, Physical Review Letters **72**, 3973 (1994).
Cited in page(s): 110

[115] M. Löffler, G. M. Meyer, and H. Walther, *Spectral properties of the one-atom laser*, Physical Review A **55**, 3923 (1997).
Cited in page(s): 110

[116] C. Ginzel, H.-J. Briegel, U. Martini, B.-G. Englert, and A. Schenzle, *Quantum optical master equations: The one-atom laser*, Physical Review A **48**, 732 (1993).
Cited in page(s): 110

[117] D. Meschede, H. Walther, and G. Müller, *One-Atom Maser*, Physical Review Letters **54**, 551 (1985).
Cited in page(s): 110

E porque, como vistes, têm passados
Na viagem tão ásperos perigos,
Tantos climas e céus experimentados,
Tanto furor de ventos inimigos,
Que sejam, determino, agasalhados
Nesta costa africana, como amigos.
E tendo guarnecida a lassa frota,
Tornarão a seguir sua longa rota.

Luís de Camões, *Os Lusíadas*, Canto I (1572)

It has been a pleasure for me to work on such an interesting topic and to be surrounded with so many remarkable people, both by their scientific merits and their humane qualities.

I owe all that to Rainer Blatt, who welcomed me in his research group and always had a fierce belief in me and in this project.

It's impossible to wish for better bosses than Christoph Becher and Piet O. Schmidt. They trusted me, always had an open door for me, were always supportive and made a lot of helpful suggestions, making it a real pleasure to discuss every little detail of the experiment.

For all that I have learned from the other assistants in the group, namely Jürgen Eschner, Ferdinand Schmidt-Kaler, Christian Roos, Wolfgang Hänsel, Hartmut Häffner, Timo Körber and Markus Hennrich, a big thank you.

The experimental work presented here would not be possible at all if it weren't for all the people who patiently answered all my questions and cleared my doubts. Regarding the design of the experiment, Andreas Mundt, Axel Kreuter, Stephan Gulde and Matthias Schulz, were helpful giants with broad comfortable shoulders. On the theory side, I would like to thank Helmut Ritsch and Thomas Salzburger for every single discussion we had. Their insight on the theory behind our single-ion device was crucial.

I was lucky to benefit from the talent and craft of Anton Schönherr and Stefan Haselwandter. They were able to transform a long succession of ugly and ill-defined sketches into the most beautiful apparatus I have ever seen. Vielen Dank! I have not forgotten the elegant pieces after the other, Helmut Jordan and Josef Dummer turned, a special thank you for you too!

Getting the experimental setup to work was a herculean task and I was lucky to share this load with fantastic people. I am thankful to:

Harald Schöbel and Lukas An der Lan, for investing a month of their summer vacation in building the coolest and best looking black box that contains our Hanbury-Brown and Twiss setup.

Christian Maurer, for his work in the simulation of the single-photon source, which defined a guideline that was helpful through all this work.

Eoin Phillips, for his good advice, for fighting my stubbornness and for the help

in the really hard times, specially those in which random noise in the CCD picture already started to look like teddy bears.

Thomas Monz, for his pragmatism, hard work and funny jokes that could put a smile in our faces when thinks went really wrong.

Helena Barros and Andreas Stute, for they have been the best friends and partners in this adventure. Their strength and undeniable optimism were inspiring and counteracted my "reserved realism". They also have the merit of being fantastic interpreters of my confuse and crippled speech. I hope the setup rewards them with great results.

François Dubin, for joining us in the fight with all his insight and energy, and for believing in the victory when all we could see was a doomed battle, merci beaucoup!

To the other members of the group and to my other friends, thank you for supporting me in the bad times, for celebrating with me in the good times, but most of all, thank you for filling the ordinary days of my life with rich experiences and emotions.

Aos meus pais e família, gostaria de agradecer o amor, carinho e apoio incondicional que sempre me deram. Mas de todos, és tu, Leonor, meu amor, a quem eu devo mais.